

NAT'L INST. OF STAND & TECH



A11106 406018

NIST  
PUBLICATIONS

U.S. DEPARTMENT OF COMMERCE  
National Institute of Standards and Technology

*NIST Special Publication 766*

*NBS/BAM 1986 Symposium on  
Advanced Ceramics*

*S. M. Eise and H. Czeles, Editors*







*NIST Special Publication 766*

---

*NBS/BAM 1986 Symposium on  
Advanced Ceramics*

---

Edited by

S. M. Hsu  
Ceramics Division  
Institute for Materials Science  
and Engineering  
National Institute of Standards  
and Technology  
Gaithersburg, MD 20899

and

H. Czichos  
Bundesanstalt für Materialprüfung  
Unter den Eichen 897  
D-100 Berlin 45  
German Federal Republic



NOTE: As of 23 August 1988, the National Bureau of Standards (NBS) became the National Institute of Standards and Technology (NIST) when President Reagan signed into law the Omnibus Trade and Competitiveness Act.

May 1989

U.S. Department of Commerce  
Robert A. Mosbacher, Secretary

National Institute of Standards and Technology  
Raymond G. Kammer, Acting Director

---

Library of Congress  
Catalog Card Number: 89-600737  
National Institute of Standards  
and Technology  
Special Publication 766  
Natl. Inst. Stand. Technol.  
Spec. Publ. 766  
159 pages (May 1989)  
CODEN: NSPUE2

U.S. Government Printing Office  
Washington: 1989

For sale by the Superintendent  
of Documents  
U.S. Government Printing Office  
Washington, DC 20402

## PREFACE

The National Institute of Standards and Technology (NIST) (formerly NBS) and the Bundesanstalt fur Materialprufung (BAM) share many similar missions and responsibilities in materials characterization, standards, and measurement sciences. Consequently, scientific interactions have been conducted on an informal basis between the organizations for many years. In 1984, these activities were increased through the auspices of the Versailles Project on Advanced Materials and Standards (VAMAS).

Discussions with Professor H. Czichos of BAM at the Gordon Research Conference on Tribology in 1984 and the Wear Conference in 1985 indicated that more frequent, structured, exchanges of scientific and technical data between our organizations would be valuable. Specifically, Professor Czichos suggested an annual seminar series similar to the well-recognized Leeds-Lyon Conference on Tribology. Enthusiastic response from NIST and BAM culminated in a 2-day seminar on ceramics at BAM in April 1986. A second joint seminar was held at the NIST in April 1987 and addressed corrosion and wear. A third seminar on polymers was held in September 1988 at BAM.

My participation in both seminars has convinced me of the value of these exchanges and I hope that these meetings which further international collaboration and understanding will continue.

This volume, a result of the first seminar, contains valuable data and scientific information which is of particular use to the ceramics technical community.

STEPHEN M. HSU  
Chief, Ceramics Division  
National Institute of Standards and Technology  
(formerly the National Bureau of Standards)



## ABSTRACT

Advanced ceramics offer many advantages that other materials do not possess. They have high strength, dimensional stability, are chemically inert, lightweight, wear resistant, and have desirable properties in electrical, optical, and thermal applications. At high temperatures, they are the only class of material with reasonable properties. As such, advanced ceramics is increasingly used in electronic, structural, wear, optical, and electrical applications and devices.

Worldwide production of advanced ceramics is growing rapidly. Since ceramics are based on alumina and silica, the most abundant minerals on earth, effective utilization of ceramics carries implications into the next several centuries.

One of the major technical barriers to widespread use of ceramics is the inability of industry to manufacture reliable ceramics reproducibly and economically. Advanced ceramics are sensitive to small defects introduced during processing and generated during use. The identification of key parameters and subsequent measurements of these parameters are crucial to control the quality of ceramics. The National Institute of Standards and Technology (NIST) (formerly National Bureau of Standards, NBS), and the Bundesanstalt fur Materialprufung (BAM) to a large extent, share a similar mission to assist their respective industries to achieve reliable manufacturing through standards. This symposium therefore provides timely exchange of technical information on a very significant subject area.



## CONTENTS

	Page
A Critical Assessment of Requirements for Ceramic Powder Characterization; A. L. Dragoo, C. R. Robbins, and S. M. Hsu, NBS.....	1
Microstructural Modification in Ceramics Resulting from Diffusion Induced Boundary Migration; J. E. Blendell, NBS.....	19
Structural Reliability of Ceramics at Elevated Temperatures; E. R. Fuller and S. W. Wiederhorn, NBS.....	29
An Ultrasonic Study of Ceramics from the Green State to Fully Fired; A. L. Dragoo, NBS.....	42
Nondestructive Characterization of Ceramic Materials: Thermal Waves G. S. White, NIST, E. H. LeGal LaSalle, Laboratoire d'Optique Physique, ESPCI.....	59
Computer-aided Ultrasonic Testing of Non-Oxide Ceramics; A. Hecht, E. Neumann, P. Rose, BAM.....	79
Computertomography; J. Goebbels, H. Heidt, A. Kettschau, and P. Reimers, BAM.....	97
Nondestructive Characterization of Ceramic Materials: Small Angle Neutron Scattering, K. A. Hardman-Rhyne and E. R. Fuller, NBS.....	101
Introduction to the Versailles Project on Advanced Materials and Standards (VAMAS) Technical Working Area: Wear Test Methods; S. Becker and J. Lexow, BAM.....	111
Fretting of Ceramic Materials, D. Klaffke, BAM.....	126
Tribology of Advanced Ceramics, S. M. Hsu, NBS.....	144



A CRITICAL ASSESSMENT OF REQUIREMENTS FOR CERAMIC POWDER  
CHARACTERIZATION

A. L. Dragoo, C. R. Robbins and S. M. Hsu  
National Bureau of Standards  
Gaithersburg, Maryland

Abstract

The detailed characterization of ceramic powders is very important for the reproducible manufacture of advanced ceramics that will perform reliably in service. The basic issues are: what to measure, how to measure it and how to assure quality in analytical measurements by all laboratories. "What to measure" involves understanding the relationship between powder characteristics and ceramic microstructures. "How to measure it" requires the development of measurement methods and the determination of repeatability and reproducibility. Standard Reference Materials (SRM) are required to assure the quality of measurements and the comparability of measurements between different laboratories and techniques. From considerations of the distributed nature of powder and ceramic properties, new SRM's are proposed which will certify distributed properties. As an example of such SRM's, technical requirements are developed for the production of an SRM with a certified particle size distribution for ceramic powders. Factors which enter the certification of a particle size distribution for a ceramic powder include the approximate mathematical representation of the distribution, weighting of the distribution by the measurement technique, the particle shape distribution, and statistical variances introduced by the powder, the sampling methods, and the method of measurement.

## I. Introduction

In their study conducted for the National Bureau of Standards, Charles River Associates Inc. (CRA)<sup>1</sup> identified three key barriers to the commercialization of ceramic materials for advanced technological applications: production cost, reliability in service, and reproducibility in manufacture. For the case of ceramic components for heat engines CRA saw reliability as a major technological barrier and improved characterization of ceramic powders as providing "important leverage in overcoming the reliability and reproducibility problems."<sup>2</sup> Improved characterization of ceramic powders requires not only improved measurements but also improved understanding of how powder characteristics are related to properties and performance of resulting ceramic materials.

Ceramic powders and ceramic microstructures share a common feature that is important for the improved characterization of both powders and microstructures: i.e., due to local variations on the scale of grain size, characteristics are distributed rather than single-valued in nature. The distributed nature of characteristics requires that a measured characteristic must be represented, at least, by two statistics: by a mean and a standard deviation for the material variation. These two statistics often may not be sufficient; for example, if the distribution is multimodal or higher skewed.

The importance of the distributed nature of ceramic characteristics is met, for example, in the fact that the strength of a material under brittle fracture is determined by a limiting flaw which may be a crack, void, pore cluster, or large grain. Limiting flaws are the larger outliers within the population of flaws. Flaws result from a variety of factors including

variability in the starting powder. For example, hard agglomerates in ceramic powders have been noted as the cause of gross voids in a variety of ceramics sintered from active powders.<sup>3-8</sup>

What are the characteristics of powders which most influence the microstructure of a resulting ceramic? And, how can the relevant properties be measured best? Table 1 lists many of the physical and chemical characteristics of powders. It is evident from a survey of the physical characteristics, in particular, (1) that some properties are related, such as specific surface area, porosity and particle size; and (2) that characterization of a feature, such as agglomerates, involves several characteristics. Further, a qualitative characteristic such as the "hardness" of an agglomerate requires description in terms of both chemical and physical characteristics which are measurable. Thus, a single characteristic does not appear to be generally sufficient to predict the sinterability of a powder.

Techniques, such as sedimentation and electrical zone sensing, which employ a macroscopic amount of material for measurement of particle size and porosity provide a measure of the distributed aspect of those characteristics. As an example of the considerations required in the development of a standard for a distributed characteristic of a powder, requirements for particle size SRM will be considered below in Sections III to VI. The ability to measure a distributed characteristic on a macroscopic quantity of powder is not the case for many other characteristics, especially for chemical characteristics. Information regarding the distribution of a chemical characteristic is most often obtained by microscopic techniques, such as analytical microscopy.

Improvement in the measurement of physical and chemical characteristics of powders requires development of improved measurement techniques and sample preparation procedures that have increased precision and accuracy. Precision is "the agreement within a set of observations or test results obtained as are directed in a method."<sup>9</sup> Each observation or test must be carried out in a manner to assure the independence of each result. "Repeatability" is defined here as that aspect of precision involving comparison of results within a single laboratory and with a single technique. "Reproducibility" is defined here as that aspect of precision involving comparison between laboratories or between different techniques. Accuracy is "the degree of agreement between the true value of the quantity ... and the average of many observations."<sup>9</sup> The terms "bias" and "systematic error" are used here to refer to the deviation between the true and observed values. Standards are required to measure the bias between techniques and in the case of absolute measurements, to establish the amount of bias within a technique.

Standard Reference Materials (SRM) are characterized and certified by the National Bureau of Standards for some chemical or physical properties. The issues of precision and accuracy are addressed in the characterization of these materials. Kaye<sup>10</sup> has drawn attention to the need for the National Bureau of Standards to play a greater role in providing standards for particle size and shape for the fineparticle industry. With the expectation that ceramic powders will provide some of the future fineparticle standards, the NBS Ceramics Division is engaged in a

long-range program of developing and certifying Standard Reference Materials (SRM's) intended to improve the assurance of chemical and physical quality of ceramic powders.

## II. Existent Particle Size Standards

A variety of reference materials are presently available for the calibration of particle size measurements. Table 2 summarizes the particle size standards which are available from governmental organizations. Table 3 lists a variety of particle size references which are available commercially. Spherical polymer particles with very narrow size ranges have been certified for single particle size values. SRM 1690 consists of polystyrene spheres which were manufactured on board a space shuttle to achieve improved roundness. Mulholland et al.<sup>11</sup> described the certification of SRM 1690, a nominal one micrometer diameter standard. Although latex and polystyrene spheres have excellent dimensional and shape characteristics, limited quantities and costs may restrict their use to applications such as primary calibrants in a laboratory and as reference materials where only small quantities are required. In addition, these materials are transparent to x-rays and cannot be used to calibrate instruments which use x-ray attenuation. Finally, these materials provide a single-point calibration.

The reference materials based on glass beads and quartz powder or sand have certified size distributions obtained by sieving, sedimentation and electrical sensing zone techniques. Although glass beads can be obtained with nearly spherical shapes, it is difficult to prepare glass materials that are bubble free. The development and certification of quartz powder

and sand as Certified Reference Materials (CRM's) for distribution by the Community Bureau of Reference of the European Economic Community were described by Wilson<sup>12</sup>.

The introduction of new synthesis methods for ceramic precursor powders, such as reactions in flames and plasmas, and the use of alkoxides and other organometallic precursors in aqueous and nonaqueous liquid systems, has begun to provide a variety of submicrometer sized particles which often have very regular shapes. The growing availability of these powders poses challenges to physical characterization methods used to measure them and to the standards used to assure the quality of these powders. However, these new powders offer the opportunity of new source materials for improved standards for physical, as well as chemical, characteristics of powders. Here, we briefly examine some of the requirements for such a ceramic powder if it is to provide the basis for a Standard Reference Material for particle size measurements. A standard for submicrometer sizes and with a size distribution approximating an idealized distribution, such as the well-known lognormal distribution, is of special interest because it will enable comparisons of different methods of size measurement to be compared with a greater degree of confidence.

### III. Empirical and Idealized Particle Size Distributions

Estimates of a mean size  $\bar{x}$ , and a standard deviation,  $\sigma$ , always can be obtained directly from the experimental data. However, if a particle size distribution can be represented satisfactorily by an ideal or model distribution, then estimates of other statistics can be obtained. For example, it is possible to calculate distribution means<sup>13</sup>,

$$\bar{x}_{1,j} = \frac{\int_{x \min}^{x \max} x q_j(x) dx}{\int_{x \min}^{x \max} q_j(x) dx} \quad (1)$$

and arithmetic means

$$\begin{aligned} \bar{x}_{k,0} &= \frac{\int_{x \min}^{x \max} x^k q_0(x) dx}{\int_{x \min}^{x \max} q_0(x) dx} \quad 1/k \quad (2) \\ &= k \sqrt{M_{k,0}} \end{aligned}$$

where the index refers to the basis of the distribution: i.e.,

- j = 0 for a number distribution
- j = 1 for a length distribution
- j = 2 for an area distribution
- j = 3 for a volume distribution.

$M_{1,j}$  is the first order moment with respect to an  $j$ th type distribution;  $M_{k,0}$  is a  $k$ th order moment with respect to a number distribution. Since different measurement techniques impose different distributions on a population of particles, a functional representation of a particle size distribution enables results of various techniques to be compared.

The lognormal distribution which was introduced over a century ago by Galton<sup>14</sup> and McAlister<sup>15</sup> has been found to model observed particle size distributions found both in nature and from industrial processes<sup>16-18</sup>. In addition to the lognormal distribution there are several other distributions which may be considered. The Rosin-Rammler distribution<sup>19,20</sup> was found to describe the properties of powdered coal. The Pearson Type V distribution<sup>21</sup> has been used as the assumed functional form for particle size measured by a commercial photon correlation spectrometer<sup>22</sup>.

For the lognormal distribution the percentage,  $d\phi$ , of particles between  $z$  and  $z + dz$ , where  $z = \ln x$ , is expressed as

$$d\phi = q(z)dz = \frac{1}{\sigma_z \sqrt{2\pi}} \exp \left[ -\frac{(z-\bar{z})^2}{2\sigma_z^2} \right] dz. \quad (3)$$

The statistics  $\bar{z}$  and  $\sigma_z$  of the distribution can be expressed in terms of the geometric mean,  $x_g$ , and the geometric standard deviation:

$$\bar{z} = \ln x_g \quad (4a)$$

$$\sigma_z = \ln \sigma_g \quad (4b)$$

The geometric mean is equal to the mode and median values if the number frequency distribution is plotted with respect to the logarithm of the particle size. The lognormal distribution has the property that the standard deviation is independent of the choice of basis. Simple logarithmic relationships exist between the geometric means for the higher order distributions and  $x_g$  and  $\sigma_g$ . Also, various arithmetic means and moments of lognormal distributions with respect to different bases can be related to these statistics<sup>23</sup>.

Procedures for fitting an empirical distribution to a lognormal distribution and for testing the distribution were given by Kottler<sup>24-27</sup>. He examined the calculation and use of the log-probit plot. Although such a plot appears linear if the data exhibits lognormal behavior, the data cannot be fitted by a simple linear regression procedure. From the cumulative probability

$$p = \int_{-\infty}^t q(t)dt \quad (4)$$

where  $t$  is the normal deviate,  $t = (x - \bar{x})/\sigma$ , and, where  $q(t)$  is given by

eq (3), a change,  $\delta P$ , is related to  $\delta t$  by

$$\delta P = q(t) \delta t \quad (5)$$

It is  $t$  which is proportional to  $\ln x$ . To estimate the goodness of fit by a calculation of Chi-squared for the errors in the normal deviate, it is necessary to use the Mueller-Urban weights

$$W = N[q(t)^2/P(1-P)] \quad (6)$$

where  $N$  is the number of particles in the population. The standard error bands about the  $P' = P(\text{computed})$  versus  $\log x$  line are given by  $P' \pm S'$ , where

$$S' = [P'(1-P')/N]^{1/2} \quad (7)$$

Minimization of the value of Chi-squared is complicated by the fact that the errors in  $P$  are cumulative, and therefore, not independent. Kottler described a method of successive approximations by which Chi-squared can be minimized.

#### IV. Particle Shape

Ceramic powders, with a few exceptions, do not consist of spherical or nearly spherical particles. Kaye<sup>10</sup> has defined an ideal reference material as "usually composed of dense, smooth, spherical fine particles, the characteristics of which can be measured directly with different characterization procedures that employ different physical measurement technology." However, the condition of sphericity may be relaxed

- (1) if the particle shape is regular so that a physical dimension can be related to a measured equivalent diameter;
- (2) if a numerical shape characteristic is narrowly distributed for a given particle size;
- (3) if the shape characteristic does not vary significantly over the range of particle sizes of interest.

The relaxation of the sphericity condition requires the determination of one or more particle shape factors. Development of shape factors will require the use of microscopy and image analysis to obtain related measurements of particle size and shape. King<sup>28,29</sup> discussed the use of image analysis and the development of particle size statistics from image data.

#### V. Methods for Particle Size Measurements

The concept of particle size, although intuitively meaningful, is operationally ambiguous since the measured value depends significantly on the method of measurement because the measurement imposes a particular selectivity on the particle size distribution. Variance in the measurement is sometimes superimposed on the inherent variance of the powder. Biases may be introduced by the experimental procedure and by the approximations which relate the instrumental response to the particle size. At the present time, a definitive method does not exist for measuring a particle size distribution. A definitive method is "based on sound theoretical principles and which has been experimentally demonstrated to have negligible systematic errors and a high level of precision"<sup>30</sup>. To achieve high accuracy in a definitive method, especially for measurement of a physical property, the measurement must be referenced to the standards for the fundamental units. Determination of a particle size distribution and associated shape factors will require a suite of methods which may include microscopy and image analysis, sedimentation with ultracentrifugation and electrical sensing zone measurements.

Wood<sup>31</sup> has discussed various methods of particle size analysis from the standpoint of the dynamic range of the method and the basis, or weighting, factor,  $j$ , of the measured distribution, see Eq. (1) and (2). Fig. 1 summarizes a variety of size analysis methods with respect to dynamic range and weighting factor. Wood distinguishes between a primary weighting factor which describes the manner in which classes of particles are counted and a secondary weighting factor which is a function of equivalent diameter basis and the measurement principle. An analytical technique which determines the equivalent diameter (ED) from projected area has a secondary weighting factor  $j = 2$ ; a technique which determines ED from a volume measurement has  $j = 3$ ; and a technique which determines ED from a surface-to-volume ratio has  $j = 2.5$ .

It is important that the method used to measure the distribution must not yield a large standard error,  $S$ , see Eq. (8), over the range of certification. As Kottler<sup>26</sup> noted,  $S$  is proportional to  $N^{-1/2}$  where  $N$  is the total number of particles measured. For a technique which measures the relative concentration on a mass basis, such as sedimentation,  $N$  is replaced effectively by the mass of particles in the volume over which the measurement is carried out. This consideration implies that image analysis methods may require the analysis of on the order of 10,000 images to obtain a satisfactorily limit of uncertainty.

## VI. Certification, Packaging and Stability of SRM's

The development and certification of an SRM requires the performance of the following tasks:

- identification of the measurement need;
- determination of the characteristic to be certified;
- identification of potential source materials;

- small, actual differences between measurement methods which become discernible with improved precision;
- underestimate of the standard deviation for a method.

## VII. Conclusion

As ceramic components find a wider application in the national and international economies, the need for standards for quality assurance in their manufacture and use will increase. Since the quality of the starting powder is an essential factor in attaining reliability and reproducibility of ceramic components, it follows that new Standard Reference Materials will be needed for the measurement of particle size. Since the particle size of ceramic powders is generally a distributed property, SRM's with certified particle size distributions are expected to be necessary for the development and use of improved ceramic materials.

Since SRM's are developed to meet the measurement needs of industry and commerce, it is important that new SRM's for particle size measurements reflect user needs with respect to material, size range and possible auxiliary properties. Consequently, the suggestions of and collaboration with the user community are welcome.

## Acknowledgements

The partial support of this work by the Office of Automotive Technology Development, Department of Energy, is gratefully acknowledge.

## References

1. J. R. H. Black, S. L. Blum, S. H. Kalos, and G. C. Tasse, "An Economic and Technical Assessment of Advanced Ceramic Materials," Am. Ceram. Soc. Bull., **64** [1] 39-41, 50 (1985).
2. Charles River Associates Inc., Technological and Economic Assessment of Advanced Ceramic Materials, Vol. 1; Planning Report 19. NBS GCR 84-470-1. National Bureau of Standards, August 1984.
3. C. A. Bruch, "Sintering Kinetics for the High Density Alumina Process," Am. Ceram. Soc. Bull., **41** [12] 799-806 (1962).

4. J. S. Reed, T. Carbone, C. Scott, and S. Lukasiewicz, "Some Effects of Aggregates and Agglomerates in the Fabrication of Fine Grained Ceramics," p. 171 in *Processing of Crystalline Ceramics*. Edited by H. H. Palmour, R. F. Davies, and T. M. Hare. Plenum Press, NY, 1978.
5. W. H. Rhodes, "Agglomerate and Particle Size Effects on Sintering Yttria-Stabilized Zirconia," J. Am. Ceram. Soc., 64 [1] 19-22 (1981).
6. A. L. Dragoo and L. P. Domingues, "Preparation of High-Density Ceria-Yttria Ceramics," J. Am. Ceram. Soc., 65 [5] 253-59 (1982).
7. F. F. Lange and M. Metcalf, "Processing-Related Fracture Origins: II, Agglomerate Motion and Cracklike Internal Surfaces Caused by Differential Sintering," J. Am. Ceram. Soc., 66 [6] 398-406 (1983).
8. F. W. Dynys and J. W. Halloran, "Influence of Aggregates on Sintering," J. Am. Ceram. Soc., 67 [9] 596-601 (1984).
9. Standard Terminology for Statistically Related Terms, ASTM Standard D4392-84
10. B. H. Kaye, "Standard Fineparticles - Who Needs Them?" Chemtech, 40-43, Jan. 1980.
11. G. W. Mulholland, A. W. Hartman, G. G. Hembree, E. Marx and T. R. Lettieri, "Development of a One-Micrometer Diameter Particle Size Standard Reference Material," J. Res. Natl. Bur. Stand. (U.S.), 90 [1], 3 - 26 (1985).
12. R. Wilson, "Reference Materials of Defined Particle Size Certified Recently by the Community Bureau of Reference of the European Community," Powder Tech., 27, 37-43 (1980).
13. DIN 66141, "Darstellung von Korn-(Teilchen)groessen-verteilungen," February 1974.
14. F. Galton, "The Geometric Mean, in Vital and Social Statistics," Proc. Roy. Soc. London, 29, 365-67 (1879).
15. D. McAlister, "The Law of the Geometric Mean," Proc. Roy. Soc. London, 29, 367-76 (1879).
16. J. Aitchison and J. A. C. Brown, *The Lognormal Distribution with Special Reference to Its Use in Economics*. Cambridge University Press, Cambridge, 1957.
17. K. Mahmood, "Lognormal Size Distribution of Particulate Matter," J. Sedimentary Petrol., 43 [4] 1161-66 (1973).
18. S. K. Kurtz and F. M. A. Carpay, "Microstructure and Normal Grain Growth in Metals and Ceramics. Part 1. Theory," J. Appl. Phys., 51 [11] 5725-44 (1980).

19. P. Rosin and E. Rammler, "The Laws Governing the Fineness of Powdered Coal," J. Inst. Fuel, 7, 29-34 (1927).
20. P. Rosin and E. Rammler, "Grinding Properties of Coal," Zement, 20 210-13, 240-41, 317-21, 343-46, 363-65 (1931).
21. J. K. Ord, "Pearson System of Distributions," pp. 655-59 in Encyclopedia of Statistical Sciences, Vol. 6. Wiley, New York, 1985.
22. L. G. Bunville, "Commercial Instrumentation for Particle Size Analysis," pp. 1-42 in Modern Methods of Particle Size Analysis. Edited by H. G. Barth. Wiley, New York, 1984.
23. T. Allen, Particle Size Measurement, 3rd ed.; pp. 157-61. Chapman and Hall, London, 1981.
24. F. Kottler, "The Distribution of Particle Sizes, Part I," J. Franklin Inst., 250, 339-56 (1950).
25. F. Kottler, "The Distribution of Particles Sizes, Part II," J. Franklin Inst., 250, 419-41 (1950).
26. F. Kottler, "The Goodness of Fit and the Distribution of Particle Sizes, Part I," J. Franklin Inst., 251, 499-514 (1951).
27. F. Kottler, "The Goodness of Fit and the Distribution of Particle Sizes, Part II," J. Franklin Inst., 251, 617-41, (1951).
28. R. P. King, "Determination of the Distribution Size of Irregularly Shaped Particles from Measurements on Sections or Projected Area," Powder Technol., 32, 87-100 (1982).
29. R. P. King, "Measurement of Particle Size Distribution by Image Analyzer," Powder Technol., 39, 279-89 (1984).
30. J. K. Taylor, Handbook for SRM Users. NBS Special Publication 260-100. National Bureau of Standards, Sept. 1985.
31. B. C. Wood, "Selection Criteria for Particle Size Analysis Equipment," Powder Bulk Solids, 35-39 (April 1986).
32. T. Allen and A. A. Kahn, "Critical Evaluation of Powder Sampling Procedures," Chem. Engr., CE108-CE112 (May 1970).
33. T. A. Hatton, "Representative Sampling of Particles with a Spinning Riffler. A Stochastic Model," Powder Technol., 19, 227-33 (1978).
34. R. C. Oppenheim and J. A. Hersey, "Physical and Chemical Changes in Powders on Storage," J. Powder Bulk Solids Technol., 1 (3), 3-9 (1977).

Table 1. Characteristics of Ceramic Starting Powders

Physical Characteristics	Chemical Characteristics
Grains (Primary Particles)	Bulk Composition
Size	Major Elements
Shape	(1 to 100%)
Agglomerates (Secondary Particles)	Minor Elements
Size	(10 ppm to 1%)
Shape	Trace Elements
Porosity	( < 10 ppm)
Amount (See Density)	Inorganic Species
Size	(for example,
Shape	sulfates and
Particle Contact	nitrates)
Coordination	Organic Species
Strength	Water and other
	volatiles
	Phases
Density	
Specific Surface Area	Surface Composition
Permeability	Major Elements
Compactibility	Minor Elements
Flowability	Trace Elements
	Inorganic Species
	Organic Species
	Water
	Phases

Table 2. Particle size standards certified by governmental organizations.  
Particle size is in units of  $\mu\text{m}$ .

Material	Source	Use	Property
SRM 484b, Magnification Scale	NBS	SEM(s)	1,2,3,5,50
SRM 474, Line Width		OM(s)	1 to 12
SRM 1688, Latex Spheres		In preparation or planning	
SRM 1689, Latex Spheres		In preparation or planning	
SRM 1690, Polystyry. Spheres		Diam	$\sim 0.9$
SRM 1691, Polystyry. Spheres			$\sim 0.3$
SRM 1692, Polystyry. Spheres		In preparation or planning	
SRM 1960, Polystyry. Spheres			$\sim 10.0$
SRM 1003, Glass Beads		Stokes Diam	3 to 5
SRM 1004, Glass Beads		Sieves	34 to 120
SRM 1017a, Glass Beads		Sieves	100 to 310
SRM 1018a, Glass Beads		Sieves	225 to 780
CRM 066, Quartz Powder	BCR	Stokes Diam	0.35 to 3.50
CRM 067, Quartz Powder		Stokes Diam	2.4 to 32.0
CRM 068, Quartz Sand		Vol Diam	160 to 630
CRM 069, Quartz Sand		Stokes Diam	14 to 90
CRM 070, Quartz Powder		Stokes Diam	1.2 to 20
CRM 130, Quartz Sand		Vol Diam	50 to 220
CRM 131, Quartz Sand		Vol Diam	480 to 1800
CRM 132, Quartz Sand		Vol Diam	1400 to 5000
CRM 165, Latex Spheres	BCR	Particle Counting, Light scattering	$2.223 \pm 0.013$
CRM 166, Latex Spheres			$4.821 \pm 0.019$
CRM 167, Latex Spheres			$9.475 \pm 0.018$

Table 3. Examples of commercially available particles for size references.

Polymer Spheres

Polystryrene (PS)  
Polyvinyl-Toluene (PVT)  
Polyvinyl-Divinyl Benzene (DVB)  
Polystryrene-Butadiene (PSB)

Spherical Pollens

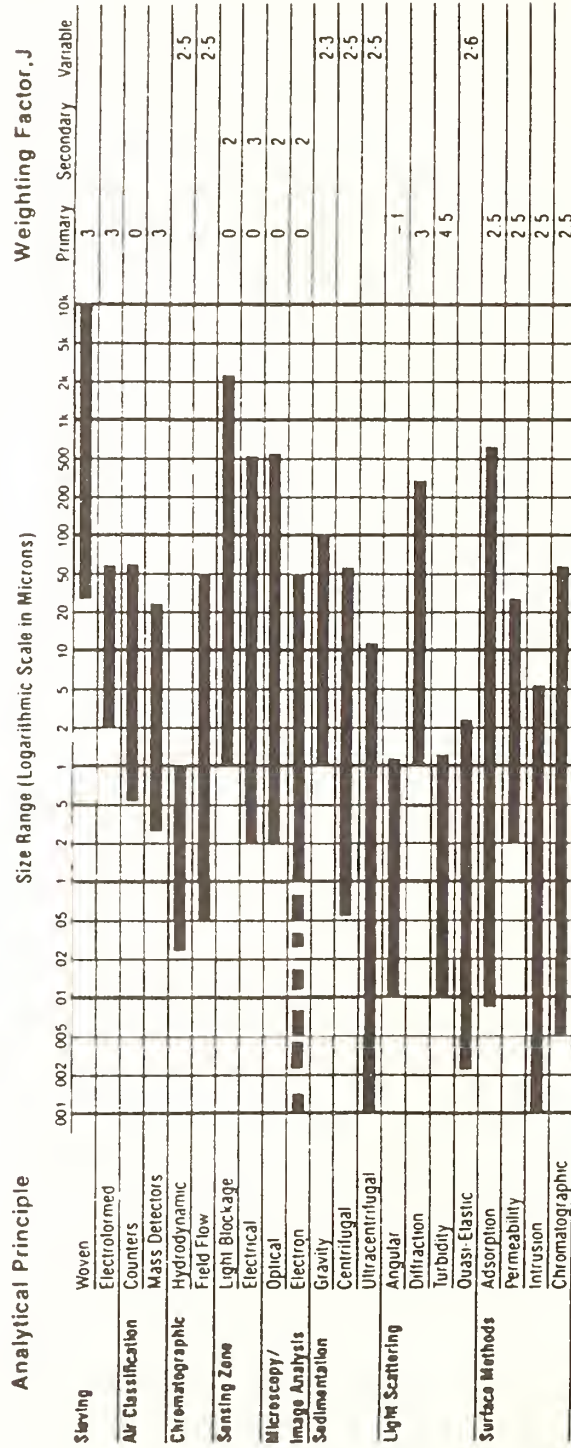
Paper Mulberry  
Ragweed  
Bermuda Grass  
Walnut  
Corn

Uniform Glass Microspheres

Test Dusts

AC Fine  
Arizona Road

## Analytical Principle vs. Size Range and Weighting Factor, J



Courtesy Powder/Bulk Solids, Minneapolis, MN.

MICROSTRUCTURAL MODIFICATIONS IN CERAMICS RESULTING  
FROM DIFFUSION INDUCED BOUNDARY MIGRATION

J. E. Blendell  
Ceramics Division  
Institute for Materials Science and Engineering  
National Bureau of Standards  
Gaithersburg, MD 20899

INTRODUCTION

The recent observations of Diffusion Induced Grain Boundary Migration (DIGM) in ceramics have caused a reevaluation of the stability of interfaces under conditions where diffusion is occurring. We will review what DIGM is, show typical microstructures that occur, explain why this phenomenon is important to ceramics processing and give some examples of how DIGM affects the properties of ceramic materials.

DIGM is the migration of grain boundaries due to the diffusion of a solute in the boundary.<sup>1</sup> The boundaries are otherwise stable; that is, they will not migrate at these temperatures without the introduction of the solute. In DIGM experiments this stabilization is usually accomplished by annealing the samples at high temperatures to cause grain growth. When the solute is introduced into the system at a lower temperature, the boundaries migrate. The area swept out by the moving boundaries has been alloyed. The alloying has occurred to a much larger extent than can be accounted for by lattice diffusion at the experimental temperatures. DIGM has also been observed during dealloying, in which the solute diffuses out of the sample. For a critical review of DIGM see Handwerker.<sup>2</sup>

There is an analogous process, Liquid Film Migration (LFM), that occurs in solid-liquid systems under similar conditions to DIGM except that a liquid film separates the grains, rather than a grain boundary. The microstructures observed in LFM are nearly identical to those observed in DIGM. The differences are due to the shape of the grains in a solid-liquid system. For example, in the MgO system, with a liquid present the grains tend to be spherical, and when no liquid is present the grains tend to be polyhedral.

A typical microstructure produced by DIGM is shown schematically in Figure 1, along with many of the other features commonly observed in DIGM. The original position of the boundary is shown as a dotted line, the final

positions are solid lines and the cross-hatched regions have been alloyed with the solute. The differences between DIGM and grain growth are striking. During DIGM boundaries move away from their centers of curvature as they migrate, whereas in grain growth the boundaries move towards their centers of curvature. The area of the boundaries increases during DIGM in contrast to grain growth where the grain boundary area decreases. Also DIGM occurs at temperatures much lower than those at which grain growth occurs. During grain growth, the boundaries tend to remain smoothly curved, or locally planar if faceting occurs. Boundaries that are migrating during DIGM often show sinusoidal shapes with the same boundary migrating into both adjacent grains. As shown in Figure 2, a range of boundary shapes are observed in the same sample although there is usually a tendency for one boundary shape to dominate.

One important problem about DIGM has been the identification of the driving force. There exist many driving forces for boundary migration, such as curvature, phase transitions, temperature gradients and electric field gradients. When these have been eliminated by experimental design, DIGM is still observed during solute diffusion. While there is a reduction in the free energy of the system by the formation of the alloy, this energy reduction is not sufficient to drive boundary migration.<sup>3</sup> For example, in isotope self diffusion, the same free energy of mixing is dissipated, but there is no coupling of the energy of mixing to a force driving the motion of the boundary. This is because the isotope atoms are chemically identical and the boundary has no interaction with the isotope. Thus the boundary does not "know" that isotope self diffusion is occurring. Another way to think about it is that for a boundary to move there must be a force on it. The motion of the boundary can be prevented by applying an opposite force. If the free energy decrease during isotope mixing could drive the motion of the boundary, then there exists a force that could prevent the boundary motion and therefore, isotope mixing. As there is no force that can be applied to prevent, or reverse isotope mixing, the free energy decrease due to isotope mixing can not apply a force on the boundary. The non-ideal terms in the free energy might, in theory, apply a force on the boundary, but the occurrence of DIGM both for positive and negative deviations from ideal solution behavior, and both for alloying and

dealloying, with identical microstructures and velocities, demonstrate that these excess thermodynamic terms do not provide the driving force.<sup>2</sup>

It is now well established that the driving force for DIGM is the coherency stress due to the difference in lattice parameter between the constrained alloyed region and the unalloyed bulk.<sup>4</sup> All other proposed mechanisms have been eliminated either by thermodynamic arguments or by experiment. Most importantly, the critical experiment of demonstrating that the migration velocity goes to zero as the difference in lattice parameter between the diffusion zone and the unalloyed bulk goes to zero, has been performed.<sup>4</sup>

#### COHERENCY STRESS MODEL

DIGM arises when there is diffusion of a solute down a grain boundary and into the lattice adjacent to the grain boundary. When the solute is of a different atomic size than the solvent, this diffusion causes the lattice to be locally stressed. When there is a difference in stress between the grains, atoms will migrate from the higher stressed side, across the boundary to the lower stressed side. The boundary will thus migrate into the region of higher stress. The velocity of a boundary is determined by the difference in stress across the boundary and the rate of diffusion of atoms across the boundary.

The stress necessary for DIGM will exist even when lattice diffusion is effectively "frozen out", that is, at low temperatures. A atomic jump of only one lattice spacing into the lattice from the grain boundary is needed to create the coherency stress. Even at low temperatures there is always some mixing of solute atoms from the grain boundary into the lattice, although it may be very limited in depth.

The stress difference across the boundary can arise for several reasons. Because of the anisotropy of the elastic modulus, even for cubic materials, there will be a difference in stress for different crystallographic orientations. The strain is determined by the change in lattice parameter with composition and is isotropic for cubic materials. Alternatively, if the dislocation content of one grain is higher, or one grain is oriented so that the stress can cause dislocation generation, then stress relief can occur in that grain. Thus there will always be a difference in stress across a grain boundary which will initiate migration.

For the case of two solid grains separated by a liquid (LFM), the compositional change due to the stress can be determined from the free energy,  $f$ , as a function of composition using a common tangent construction.<sup>5</sup> This is shown in Figure 3.  $c_{\text{coherent}}$  is the composition of the stressed material and  $c_{\text{eq}}$  is the equilibrium composition. At the stressed grain, material of composition  $c_{\text{coherent}}$  will dissolve in the liquid, migrate across the liquid film (down the composition gradient) and precipitate on the unstressed grain at composition  $c_{\text{eq}}$ .

#### MICROSTRUCTURAL EFFECTS

DIGM has been observed<sup>6</sup> in the MgO system with additions of NiO or CoO as shown in Figure 4. Boundaries are induced to migrate, increase their curvature and cause alloying at much higher rates than when diffusion is not occurring.

LFM has also been observed<sup>7</sup> in the same system, using  $V_2O_5$  as the liquid phase. Typical microstructures are shown in Figure 5. The composition profiles have been determined<sup>8</sup> for the liquid case and are shown in Figure 6. The conditions of temperature and time used in these experiments were calculated using the coherency stress model.

The microstructures observed are very different from typical structures seen in ceramics. The interlocking nature of the grain boundaries is a feature of boundaries that have moved due to DIGM. This feature can lead to enhanced creep resistance by increasing the diffusion distance. Another unique result of DIGM is a reduction in the grain size. Since all the grain boundaries migrate into the adjacent grains, a first order model predicts that there will be a reduction in the grain size by approximately a factor of 14 (the number of neighbors). Thus it may be possible to reduce the grain size of a ceramic by solute diffusion after sintering. This would provide advantages in increased strength and in addition, could significantly change the electrical properties. In metallic systems DIGM has been observed to switch from occurring in the bulk, to a surface phenomenon as the temperature is increased.<sup>9</sup> This can be used to modify the surface of a material to produce a surface coating without changing the bulk microstructure or properties.

However there are situations where DIGM would not be advantageous. For fiber reinforced composites, DIGM can lead to increased bonding between

the fiber and the matrix. This will reduce the effectiveness of fiber pull-out as a toughening mechanism. For ceramics used as nuclear waste storage materials, boundary migration due to the presence of compositional inhomogeneities can occur. Radioactive material could be leached out at significantly higher rates than predicted. Since DIGM can occur at very low temperatures and long times, DIGM will not be observed in leach tests performed in the laboratory.

#### SUMMARY

DIGM is the motion of grain boundaries due to the diffusion of a solute down the grain boundary and into the lattice. The areas swept out by the boundary are alloyed while areas not swept remain unalloyed. DIGM occurs at temperatures much lower than those where grain growth occurs.

The driving force for DIGM is the coherency stress due to the difference in atomic size between the solute atoms and the solvent material. The coherency stress model has been very accurate in predicting the temperature and times necessary for observing DIGM and LFM. Other proposed mechanisms have been eliminated either by thermodynamic arguments or by experiment.

The changes in the microstructure due to DIGM can have a major effect on the properties of materials. Interlocking boundaries may increase the high temperature creep resistance of ceramics, change the toughness for grain boundary fracture, but will degrade the properties if a specific microstructure is required as in many composites. Also, the ability of ceramics to be effective nuclear waste storage materials may be reduced by the dealloying that can occur. Thus DIGM is an important process for determining the long term performance of ceramic materials.

## REFERENCES

1. M. Hillert and G.R. Purdy, *Acta Met*, 26, 333(1978).
2. C.A. Handwerker, Diffusion in Thin Films, ed. D. Gupta, Noyes Publications, (1987).
3. R.W. Balluffi and J.W. Cahn, *Acta Met*, 29, 493(1981).
4. W. Rhee and D.N. Yoon, *Acta Met*, 35, 57(1987).
5. C.A. Handwerker, J.W. Cahn, J.E. Blendell and D.N. Yoon, Diffusion in Solids: Recent Developments, ed. M.A. Dayananda and G.E. Murch, Metallurgical Soc., Warrendale, PA (1985).
6. J.E. Blendell, C.A. Handwerker, C.A. Shen and N.D. Dang, Ceramic Microstructures '86, ed. J. Pask and A.G. Evans, Plenum Press, New York(1987).
7. C.A. Handwerker and J.E. Blendell, to be published.
8. C.A. Handwerker, R. Marinenko, D.E. Newbury and J.E. Blendell, to be published.
9. J.E. Blendell, C.A. Handwerker, W.A. Kaysser and G. Petzow, Surfaces and Interfaces in Ceramic and Ceramic-Metal Systems, ed. J. Pask and A.G. Evans, Plenum Press, New York(1981).

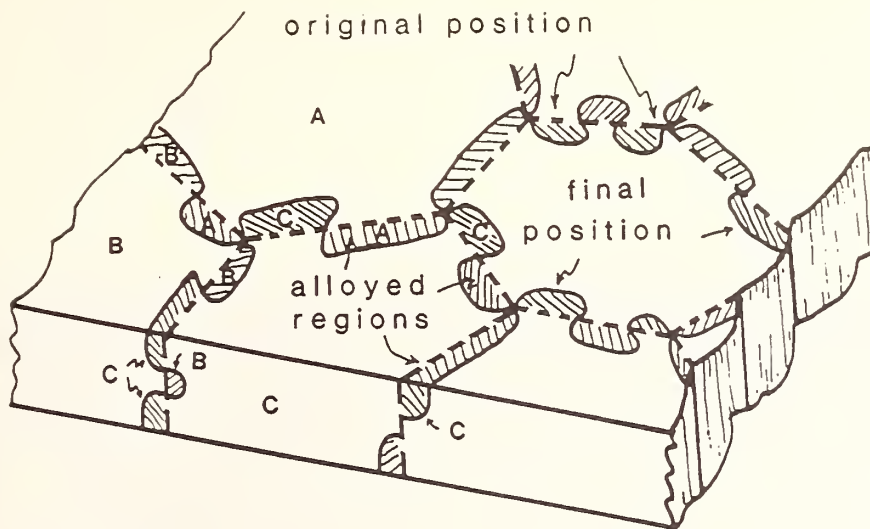


Figure 1. Schematic of microstructures observed in DIGM. Boundaries that were initially straight have migrated away from their centers of curvature and alloying has occurred only in the regions swept by the boundaries. The regions behind the migrated interface have epitaxial relationships with the matrix grains as indicated by the letters.

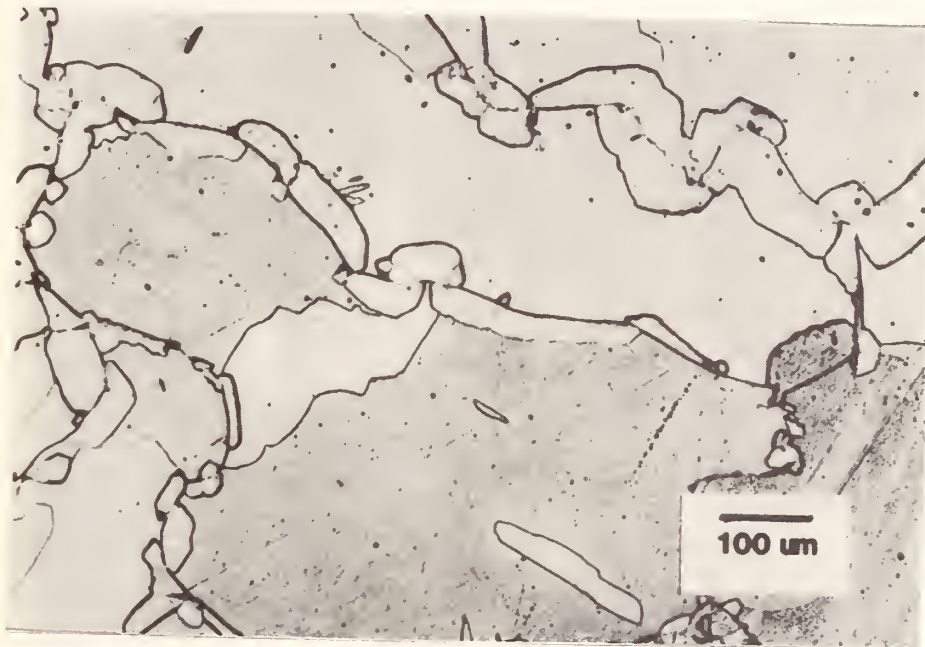


Figure 2. Microstructure observed in Iron foils that have been exposed to Zinc vapor. DIGM has occurred with a variety of boundary morphologies.

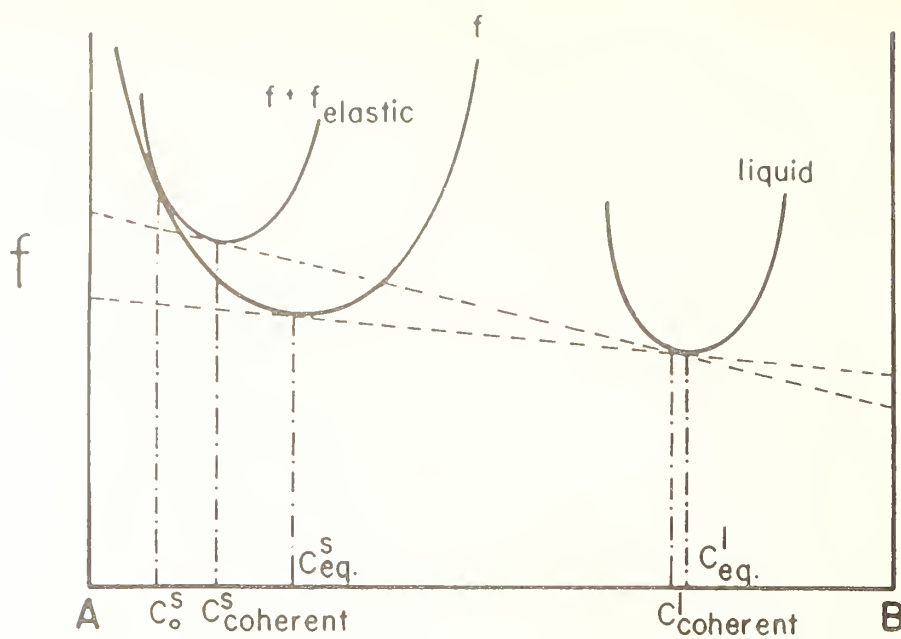


Figure 3. Free energy,  $f$ , as a function of composition in a binary system, A-B. Shown is the common tangent construction for determining the composition of an unstressed planar solid,  $c_{eq}^s$ , in contact with its equilibrium liquid and for a coherently stressed solid,  $c_{coherent}^s$ , in contact with its equilibrium liquid.

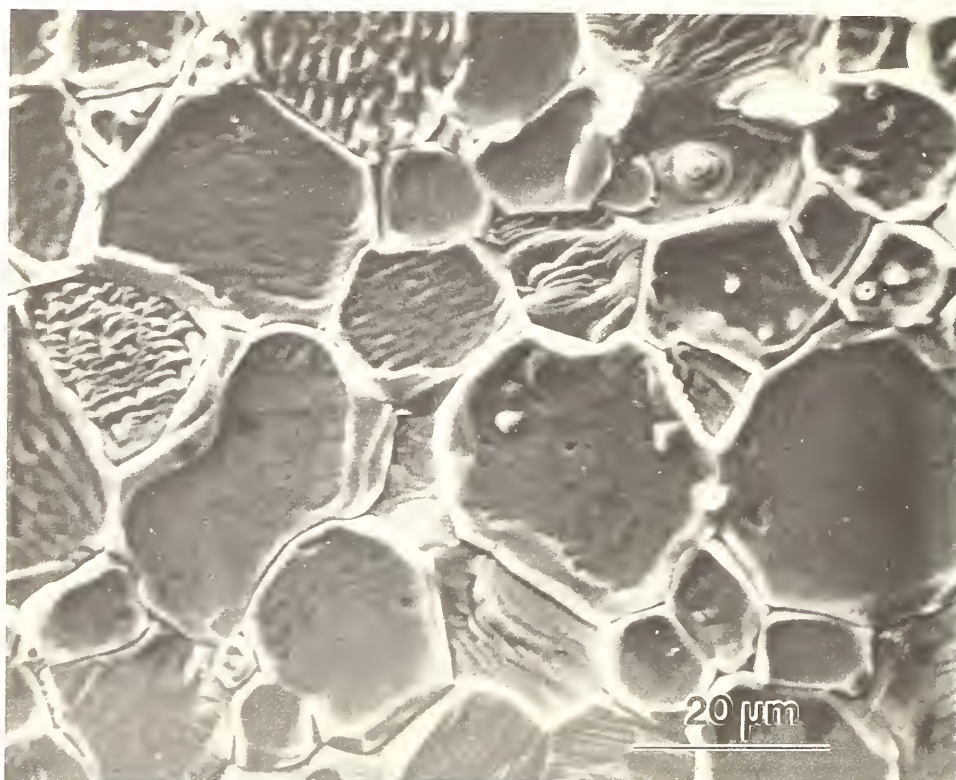


Figure 4. DIGM in MgO-NiO system. Surface of MgO sample exposed to NiO at 1280°C for 16 hrs. The surface relief due to solute addition in the regions swept by the grain boundaries can be clearly seen. Facetting is seen on several grain surfaces.

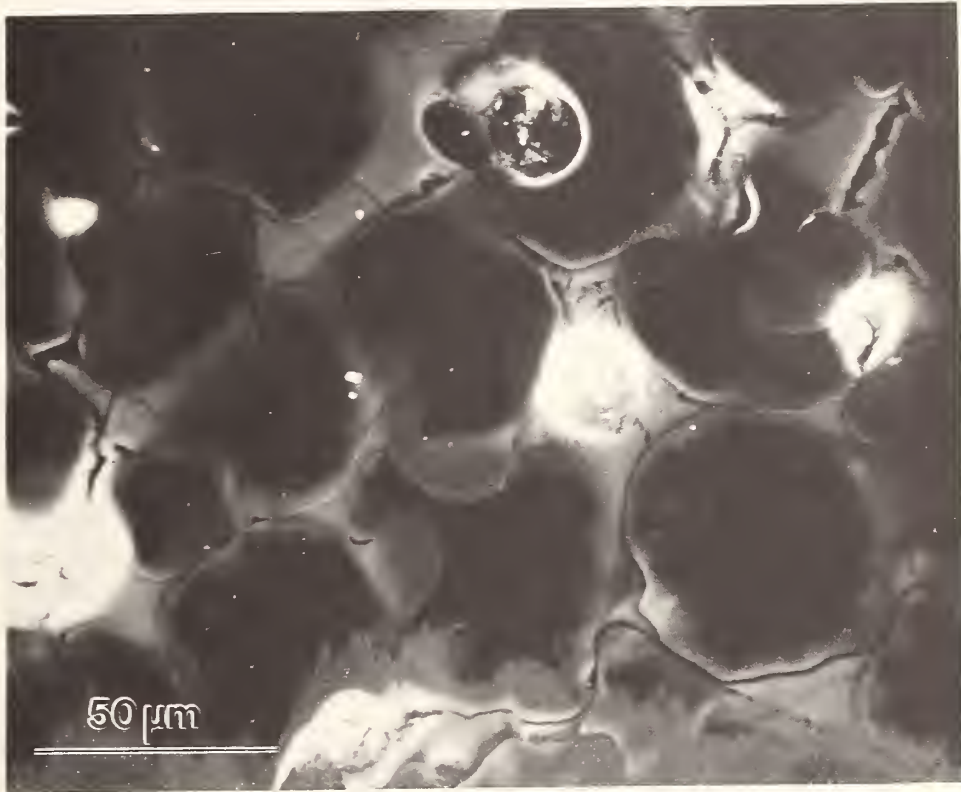


Figure 5. Liquid Film Migration in  $\text{MgO-V}_2\text{O}_5$  as a result of Co diffusion at  $1250^\circ\text{C}$  for 20 min. Boundaries have migrated away from their centers of curvature and alloying, as indicated by the lighter gray, has occurred. The grains were initially spherical.



Figure 6. Quantitative Electron Microprobe analysis showing Co concentration in the grains due to alloying. The original grains are pure MgO as indicated by the darkest gray. The regions of intermediate gray indicate alloying with Co.

STRUCTURAL RELIABILITY OF CERAMICS  
AT ELEVATED TEMPERATURES

E. R. Fuller, Jr. and S.M. Wiederhorn

Ceramics Division  
Institute for Materials Science and Engineering  
National Bureau of Standards  
Gaithersburg, MD 20899

ABSTRACT

Current methodologies for assessing the structural reliability of ceramic materials at elevated temperatures are reviewed. Typically these methods have been based on fracture mechanics concepts, such as those used to describe low-temperature, brittle fracture, in which failure is assumed to ensue from the subcritical growth of a pre-existing flaw to a critical size. However, recent high-temperature data for ceramics suggest that this view may be over simplified, and that flaw or damage accumulation may be an important aspect of high-temperature reliability. The need for incorporating these concepts into a high-temperature reliability methodology is discussed.

INTRODUCTION

If strength were the sole criterion for structural performance, high-temperature structural ceramics, not metallic alloys, would be the materials of choice for a number of high-temperature structural applications [1], e.g., gas turbine engines. This observation was based on the fact that the strength of the better high-temperature structural ceramics is greater than that of the alloys currently being used in turbine engines. Accordingly, in figure 1, the strength of a grade of yttria-doped, hot-pressed silicon nitride is compared with that of Waspaloy, and several other alloys used for high-temperature applications [2,3]. The figure indicates that this silicon nitride has a potential 400°C use-advantage over Waspaloy, as indicated by the temperatures for which the strength of both materials falls precipitously. If a way could be found to utilize this high-temperature strength of ceramics, then the economy of a myriad of high-temperature structural applications would be improved considerably.

But to be used in heat-temperature applications, ceramics not only have to be strong, but they also have to be tough. Reliability of design also requires that the variance of strength be low to avoid failure as a consequence of subcritical crack growth, or momentary overloads in service. Demands such as these are difficult for ceramic materials to meet, since they traditionally lack the low variance in strength, the high fracture toughness, and the thermal shock resistance of metals. Nevertheless, high-temperature resistance to chemical attack, and a high mean strength at elevated temperatures suggest a considerable potential for these materials in heat engines. This potential for high-temperature structural

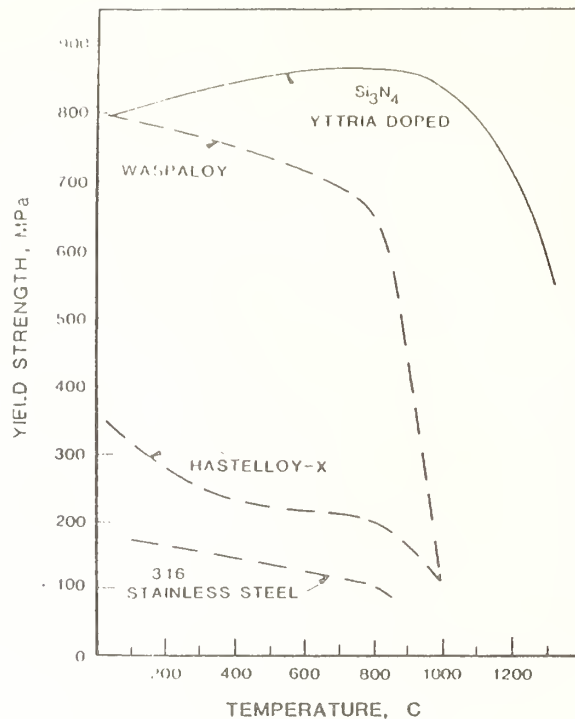


Figure 1. Comparison of the fracture strength of a yttria-doped silicon nitride [3] with the yield strength of three commercial alloys [2].

applications has been the incentive during the past fifteen years for most of the work to improve the mechanical behavior of structural ceramics.

At room temperature, ceramics are brittle materials. Their strength is determined by microstructural flaws, such as voids, inclusions and cracks, which may be present in the material. At high temperature, ceramics exhibit some ductility. However, since the number of degrees of freedom for plastic flow is generally not sufficient for arbitrary shape changes, ceramics still behave in a semi-brittle manner. In addition, time-dependent plastic flow, such as occurs during creep, results in the generation of cracks and cavities that eventually lead to stress rupture of ceramics. These two characteristics of ceramics, flaw sensitivity at low temperature and flaw generation at high temperature, largely determine the mechanical behavior and structural reliability of these materials.

In this paper we review the techniques that have been developed to improve the reliability of structural ceramics, and we relate these techniques to the mechanical and chemical behavior of the materials at elevated temperature. Four important high-temperature phenomena related to structural reliability are noted: 1) The enhanced chemical reactivity of materials at elevated temperatures, which can lead to structural modifications and flaw generation; 2) the existence of a threshold stress or stress intensity factor for creep crack growth; 3) a predominantly strain-controlled creep-rupture regime for stresses below this crack growth threshold, where reliability is governed by distributed damage processes; and 4) the redistribution of applied stresses as a result of creep and damage processes.

## STRUCTURAL CHANGES AND FLAW GENERATION

At elevated temperatures a number of new processes can occur that influence structural reliability. For example, kinetic processes, such as chemical reactions, diffusion, and viscous flow, occur more rapidly, and thermodynamic processes can result in phase transformations and new phase equilibria. Even in the absence of an applied stress, strength degradation can occur as a consequence of specific chemical reactions between the ceramic and the environment, or because of physical transformations that occur as a consequence of phase instability. For example, the reaction of inclusions in magnesia-doped, hot-pressed silicon nitride with the oxygen in the air can result in the formation of surface corrosion pits that replaced machining damage as the source of failure [4-6]. Other examples include: second-phase precipitation along grain boundaries, as in yttria-doped silicon nitride [7], devitrification of a grain-boundary glass, as in vitreous bonded alumina [8], and chemical modification of the grains themselves, as in zirconia toughened ceramics [9-10]. Specific chemical or thermodynamic reactions are usually not considered in reliability methodologies, and techniques for predicting failure as a consequence of these processes have not been developed. Because of this, materials exhibiting these degradation mechanisms must be either improved by ceramic processing, or else not used under conditions where the degradation can occur.

When stresses are present, the high-temperature strength of a material may be degraded either by the growth of cracks from flaws, as at room temperature, albeit usually by different processes, or by the generation, growth and linkage of creep cavities or cracks. At the same time such strength degradation processes are occurring, other processes may occur that reduce the severity of flaws and thereby improve the strength. The resulting strength will thus depend on the relative kinetics of the competitive processes. This competition is manifested by a threshold for crack growth, above which creep crack growth is the predominant failure mechanism and below which stress-enhanced flaw generation is the important mechanism. These concepts are elaborated further in the following sections.

### CRACK GROWTH THRESHOLD

Although the growth of cracks and flaws can be an important factor in the lifetime of structural materials at elevated temperatures, the influence of creep processes, sintering and chemical reactions on the fracture process cannot be ignored. These processes can cause effective "blunting" or "healing" of flaws or cracks, whereby giving rise to a crack growth threshold, i.e., a threshold stress intensity factor,  $K_{th}$ , below which cracks do not propagate. However, when the applied stress intensity factor,  $K_I$ , exceeds this threshold,  $K_I > K_{th}$ , crack propagation results in the same type of delayed failure as is observed at low temperatures, although crack propagation in this instance may be accompanied by a crack-tip creep deformation zone. Below this threshold, propagating cracks arrest as a consequence of creep or other high-temperature processes that reduce the flaw severity. This threshold becomes an important high-temperature design parameter, because the material's response is drastically different above and below the threshold. Above the threshold,

design by crack growth models of failure [11-15] is appropriate; below the threshold, damage generation models are appropriate [16-18].

The existence of a high-temperature threshold for crack growth has been suggested by a number of authors [5,16-23], based on both strength and crack propagation data. The most convincing evidence for such thresholds comes from strength studies on specimens containing small indentation cracks. Such specimens are subjected to a static stress until failure occurs and the time-to-failure is recorded. If failure does not occur in a specified time, the specimens are intentionally broken in a controlled manner to measure their strength. "Blunting" or "healing" of the indentation crack results either in failure from some site other than the indentation, or in a substantial increase in the strength. Techniques such as these have been used by Tressler and co-workers [21-22] to determine the crack growth threshold in silicon carbide, and by Quinn [20] to map out the crack growth regime for magnesia-doped, hot-pressed silicon nitride.

Recent data by Grathwohl [16] and by Dalgleish et al. [18] clearly indicate a boundary between those failure mechanisms controlled by crack growth, and those mechanisms controlled by flaw generation. Grathwohl's data, for example, show that different creep rupture responses are obtained for smooth and indented specimens, see figure 2. Specimens that failed from the indentation cracks follow a continuous stress-rupture curve, typical of a crack-growth dominated stress-rupture behavior. The stress-

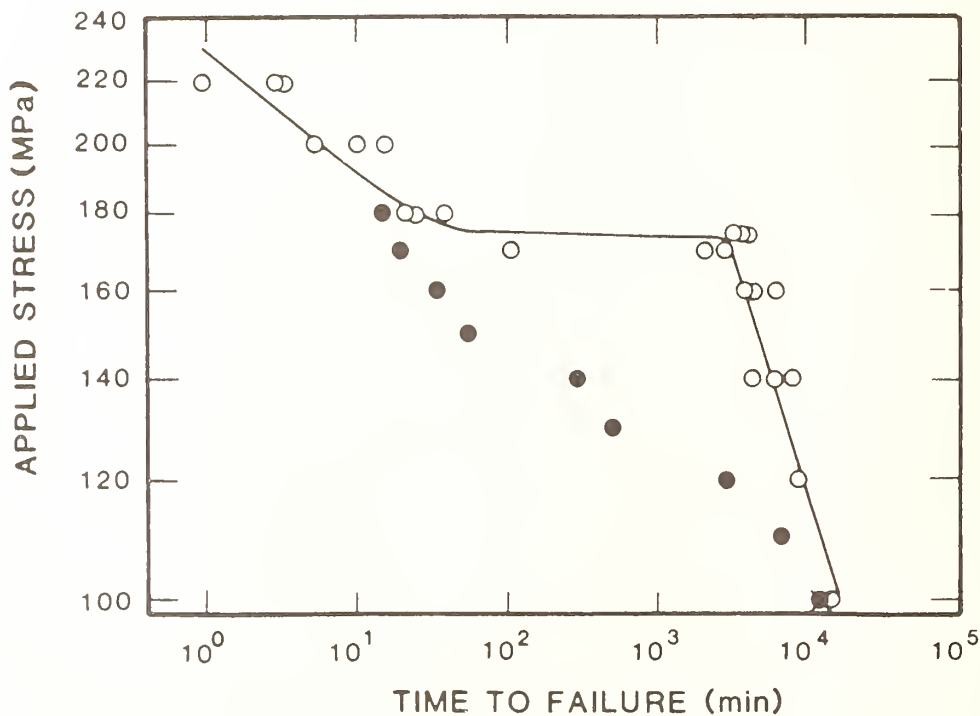


Figure 2. High-temperature creep rupture data for a hot-pressed silicon nitride (Annawerk GmbH) at 1200°C. At a given applied stress, the time-to-failure is plotted both for as-machined specimens (open circles) and for precracked specimens (filled circles). The precracked specimen at 100 MPa did not fail from the precrack. From Ref. [11].

rupture curve for the smooth bar specimens, however, shows a distinct break at a critical value of the applied stress. The high stress portion of the curve is identical to that of the indented specimens and therefore, is believed to be the result of crack growth. The break in the curve represents a possible "blunting" threshold, indicative of a transition from crack-growth dominated failure processes to creep rupture and/or flaw nucleation processes, although Grathwohl interprets this break as a consequence of the stress relaxation in the flexural specimen from creep.

### CREEP RUPTURE

At elevated temperatures, creep is the process that limits lifetime of most ceramics. Because ceramics are inherently brittle, even at elevated temperatures, lifetime is not usually limited by component extension, that occurs as a consequence of creep, but rather by the formation of cavities and cracks, that are generated by the creep process. High-temperature processes (sintering, plastic deformation, chemical reaction) that anneal cracks and reduce their severity also generate new flaw populations that are now the sources of failure. This dual role of high-temperature processes in determining failure is illustrated in figure 3 for a crack in siliconized silicon carbide which has been loaded at 1300°C [24]. Although the crack has been blunted by creep deformation and its growth arrested, continued deformation in the vicinity of the original crack tip results in the formation of cavities along shear bands. The linkage of these cavities accounts for the eventual failure of this material. Blumenthal and Evans [25] have observed a similar behavior for a commercial grade of hot-pressed aluminum oxide at elevated temperature.

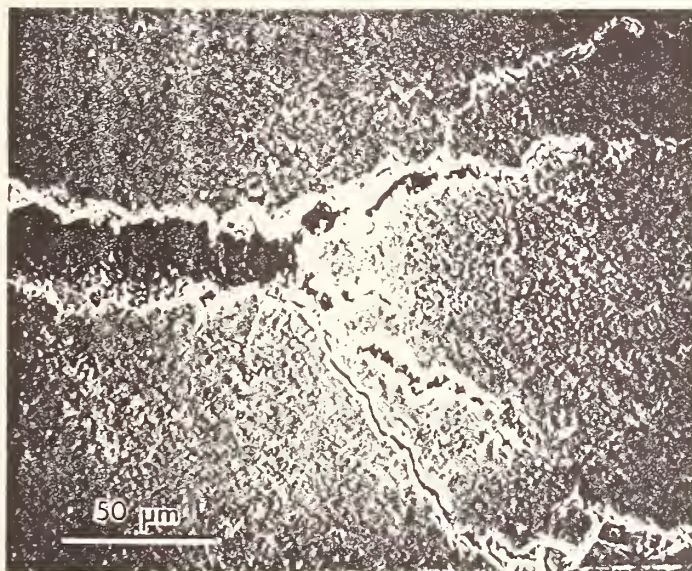


Figure 3. Blunted crack in siliconized silicon carbide at 1300°C. Continued deformation causes the crack to generate damage along shear bands emanating from the blunted crack tip [24].

Creep-rupture at elevated temperatures usually involves both damage generation, such as the nucleation and growth of cavities, and the linkage of these cavities to form cracks that cause failure. Depending on the specific damage mechanism, any of these processes may be the rate limiting step for failure. In an attempt to understand high-temperature failure mechanisms of ceramics and their dependence on microstructure, a considerable amount of theoretical work has been conducted to model the failure process [26-33]. Failure mechanisms are usually classified according to material type: those having a two-phase structure, and those having no second phase at the grain boundary. Usually these mechanisms assume that the time-to-failure depends only on one of the critical processes given above. The results are expressed in terms of a parametric relationship between failure time, temperature, applied stress and strain rate, as was done by Monkman and Grant [34] for metals. Ideally the constants in these parametric relationships can be expressed in terms of physical properties, so that, in principal, the failure time can be related both to basic material properties, such as viscosity and diffusivity, and to microstructural characteristics, such as grain size and volume fraction of second phase. To date, however, quantitative comparisons between theory and experiment have not proven satisfactory, suggesting the need for additional work to understand the fundamentals of creep rupture in ceramics.

Accordingly, current understanding of creep-rupture in ceramic materials at elevated temperatures is largely empirical. The small body of data that is available suggests that the failure of structural ceramics follows parametric relationships, such as the Monkman-Grant relationship [34], in which the time-to-failure,  $t_f$ , has an inverse relation to the minimum strain rate,  $\dot{\epsilon}$ , so that,  $t_f \dot{\epsilon} = \text{constant}$ . This relationship between strain rate and time-to-failure was first demonstrated for ceramics by Kossowsky et al. [35] for a grade of magnesia-doped, hot-pressed silicon nitride, figure 4. Since two distinct curves are obtained for the data in helium and the data in air, this study also indicates an influence of environment on the creep-rupture time. More recently, Grathwohl [16] confirmed these findings with flexural tests for another grade of silicon nitride. Grathwohl also measured the strain during creep and found that the strain-to-failure was constant for his material, as would be expected from the Monkman-Grant relation. This finding supports the idea of a strain-limited rupture criterion. Recent studies by Johnson et al. [36] and by Wiederhorn et al. [8] suggest that the Monkman-Grant coefficient,  $t_f \dot{\epsilon}$ , for some ceramic materials is not a constant, but rather depends on the applied stress and/or the temperature.

The development of a data base for lifetime prediction at elevated temperatures requires the evaluation of Monkman-Grant coefficients for material-environment systems of interest. As these coefficients must dependent on both the material's microstructure and the environment, and since no unifying concepts have emerged from creep-rupture data to date, it seems unlikely that a universal coefficient will be found for this equation. However, once the Monkman-Grant coefficient, and its stress and temperature dependence are known (or for that manner, the parameters for some other parametric relationship), the relationship can be used for the prediction of failure time. These equations replace those derived for the crack-growth dominated lifetime predictions at low temperatures.

Strain-limited failure criterion, such as the Monkman-Grant relationship, implies that lifetime at elevated temperatures is determined,

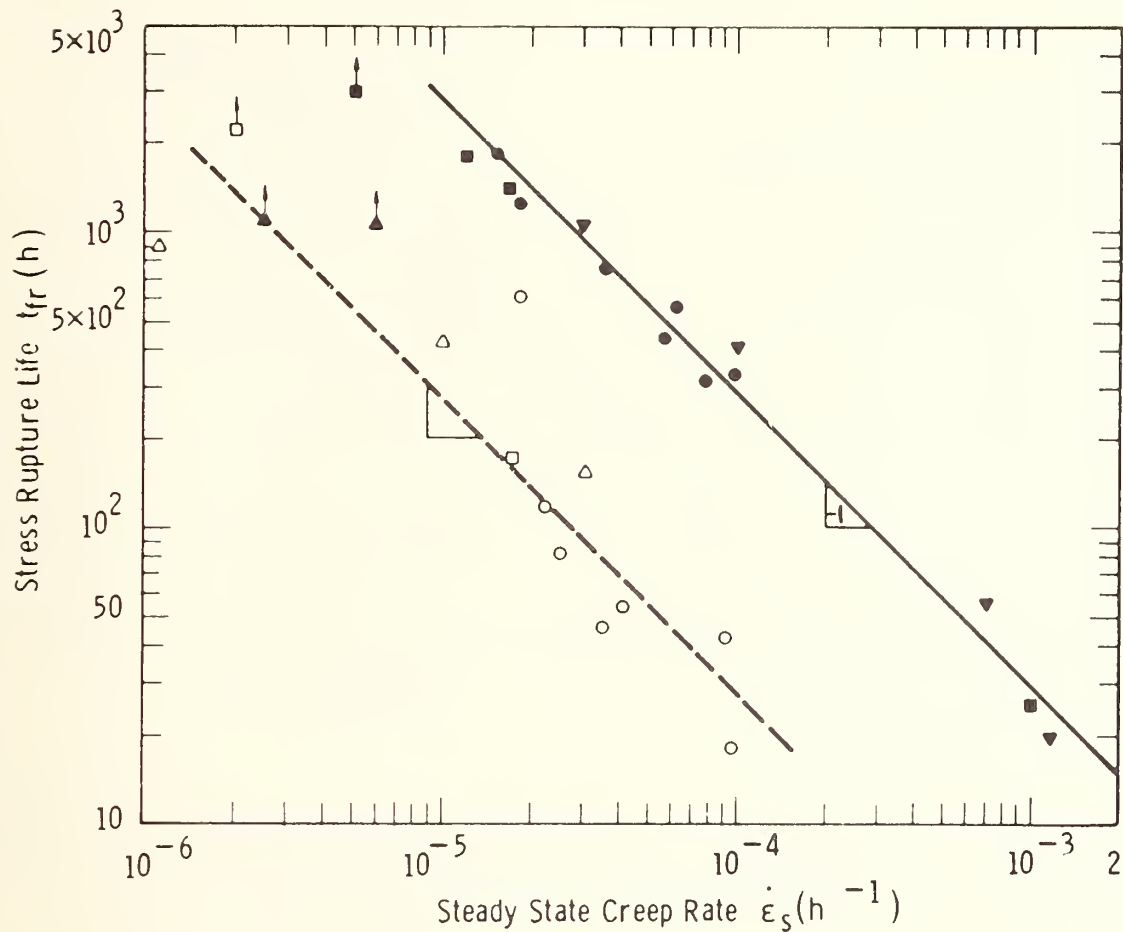


Figure 4. Dependence of creep-rupture life on the steady state creep rate in tension for a hot-pressed silicon nitride (HS-130). The solid and open symbols are for specimens tested in air and in helium, respectively. From Ref. [35].

not by the rate of crack growth, but by the rate of creep. Accordingly, improvements in lifetime can be achieved through the use of processing techniques to reduce the creep rate. Since the dependence of creep rate on microstructural variables is well understood, the use of creep theory to improve lifetime at high temperature is a feasible procedure.

#### CREEP REDISTRIBUTION OF STRESS

Thus far, the stress state has been assumed to be invariant in time. However, when a component is subjected to stress gradients, such as in a flexural test specimen, this assumption is only valid if the creep rate is linearly proportional to the stress. If the creep rate is not linearly proportional to stress, then the stress distribution will change in time, and depending on the processes controlling creep, steady state creep may not be established. Several steady state solutions for this stress redistribution have been obtained for power law creep of flexural beams, examples of which are shown in figure 5. This figure illustrates three

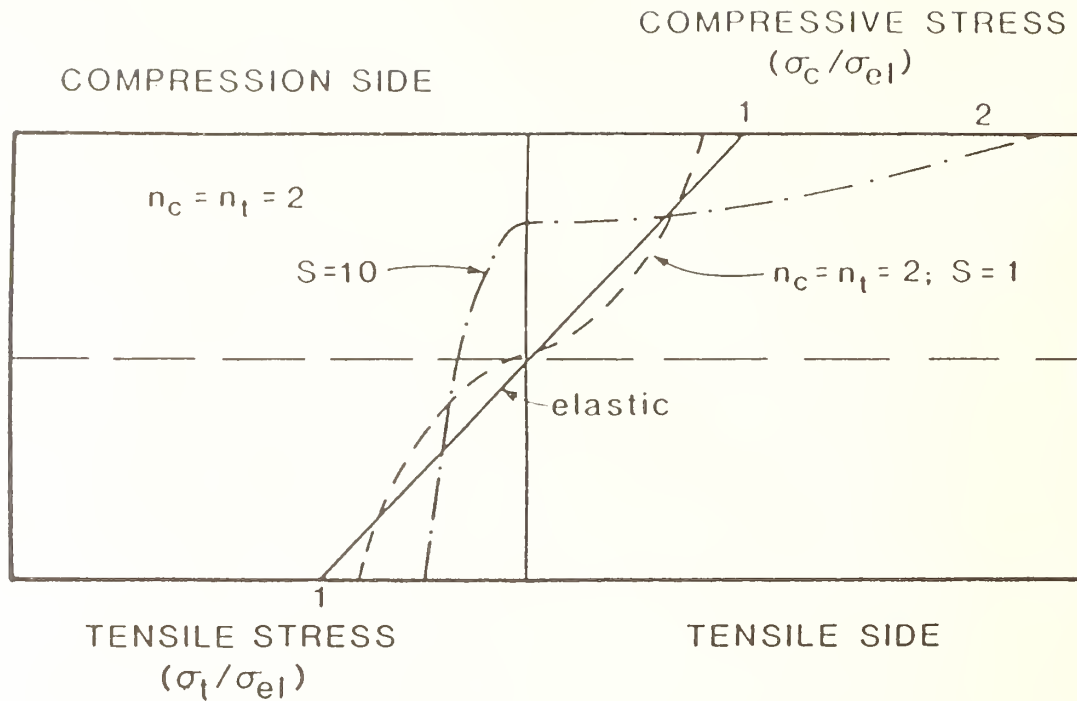


Figure 5. Calculated steady-state stress distributions for a flexural beam in creep. The creep rate in compression and tension are given, respectively, by the equations:  $\dot{\epsilon}_c = A \sigma^{n_c}$  and  $\dot{\epsilon}_t = A (S\sigma)^{n_t}$ .

separate cases for the steady state creep stress distribution. The "elastic" solution is obtained for a linear relation between strain rate and stress. The sigmoidal-shaped curve is obtained for power law creep with equal rates of creep in tension and in compression. However, when the creep rate is more rapid in tension than that in compression, an asymmetric stress distribution, such as the one illustrated, results. The  $S=10$  in figure 5, corresponds to a factor of ten in the stress dependence of the creep rate. For this last case, the neutral axis moves towards the compressive surface of the component [37-40]. To fully understand creep that is asymmetric in stress, creep data in both compressive and tensile loading must be obtained.

An example of nonlinear creep behavior is illustrated in figure 6 for a grade of siliconized silicon carbide which is known to nucleate cavities when subjected to a tensile load at high temperatures [41]. Cavities in the tensile portion of the bend bar do not support the applied load, a consequence of which is an internal reduction of the cross-sectional area of the test specimen on the tensile side of the flexure bar. The local stress on the material located near the cavities is higher than the average stress, and thus, the material creeps faster in this region than in the compressive section which contains no voids. The net result of this behavior is a shift of the tensile stress field towards the compressive section of the flexure specimen and a reduction of the average tensile stress in the specimen. The shift of the neutral axis can be demonstrated experimentally from a microstructural examination of the specimen

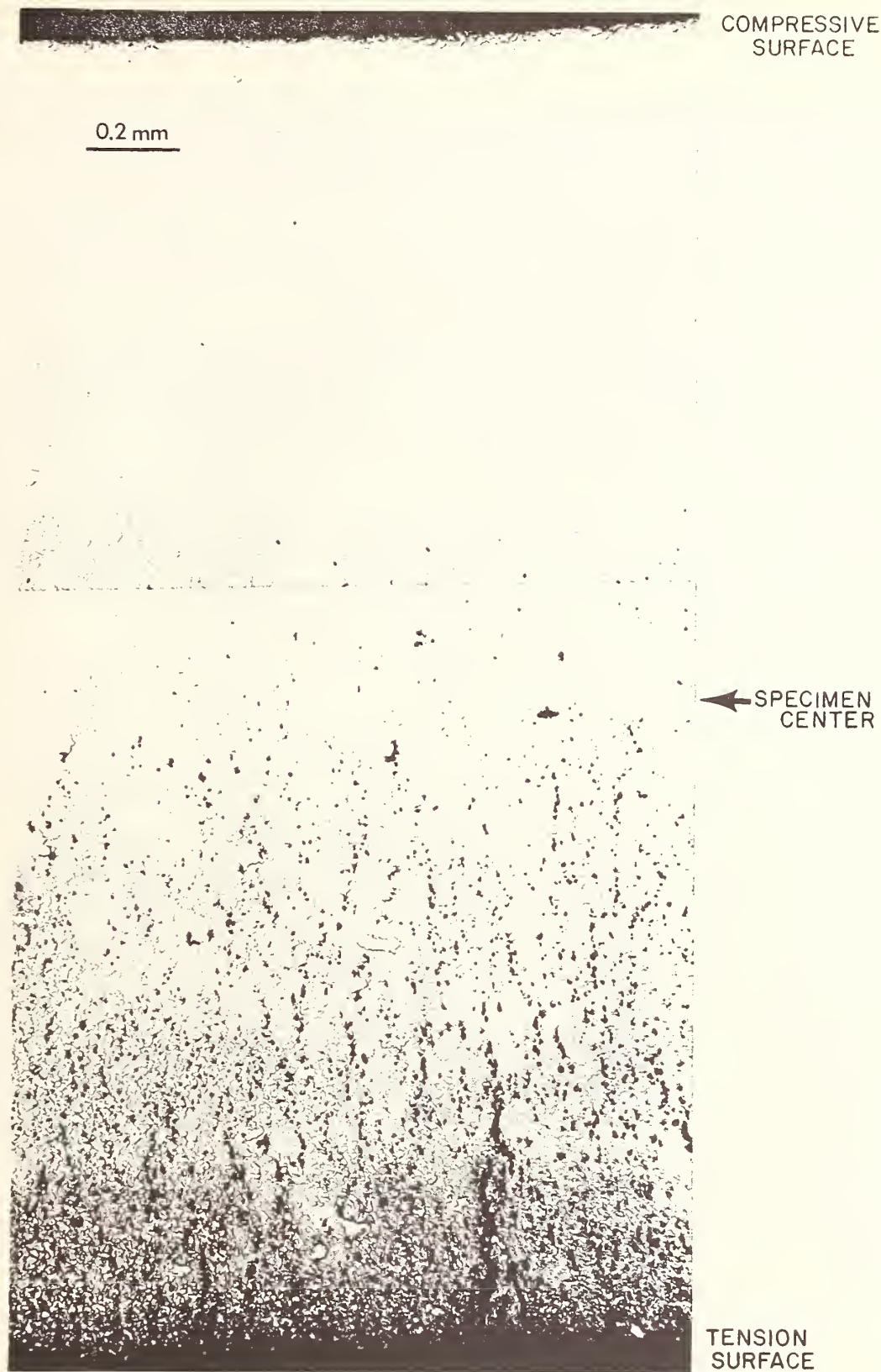


Figure 6. Cavity formation within the cross-section of a siliconized silicon carbide flexure specimen which has been tested at 1300°C and an initial applied stress of 300 MPa [41]. Note that cavity formation on the tensile side of the specimen has proceeded to beyond the original neutral axis of the specimen, indicating a shift in the neutral axis.

subsequent to testing. As illustrated in figure 6, just prior to failure cavity generation has occurred all the way across the tensile section and past the geometric center of the specimen. This shift of the stress distribution can also be demonstrated by placing parallel rows of indentations into the side surface of test bars [41]. After deformation, the position of the plane of neutral strain can be shown to have moved towards the compressive side of the specimen, suggesting a similar movement of the neutral stress axis. The transient solution to this problem has recently been analyzed by Chuang et al. [40].

Regardless of the exact process controlling creep, the fact that the stress in a component may change with time has to be factored into the design of ceramic components to obtain accurate predictions of lifetime. The reduction of the tensile stress as a function of time, for example, gives rise to a stress threshold for failure, as the stress in the tensile surface decreases [16-17]. Our understanding of bending stresses and their role in the creep rupture process is still at an early stage of development and work is needed to elucidate material behavior in multi-axial stress fields. Although some steady-state solutions of creep in flexure have been obtained, transient state creep analyses are also needed. Such transient state creep solutions have recently been obtained by Chuang et al. [40] for beams in flexure, but other stress state configurations will be needed for practical lifetime predictions. In addition, practical analyses for creep rupture of ceramic materials will require creep measurements to be made in both tension and compression to characterize the material behavior in "pure" stress states, before more complex biaxial stress states can be understood. Measurements in the tensile configuration are especially needed, because, at present, very little definitive work has been conducted on structural ceramics using tensile testing.

In addition to the discussion above, the relation between damage mechanisms and creep rates will have to be studied more fully to develop a fundamental understanding of the factors that determine the reliability of ceramic materials at elevated temperatures. The incorporation of damage processes into theories of creep have been pursued by only a few authors, see for example ref. [42]. Two facts emerge from these studies. First, damage and creep are interrelated: creep is affected by the damage process, and visa versa. Second, each damage mechanism is controlled by a distinct set of equations that determines the relation between the creep and the damage processes, and ultimately, the rupture time. In this regard, Ashby and Dyson [42] have shown that by combining different damage mechanisms with damage theory, the time-to-failure for metallic materials can be expressed in terms of a Monkman-Grant-type equation. The dependence of the Monkman-Grant coefficient on stress and temperature depends on the particular mechanism responsible for creep-rupture. The value of the coefficient is inversely related to the tolerance of the material to strain at failure. Analyses, such as that presented by Ashby and Dyson [42], have yet to be applied in a systematic way to ceramic materials.

## SUMMARY

Concepts of reliability are well established for room-temperature applications of ceramic materials. The assumption that the failure originates from pre-existing flaws is supported by a considerable body of experimental data. Based on this assumption, structural reliability

dictates control of the flaws present in a structural material and control of the external conditions (stress, environment, and temperature) that lead to the growth of flaws and eventually to component failure. There is a substantial body of theory to deal with room-temperature failure, which is currently being applied in both low- and high-temperature structural applications.

At high temperature the situation is somewhat different. If the applied stresses are greater than a threshold stress for crack growth, then failure also depends on pre-existing structural flaws, in which case, the techniques developed for failure prediction at room temperature can also be applied to high-temperature behavior. However, in these cases crack propagation may be accompanied by crack-tip creep processes, which will modify the methodology somewhat. In addition, the time-dependence of the stress, both the applied stress and the creep-modified stress state, now becomes an important variable.

When the applied stresses are less than the threshold for crack growth, pre-existing flaws may become benign with failure occurring from flaws that are generated by the high-temperature processes. Concepts of reliability in this creep-rupture regime must be based on these flaw populations, which implies an understanding of the flaw generation, flaw growth and linkage processes. Empirical descriptions of lifetime, however, are available for this regime of material response: failure time and minimum creep rate appear to be related by a Monkman-Grant-type relationship. To obtain a deeper understanding of the failure process, theoretical studies are required to relate the coefficients for these Monkman-Grant relations to the physical process occurring during creep rupture. Also, a larger data base is needed to test the theories that have been developed.

When non-uniform stresses are present in a component, such as the bending stresses in a flexural test specimen, the applicability of current lifetime prediction schemes are questionable, because of the redistribution of these stresses with time. Stress no longer becomes a design constant, but rather becomes part of the lifetime analysis. As indicated above, creep-modifications to the stress state also influence the manner in which high-temperature data is obtained, i.e., shifts in the neutral axis of flexural test specimens with time. Our understanding of these processes is in an early stage. Although theoretical analyses of the creep problem in bending are available for steady state creep, and are just becoming available for transient state creep, the dependence of creep on damage accumulation mechanisms has still to be clarified for practical ceramics. Finally, to fully understand the behavior of materials that are subjected to complex, time-dependent stress states, creep data are required in "pure" stress states (for example, both compression and tension as a minimum), and most likely, in mixed stress states as well.

Acknowledgement: The authors are pleased to acknowledge the support of the U.S. Department of Energy, Fossil Energy Materials Program (ERF) and U.S. Department of Energy, Advanced Heat Engines Project (SMW).

## REFERENCES

1. S.M. Wiederhorn and E.R. Fuller, Jr., in "Ceramic Materials and Components for Engines," edited by W. Bunk and H. Hausner, Verlag Deutsche Kermische Gesellschaft, 1986, pp. 911-929.
2. Metals Handbook, 8th edition, Vol. 1, T. Lyman ed., American Society for Metals, Novelty, OH (1961).
3. S.M. Wiederhorn and N.J. Tighe, J. Am. Ceram. Soc. 66, 884-889 (1983).
4. S.W. Freiman, J.J. Mecholsky, W.J. McDonough, and R.W. Rice, in Ceramics for High Performance Applications II, edited by J.J. Burke, E.M. Lenoe, and R.N. Katz, Brook Hill Publishing Co., Chestnut Hill, MA, 1069-76 (1978).
5. S.M. Wiederhorn and N.J. Tighe, J. Mater. Sci. 13, 1781-1793, (1978).
6. J.E. Ritter, Jr., S.M. Wiederhorn, N.J. Tighe and E.R. Fuller, Jr., in Ceramics for High Performance Applications III, Reliability, edited by E.M. Lenoe, R.N. Katz and J.J. Burke, Plenum Press, New York, 503-533 (1983).
7. F.F. Lange, S.C. Singhal, and R.C. Kerznicki, J. Am. Ceram. Soc. 60, 249-252, (1977).
8. S.M. Wiederhorn, B.J. Hockey, R.F. Krause, Jr., and K. Jakus, J. Mater. Sci. 21, 810-824 (1986).
9. M. Matsui, T. Soma and I. Oda, in Advances in Ceramics, Vol. 12: Science and Technology of Zirconia, II, edited by N. Claussen, M. Rühle and A.H. Heuer, Am. Ceram. Soc., Columbus, OH, 371 (1984).
10. N. Claussen, Mater. Sci. Eng. 71, 23-38 (1985).
11. J.E. Ritter, Jr., Yogya-Kyokai-Shi 93, 341-348 (1985).
12. J.E. Ritter, Jr., in Fracture Mechanics of Ceramics, Vol. 4, edited by R.C. Bradt, D.P.H. Hasselman and F.F. Lange, Plenum Press, New York, 667-686 (1978).
13. R.W. Davidge, J.R. McLaren and G. Tappin, J. Mater. Sci. 8, 1699-1705 (1973).
14. S.M. Wiederhorn and E.R. Fuller, Jr., Mat. Sci. and Engr. 71, 169-186 (1985).
15. A. Paluszny, Proc. Workshop on Ceramics for Advanced Heat Engines, Orlando, FL, January 24-26, 1977, in ERDA Rep. CONF-770110, pp. 231-246 (Energy Research and Development Administration).
16. G. Grathwohl, in Proc. 2nd Intl. Conf. on Creep and Fracture of Engineering Materials and Structures, edited by B. Wilshire and D.R.J. Owen, Pineridge Press, Swansea, UK, 565-577 (1984).
17. A.G. Evans, Mater. Sci. Eng. 71, 3-21 (1985).
18. B.J. Dalgleish, E.B. Slamovich and A.G. Evans, J. Am. Ceram. Soc. 68, 575-581 (1985).
19. M.H. Lewis, B.S.B. Karunaratne, J. Meredith and C. Pickering, in Creep and Fracture of Engineering Materials and Structures, edited by B. Wilshire and D.R.J. Owens, Pineridge Press, Swansea, 365-379 1981.
20. G.D. Quinn, in Methods of Assessing the Structural Reliability of Brittle Materials, edited by S.W. Freiman and C.M. Hudson, ASTM Spec. Tech. Publ. 844, 177-193 (1984).
21. E.J. Minford and R.E. Tressler, J. Am. Ceram. Soc. 66, 338-340 (1983).
22. R.E. Tressler, E.J. Minford and D.F. Carroll, in Creep and Fracture of Engineering Materials and Structures, edited by B. Wilshire and D.R.J. Owen, Pineridge Press, Swansea, 551-563 (1984).
23. E.R. Fuller, Jr., S.M. Wiederhorn, N.J. Tighe, and L. Chuck, Mater. Sci. Eng. 71, 209 (1985).

24. L. Chuck and E.R. Fuller, Jr., to be published.
25. W. Blumenthal and A.G. Evans, *J. Am. Ceram. Soc.* **67**, 751-759 (1984).
26. R.L. Tsai and R. Raj, *Acta Metall.* **30**, 1043-1058 (1982).
27. J.R. Porter, W. Blumenthal and A.G. Evans, *Acta Metall.* **29**, 1899-1906 (1981).
28. C.H. Hsueh and A.G. Evans, *Acta Metall.* **29**, 1907-1977 (1981).
29. A.G. Evans and A.S. Rana, *Acta Metall.* **28**, 129-141 (1980).
30. M.D. Thouless and A.G. Evans, *J. Am. Ceram. Soc.* **67**, 721-727 (1984).
31. M.D. Drory and A.G. Evans, *J. Am. Ceram. Soc.* **67**, 727-731 (1984).
32. J.E. Marion, A.G. Evans, M.D. Drory and D.R. Clarke, *Acta Metall.* **31**, 1445-1457 (1983).
33. A.G. Evans and W. Blumenthal, in *Fracture Mechanics of Ceramics*, Vol. 6, edited by R.C. Bradt, A.G. Evans, D.P.H. Hasselman and F.F. Lange, Plenum Press, New York, 423-448 (1983).
34. F.C. Monkman and N.J. Grant, *Proc. ASTM* **56**, 593-620 (1956).
35. R. Kassowsky, D.G. Miller, and E.S. Diaz, *J. Mater. Sci.* **15**, 601-610 (1980).
36. S.M. Johnson, B.J. Dalgleish and A.G. Evans, *J. Amer. Ceram. Soc.* **67**, 759-763 (1984).
37. H. Cohrt, G. Grathwohl and F. Thümmeler, *Res. Mechanica*, **10**, 55-71, (1984).
38. T. Fett, *Res Mechanica*, in press.
39. T.-J. Chuang, *J. Mater. Sci.* **21**, 165-175 (1986).
40. T.-J. Chuang, S.M. Wiederhorn, and C.F. Chen, to be published in *Proc. 3rd Intl. Conf. on Creep and Fracture of Engineering Materials and Structures*, Swansea, UK, April 1987.
41. S.M. Wiederhorn, L. Chuck, E.R. Fuller, Jr. and N.J. Tighe, in *Tailoring Multiphase and Composite Ceramics*, *Materials Science Research*, Vol. 20, edited by R.E. Tressler, G.L. Messing, C.G. Pantano, and R.E. Newnham, Plenum Press, 755-773 (1986).
42. M.F. Ashby and B.F. Dyson, in *Advances in Fracture Research*, Vol. 1, edited by S.R. Valluri, D.M.R. Taplin, D. Rama Rao, J.F. Knott and R. Dubey, Pergamon Press, New York, 3-30 (1984).

AN ULTRASONIC STUDY OF CERAMICS FROM THE GREEN STATE  
TO FULLY FIRED

A. L. Dragoo  
National Bureau of Standards

ABSTRACT

Ultrasonic measurements were investigated as a means for detecting hard agglomerates in alumina samples during processing from green state to fully dense. A powder consisting of hard agglomerates was prepared by calcining a spray-dried alumina powder. Longitudinal and shear wave velocities were measured in green state, bisque fired (1000 °C, 20 h) and fully dense (1465 °C, 12 h) alumina samples. Ultrasonic signals were coupled into the green state samples by means of an elastomer which required minimum contact pressure. The sound velocity measurements were compared with measurements of density and pore size distribution. For the green and bisque state samples significant differences were observed between samples formed from hard agglomerates and those formed from an uncalcined ("normal") spray-dried powder. Dense state samples obtained from both types of powder yielded equivalent sound velocities and densities. Mercury porosimetry measurements indicated that small pores were removed or sealed off in passing from the green to the bisque state, and that pore size was substantially reduced in passing from the bisque to the dense state. Green state samples from normal and calcined powders showed differences in pore size distributions at finer pore sizes, i.e., below 20 nm.

# AN ULTRASONIC STUDY OF CERAMICS FROM THE GREEN STATE

TO FULLY FIRED.

A. L. Dragoo  
National Bureau of Standards  
Gaithersburg, Maryland 20899  
USA

The objective of the present study was to investigate the use of sound velocity measurements as a means for the determination of the effect of soft and hard agglomerates on the sintering of alumina compacts. The effects on the density and elastic moduli were investigated for compacts at three stages of sintering: green-state or unfired, bisque or partially fired, and fully fired. In addition to ultrasonic characterization of the samples, the density and porosity of the samples were determined.

## EXPERIMENTAL

The procedure for the preparation of samples is illustrated by the flowchart in Fig. 1. 500 g of 99.99 percent alumina powder, having the cumulative particle size distribution, shown in Fig. 2, as determined by x-ray sedimentation, and 3.18 g of  $\text{Mg}(\text{NO}_3)_2 \cdot (6\text{H}_2\text{O})$  were dispersed in 1 L of water containing small amounts of polyvinyl alcohol (PVA) as a binder and glycerol as a plasticizer. The slurry was spray-dried to form agglomerated spheres. A micrograph of the spray-dried powder is shown in Fig. 3. The spray-dried powder was divided into equal portions, and one portion was calcined at 1000 °C for 12 h to form "hard" agglomerates. Calcination resulted in partial sintering of the material within the spherical particles but not between them.

Two sets of compacted samples were prepared. The first set was formed from the uncalcined powder. These samples are termed "normal samples" and are designated by an "N." The second set was prepared from the hard agglomerate powder. These samples are termed "calcined samples" and are designated by a "C." Disks, approximately 3.2 mm thick and 28.6 mm in diameter, were formed by uniaxial compaction with pressures up to 206 MPa. Each of the two sets of samples were subdivided into three groups of samples: green-state samples; bisque-fired samples which were sintered

at 1000 °C for 20 h; and dense samples which were sintered at 1465 °C for 12 h.

The samples were characterized by ultrasonic measurements, density measurements and mercury porosimetry. Sound velocity measurements were carried out on pairs of samples from each of the groups for a total of 12 samples.

Sample densities were determined for the green samples by a dry-weight dimensional method and for the sintered samples by a liquid immersion technique. The densities are listed in Tables 1 and 2. Accuracy of the density values for the green samples was estimated to be better than  $\pm 1$  percent and for the sintered samples,  $\pm 0.1$  percent. The density of two dense samples were also determined with a helium pycnometer.

Mercury intrusion porosimetry was used to measure the pore size distribution and the bulk and structural densities for the three types of ceramic samples. The results of those measurements are summarized in Table 2. The bulk density is defined by the external volume of the material and includes both open and closed pores; the structural density includes the material plus only the closed pores in the measured volume. The three estimates of the mean pore diameter are discussed below.

#### Ultrasonic Techniques

The ultrasonic techniques used in this study have been described in detail elsewhere by Jones et al.<sup>1</sup> and only will be summarized here. Through-transmission, using separate transmitting and receiving transducers, and pulse-echo-overlap techniques were used to make time-of-flight ultrasonic measurements. The through-transmission configuration is illustrated schematically in Fig. 4.

The shear-wave transit times were measured by means of two echo-overlap procedures: through-transmission overlap for green and bisque samples and pulse-echo overlap for the dense samples. For the green and bisque

samples, a novel elastomer material,<sup>a</sup> capable of supporting shear waves at MHz frequencies, was used to dry couple the transducers to the samples. A single transducer with a viscous coupling agent was used for the dense samples.

The longitudinal-wave transit times were measured by a through-transmission technique for the green samples and by pulse-echo-overlap for bisque and dense samples. Green and bisque samples were dry coupled to the transducer by covering the surface of the sample with a natural latex elastomer (surgical glove material) followed by applying silicone oil between the elastomer and the transducer. This coupling method yielded a better longitudinal-wave signal than that obtained with the shear-wave coupling material. Dense samples were measured with a direct oil coupling.

#### Mercury Porosimetry

The measurement of pore size by mercury intrusion assumes cylindrical pore structures to establish a relationship between the applied pressure and the pore radius. Pore size distributions are obtained for fraction of total volume for per size interval and for fraction of total surface area per size interval. Median pore diameters are calculated for each distribution. These median values are listed in Table 2 under the columns labelled "Med. (V)" and "Med. (A)", for volume-based and surface area-based distributions, respectively. In addition, the measurement returns an estimate of the mean pore size from the ratio of total volume, V, to total surface area, A; i.e.,  $(4V/A)$ . For very narrow pore size distributions the three estimates of the mean pore diameter are nearly equivalent. For broad or multimodal distributions the three estimates are disparate, with the volume distribution yielding the highest estimate.

#### RESULTS AND DISCUSSION

The relationship between velocities to sample density for shear-waves and

---

<sup>a</sup>Proprietary material provided to NBS for test and evaluation by B. Boro Djordjevic, Martin-Marietta Laboratories, Baltimore, MD.

longitudinal waves are shown Fig. 5 and 6, respectively. For both types of waves, there is nearly an order-of-magnitude increase in sound velocity from the green to the dense state. The error bars in the figures are a combination of between sample variations, dimensional uncertainties, and ultrasonic transit-time errors. The accuracy of the velocity measurement technique was determined by making reference measurements on an aluminum alloy and on single-crystal quartz and was found to be better than 1 percent for the dense samples.

As shown in Fig. 5 and 6 and by the elastic moduli in Table 1, the ultrasonic measurements are clearly different for normal and calcined samples in the green and bisque states. For the green and bisque states, the velocities for calcined samples are markedly less than those for normal samples, whereas dense state samples were similar with respect to both density and sound velocities. The sound velocities are a function both of the density of the sample and its processing history. For green state samples, different amounts of binder in the normal and calcined samples may be significant. Kupperman and Karplus<sup>2</sup> showed that green-state ceramics of different densities, as a result of different forming pressures, manifest an increase in velocity with density which is comparable to that observed here. However, in this work a single forming pressure was used, with the calcined samples yielding slightly lower densities than the normal samples.

Elastic moduli and Poisson's ratio were calculated for each sample, assuming sample isotropy.<sup>3</sup> The results are given in Table 1. The propagated errors in the calculation of Young's moduli are, for worst case,  $\pm 2$ , 8 and 3 percent for green, bisque and dense states, respectively. For the shear moduli, the worst case errors are  $\pm 2$ , 7 and 2 percent; for the bulk moduli,  $\pm 3$ , 13 and 4 percent. Between sample variation contributed the largest portion of the uncertainty in each case.

Sample (elastic) homogeneity and isotropy were measured ultrasonically on one sample in each sample pair. Longitudinal wave homogeneity was evaluated from measurements at the center and 3 peripheral positions.

The standard errors were 2, 1.5 and 0.3 percent for green, bisque and dense states, respectively. Such an increase is expected since homogeneity is presumed to improve as sintering proceeds. Sample isotropy was evaluated by rotating the shear polarization direction at the center of each sample in increments of 45° from an arbitrary initial orientation. The anisotropy was within measurement precision for shear waves.

The porosimetry results in Table 2 were obtained from measurements on a single specimen of each type which were broken into 2 to 4 pieces. The relative errors in the mean pore diameters are about 20 percent for the green and bisque samples, with the exception of Med.(A) and (4V/A) values for the green calcined samples which are about 80 percent, and for the dense samples, about 40 percent. The uncertainties for the bulk and structural densities are about 3 percent for all cases. These estimates of the uncertainties do not include a contribution from sample-to-sample variation.

The calcined and normal samples differ significantly only in the case of the green state samples. For these samples the calcined and normal state samples differ in their porosity, pore size distributions and mean pore size. The calcined sample showed slightly lower bulk densities, indicating more porosity. The three estimates of the mean pore size for this sample are slightly larger than those for the normal sample. The calcined sample showed a tendency to delaminate near the midline of the sample. The large uncertainties in Med.(A) and (4V/A) for the calcined sample are associated with significant variation in the observed pore size distribution at small pore diameters.

The normal green sample exhibited surface area distributions with strong modes near 100 and 5 nm; i.e., toward the upper and lower extremes of the size range. Since the importance of the small pores is reduced in the volume distribution which emphasized the mode near 100 nm,

Med.(V) >> Med.(A), normal green state  
is obtained in Table 2. The normal green state sample yielded more reproducible pore size distributions than the calcined sample.

For the bisque and dense states, the porosity characteristics of calcined and normal samples became nearly identical. The surface area-based pore size distributions for both types of bisque fired samples showed a very strong mode centered near 100 nm and a weak mode centered between 5 and 10 nm. The dense state samples showed a single mode centered near 10 nm.

The porosimetry results indicate that small pores were eliminated or sealed off during processing from the green state to the bisque state. From the bisque state to the dense state, it is evident that pore size is reduced. Comparing the porosimetry results and the ultrasonic results, the sound velocity measurements are expected to be affected primarily by the largest pores, whereas porosimetry measurements can detect both large and small open pores. On the other hand, sound velocities are expected to be more sensitive to the continuity and rigidity of the material structure.

From the standpoint of sintering process, from green to bisque state, the small increases in sound velocities and elastic moduli suggest that the material structure became more rigid and continuous, probably as a result of the loss of binder and the formation of necks between particles. Also, fine pores were eliminated or sealed off. From bisque to dense state, pore size was markedly reduced and the identity of the hard agglomerates was lost.

#### CONCLUSIONS

Shear and longitudinal sound velocities were measured and elastic moduli determined for green, bisque and dense state alumina samples. Dry coupling of shear waves into green state compacts was accomplished with an elastomer which required minimum contact pressure. Ultrasonic measurements were able to detect the presence of hard agglomerates in green and bisque state samples but not in the dense state samples. This results suggests the possible use of ultrasonic measurements to monitor the presence of hard agglomerates in green state materials.

Mercury porosimetry measurements indicated that small pores were eliminated or sealed off during the bisque-firing and that the pore size was substantially reduced for sintering to full density.

#### Acknowledgements

The author recognizes the major contribution of M. P. Jones who, as a graduate student at Johns Hopkins University, worked in collaboration with C. R. Robbins, of the Ceramic Powder Characterization Group, and with G. V. Blessing, of the Ultrasonic Standards Group at NBS, to prepare many of the samples and to conduct the ultrasonic measurements. The porosimetry measurements by C. R. Robbins are also recognized. The early suggestion of this research problem and discussions with W. Coblentz (present address: Norton Company, Worcester, MA) were important in the formation of research program. This work was supported by the Office of Nondestructive Evaluation at the National Bureau of Standards.

DIMENSIONAL DENSITY, ELASTIC MODULI AND POISSON'S RATIO  
(P. RATIO) OF NORMAL (N) AND CALCINED (C) SPRAY-DRIED ALUMINA

POWDERS

Sample State	Density (g/cm <sup>3</sup> ) Dimensional	Elastic Moduli (GPa)			
		Young's	Shear	Bulk	P. Ratio
Green-N	1.93	2.6	1.7	0.6	-0.23
Green-C	1.88	0.6	1.1	0,1	-0.72
Bisque-N	2.12	29.0	13.0	11.0	0.07
Bisque-C	2.00	11.0	6.6	2.0	-0.14
Dense-N	3.91	400.0	162.0	248.0	0.23
Dense-C 1465	3.92	405.0	164.0	256.0	0.23

SAMPLE DENSITIES AND PORE DIAMETERS FOR SPECIMENS FORMED FROM NORMAL (N)  
AND CALCINED (C) SPRAY-DRIED ALUMINA POWDERS

Sample State	Dimens.	Density (g/cm <sup>3</sup> )			Pore Diameter (um)		
		Bulk	Struc.	He Pycn.	Med.(V)	Med.(A)	(4V/A)
Green-N	1.93	1.87	3.57		0.075	0.018	0.039
Green-C	1.88	1.82	3.44		0.101	0.062	0.070
Bisque-N	2.12	2.04	3.71		0.106	0.091	0.069
Bisque-C	2.00	1.92	3.66		0.108	0.092	0.071
Dense-N	3.91	3.74	3.80		0.008	0.006	0.008
Dense-C							
1465	3.92	3.72	3.80	3.952	0.008	0.005	0.008
1500				3.931			

Dimens. = density determined from dimensional measurements on weighted specimens.

Bulk = bulk density obtained from Hg intrusion porosimetry.

Struc. = structural density obtained from Hg intrusion porosimetry.

He Pycn. = density obtained using He pycnometer.

Med.(V) = median pore diameter based on distribution of pore volume.

Med.(A) = median pore diameter based on distribution of pore area.

(4V/A) = average pore diameter calculated from total pore volume (V) and total pore area (A).

1. Jones, M.P.; Blessing, G.V.; Robbins, C. R. Dry-Coupled Ultrasonic Elasticity Measurements of Sintered Ceramics and Their Green States. Mater. Eval. 44(7): 859-62; 1985.

2. Kupperman, D. S.; Karplus, H. B. Ultrasonic Wave Propagation Characteristics of Green Ceramics. Am. Ceram. Soc. Bull. 63(12): 1505-09; 1984.

3. See, e.g., Kolsky, H. Stress Waves in Solids. New York: Dover Publications; 1963.

# Al<sub>2</sub>O<sub>3</sub> SAMPLE PREPARATION

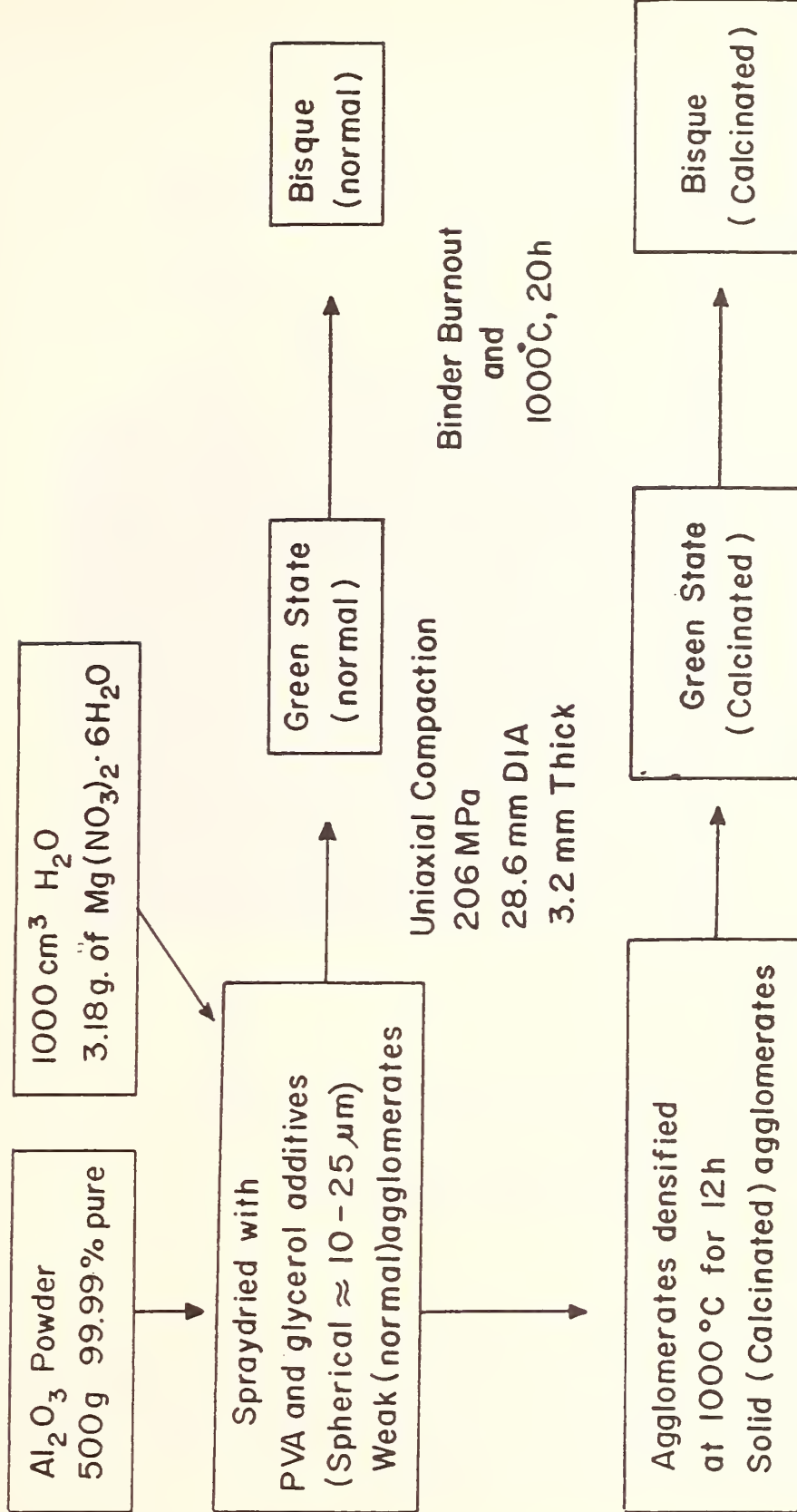


Figure 1--Flowchart for the preparation of alumina samples containing soft and hard agglomerates.

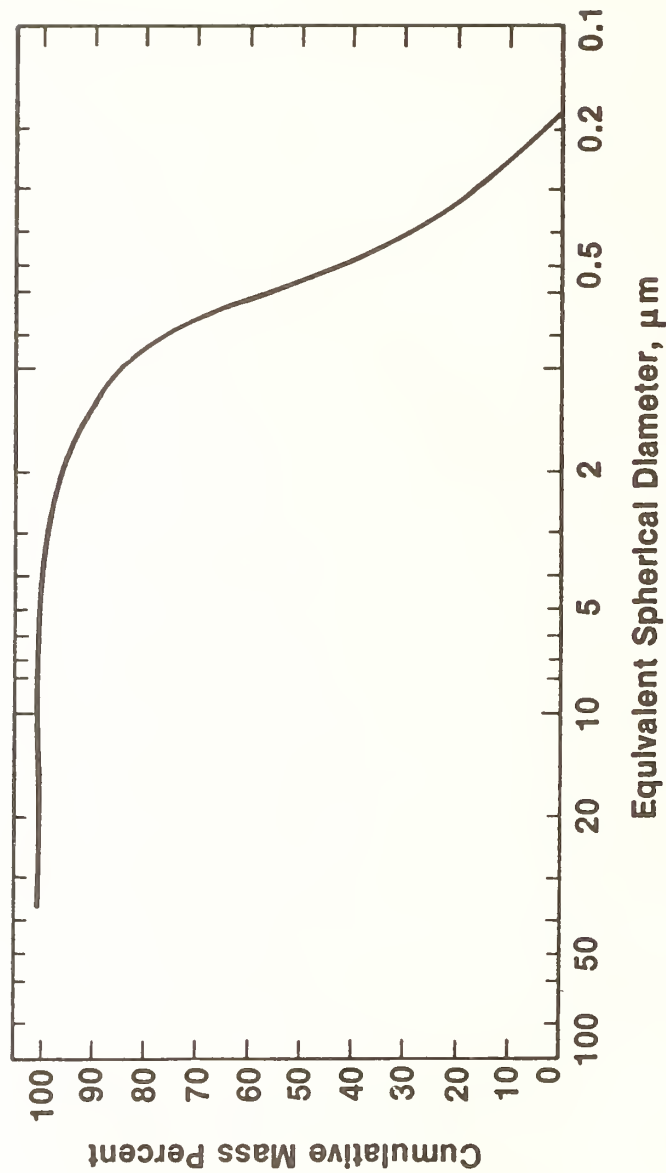


Figure 2--Cumulative particle size distribution for alumina starting powder as obtained with x-ray sedigraph. Cumulative percent finer is plotted versus the Equivalent Spherical Diameter (ESD), in  $\mu\text{m}$ , calculated from Stokes Law for settling of spheres.

## SPRAY-DRIED PARTICLES

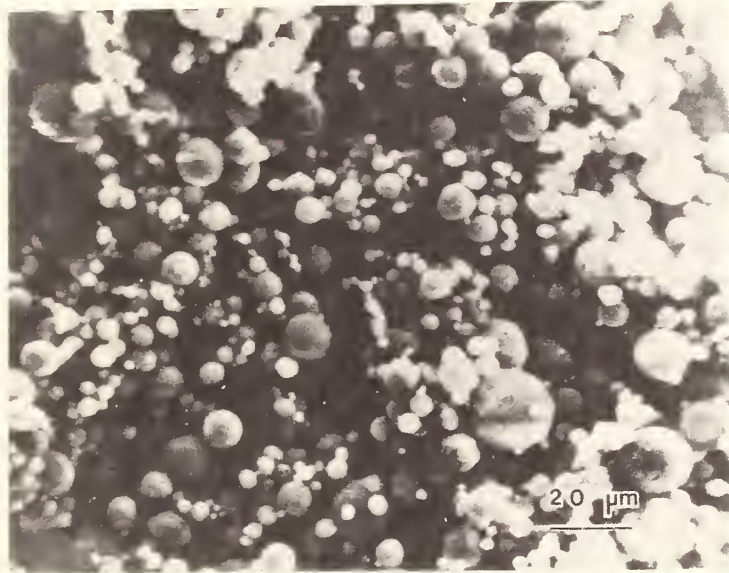


Figure 3--Micrograph of spray-dried alumina powder.

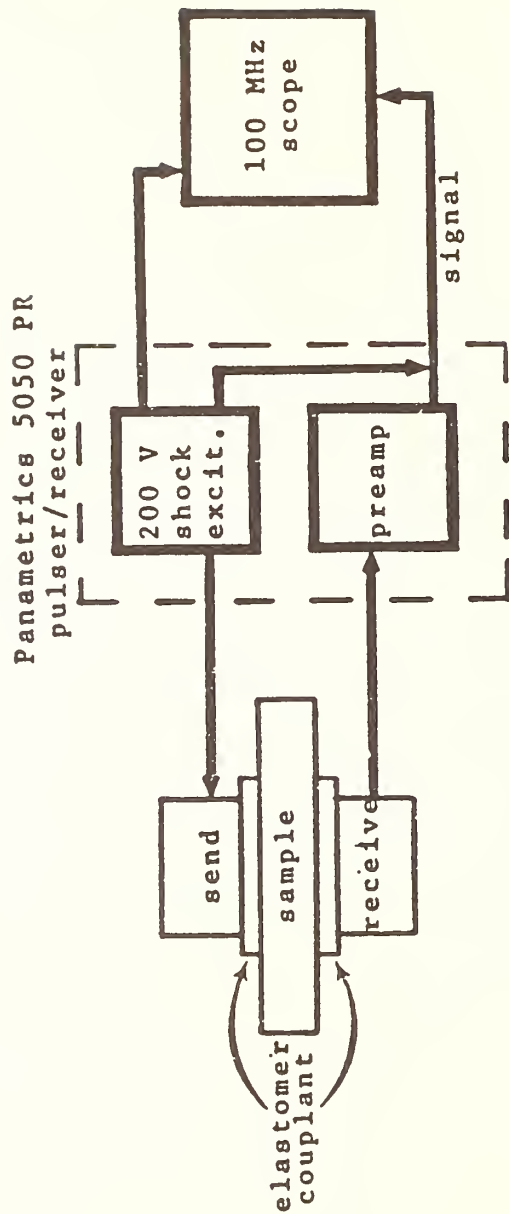


Figure 4--Block diagram of apparatus used in the through-transmission pulse-echo technique.

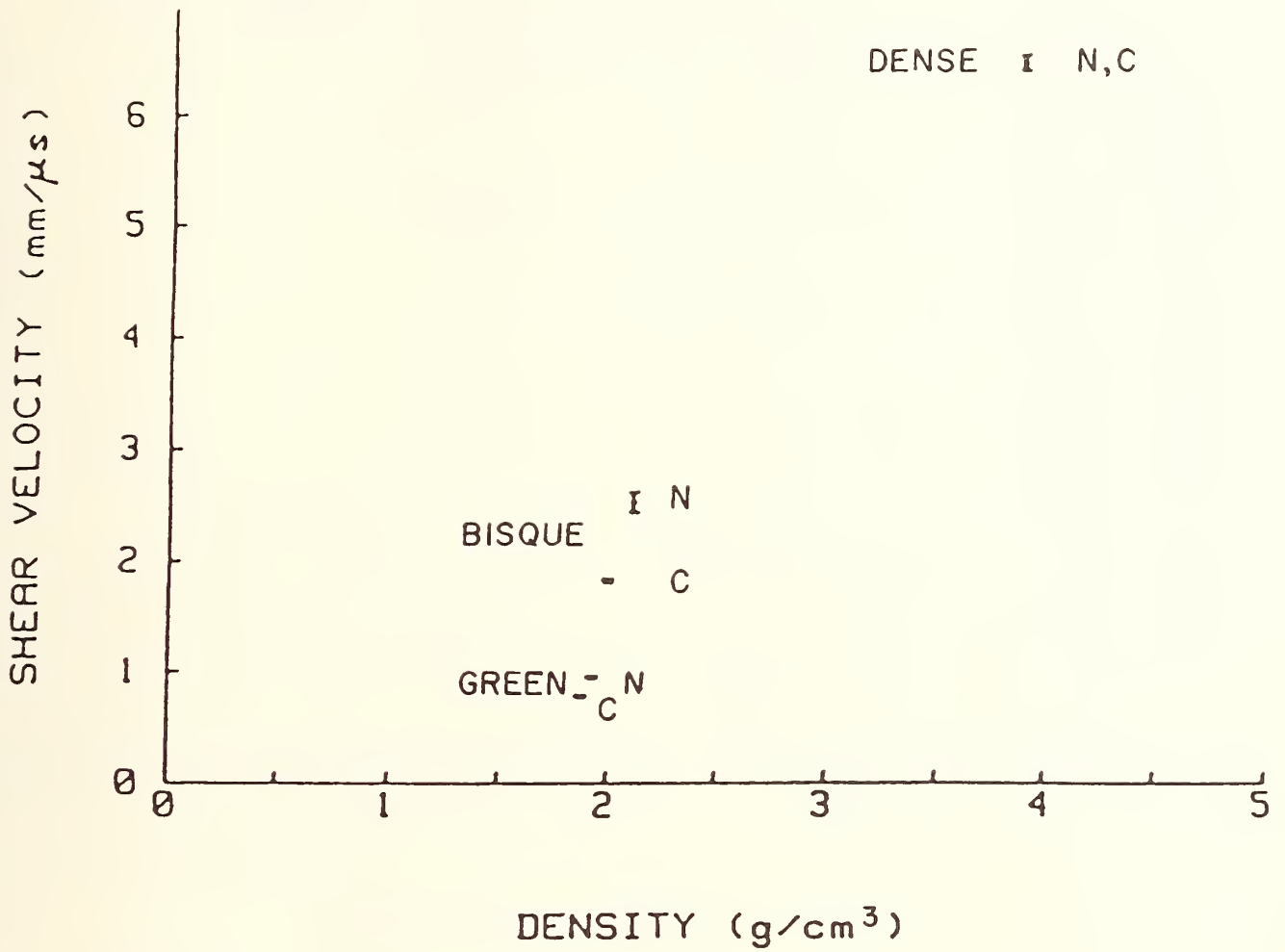


Figure 5--Ultrasonic shear wave velocity vs. sample density for the green, bisque and dense states, with both normal (N) and calcined (C) processed spray-dried powders.

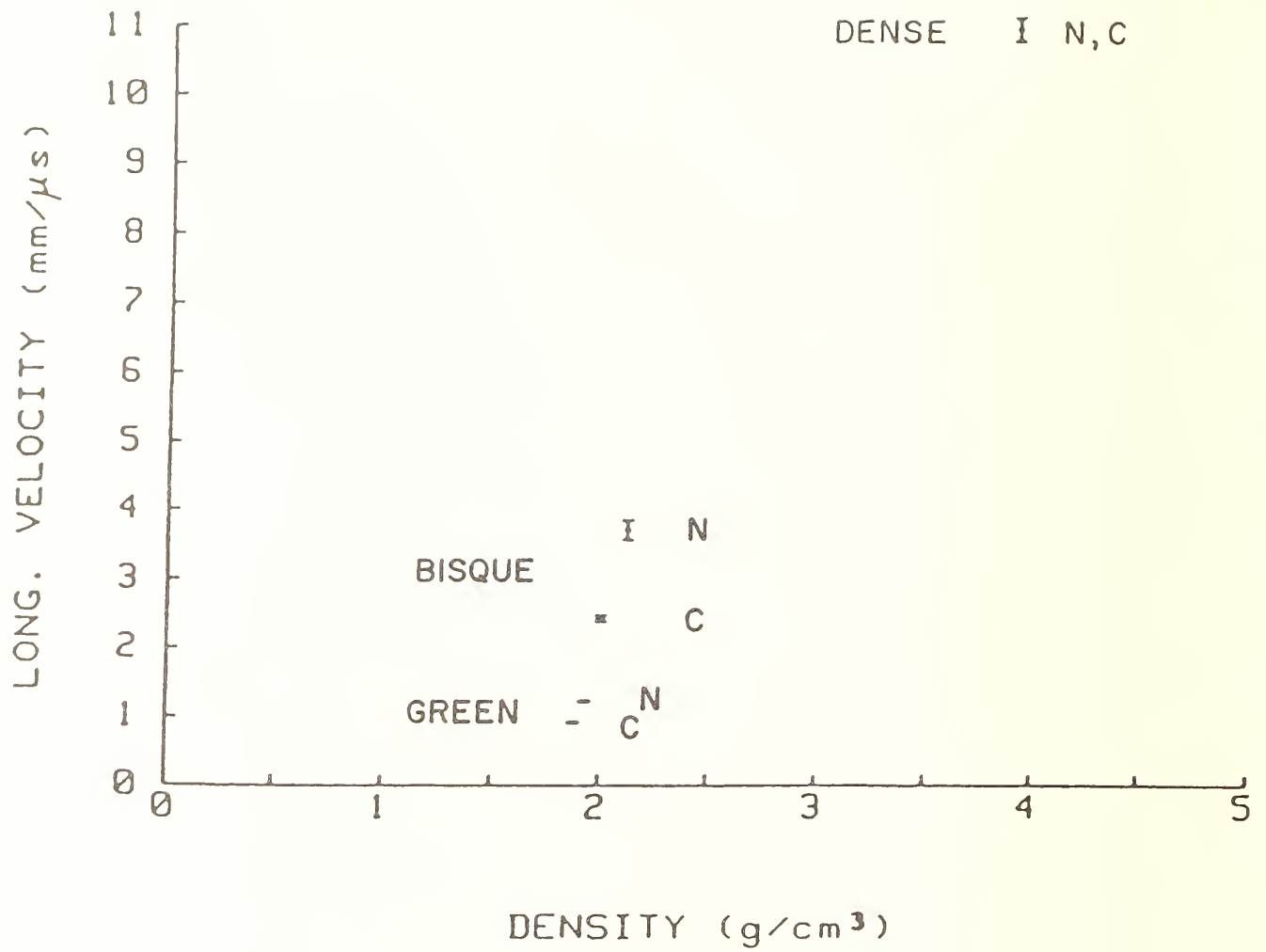


Figure 6--Ultrasonic longitudinal wave velocity vs. sample density for the green, bisque and dense states with both N and C type powders.

NONDESTRUCTIVE CHARACTERIZATION  
OF CERAMIC MATERIALS: THERMAL WAVES

G. S. White  
Ceramics Division  
Institute for Materials Science  
and Engineering  
National Bureau of Standards  
Gaithersburg, MD 20899

and

E. H. LeGal LaSalle\*  
Laboratoire d'Optique Physique  
ESPCI  
10 Rue Vauquelin  
75005 Paris, France

ABSTRACT:

Investigation of thermal wave techniques for application to the nondestructive evaluation (NDE) of ceramic materials is in its early stages. Thermal waves have the advantage of having an adjustable thermal diffusion length, which determines the probe length, and of being a surface and near surface probe. Research at NBS has shown this technique to be sensitive to some forms of surface polishing damage in vitreous silica and to variations in porosity of alumina.

INTRODUCTION:

Although many techniques for nondestructive evaluation (NDE) have been developed, and are in use, for testing metals, the corresponding progress for ceramics has been limited. The principal reason behind this lack of progress in ceramic materials is the brittle nature of these materials; because of their low fracture toughness (on the order of 1 to 10 MPam<sup>1/2</sup> compared to ≈100

MPam<sup>1/2</sup> for metals), catastrophic flaws are measured in tens of micrometers rather than in millimeters, as for metals. In addition, defects which result in failure of ceramics usually lie on the surface. Therefore, NDE techniques which measure bulk properties are often inappropriate for finding defects in ceramics. In this paper, application of thermal wave techniques to the NDE of ceramic materials is discussed and related to the concerns listed above. Two examples relating to recent NBS research are discussed.

#### THERMAL WAVE PROCEDURE:

The concept of thermal waves as a material probe has developed over the past few years<sup>1</sup> with contributions from several research groups. The following picture has been reached. When a periodic heating source is applied to a material, the resulting periodic heat flow can be described as highly damped travelling waves.

$$S = A \exp(j\omega t - (1+j)x/\mu), \quad (1)$$

where  $S$  is the thermal wave signal,  $x$  is the distance traveled, and  $\mu = (2K/C\rho\omega)^{1/2}$  is the thermal diffusion length which is a function of the thermal conductivity,  $K$ , the heat capacity,  $C$ , the density of the specimen,  $\rho$ , and the angular modulation frequency of the heat source,  $\omega$ . As the strong damping component in eqn. 1 indicates, the effective depth to which such waves travel in the material depends upon the modulation frequency of the heating source;

the lower the frequency, the deeper the penetration. For most applications, the practical penetration range of the thermal waves can be considered  $\approx \mu$ .

A number of detection schemes exist which measure certain aspects of this heat flow, and two of them, the photoacoustic effect and the mirage effect, will be qualitatively described here. The photoacoustic effect signal (Fig. 1) results from thermally induced pressure variations in the atmosphere above the heated specimen which has been placed in a sealed chamber. The pressure variations drive a microphone and the resulting signal is proportional to the temperature of the specimen<sup>2</sup>. The mirage effect (Fig. 2), takes advantage of the modulation of the index of refraction gradient above or in the heated region of the specimen to deflect a probe laser beam and to produce a signal proportional to the gradient of the temperature<sup>3</sup>. Generally, the probe beam is passed through the heated atmosphere above the specimen surface without touching the specimen itself. In both of these detection techniques, the heating can be caused by any modulated source; e.g. laser, electron-beam, flashlamp, etc.

Because the thermal behavior can be described as a damped travelling wave phenomenon, the signal can be divided into two independent components: magnitude and phase. The magnitude is a measure of the strength of the signal and, therefore, reflects optical as well as thermal properties of the specimen. The phase component is a measure of the delay between the time heat is applied and the signal is detected and is much less sensitive to optical features<sup>4</sup>.

As eqn. 1 implies, the interrogation range of the thermal waves depends not only upon the modulation frequency of the heat source, but also upon thermal parameters of the specimen under study. Table I compares  $\mu$  at two different frequencies for three commonly used ceramic materials: vitreous silica,

alumina, and silicon carbide. There is an order of magnitude change in  $\mu$  when the specimen is changed from vitreous silica to silicon carbide, and this change is independent of any experimental parameters. In principle, the values of  $\mu$  can be maintained from material to material by variations in  $\omega$  although, in practice, the frequency capabilities of the modulator may not have the necessary range.

Although the understanding of thermal waves has greatly improved, only recently have there been systematic attempts to use this understanding in the NDE of ceramic materials. Because thermal waves are essentially a surface and near surface effect and because the thermal diffusion length can be modified over a large range by changing the heating modulation frequency, thermal waves seem naturally suited to this application.

#### THERMAL WAVE APPLICATIONS:

Residual Polishing Damage: There is concern over the possible creation of residual damage resulting from surface preparation of optical components. Because thermal waves have proven useful in the interrogation of metallic and semiconductor layered specimens<sup>1,5</sup>, it is a reasonable step to use them to look for near surface residual damage in glass. The possible types of residual damage envisioned include scratches, subsurface microcracks, and residual stresses. Since the penetration depth of the thermal waves depends upon the modulation frequency of the heat source, the presence of a damaged layer with thermal properties different from those in the bulk would result in a change in the frequency dependence of the signal as the thermal waves cross the boundary between the damaged and undamaged material. The size of this change would depend upon the magnitude of the change in  $(K/\rho C)^{1/2}$ . Therefore,

one of the most direct applications of thermal wave techniques to the detection of a residual damage layer would be to measure the frequency dependence of the thermal wave signal.

Specimens, 1.2 x 1.5 x 0.21 mm, were cut from polished vitreous silica slides. The specimens were abraded with a 180 grit diamond wheel and then polished in steps using 30, 15, and 1  $\mu\text{m}$  diamond polishing compound and .3  $\mu\text{m}$  alumina powder. At each step, specimens were set aside for thermal wave investigations.

The experiments consisted of measuring the photoacoustic or mirage signals at 5 random spots on the specimen surfaces as a function of heating modulation frequency, using both photoacoustic and mirage detection techniques. The frequency range was limited by the mechanical chopper to  $20 \text{ Hz} \leq \omega \leq 250 \text{ Hz}$ . The signal from both the photoacoustic cell and the mirage system beam deflection detector was filtered in a vector lock-in amplifier. Both phase and magnitude were measured at each of the positions on the specimen surface.

Measurements were made following each of the polishing steps described above. While the actual signal magnitudes varied as a result of the polishing procedure, the results described below, obtained from the specimens which underwent final polishing, are representative of the general trends observed at each polishing step.

In Figure 3a, the signal magnitude is plotted as a function of modulation frequency using the mirage effect detection technique. In Figure 3b, the corresponding phase data are displayed. In both cases, the data are plotted versus the square root of the frequency. The frequency range covered corresponds to thermal diffusion lengths, and, hence, to penetration depths, between 25 and 100 micrometers. The line through the data points in Fig. 3a is an empirical exponential fit and shows that no discontinuity, corresponding

to a damage layer, is observed in the magnitude signal. The phase data, shown in Fig. 3b, do show a discontinuous slope at about  $f = 30$  Hz, corresponding to a penetration depth of about  $80 \mu\text{m}$ . However, because 30 Hz was at the low end of the frequency capabilities of the apparatus, this result is most likely an artifact; see below.

The photoacoustic phase data, Fig. 4b, covering the same frequency range, give no indication of the discontinuity. Similarly, the photoacoustic magnitude data (Fig. 4a), which theory predicts should be a linear function of  $1/f$  for isotropic thermal insulators<sup>2</sup>, does not suggest the presence of a damage layer. A straight line fit connects all the data for both the phase and magnitude measurements. Therefore, the preponderance of the thermal wave data has failed to give any indication of a damage layer in the depth range of 25 to  $100 \mu\text{m}$ .

However, while no damage layer has yet been observed, photoacoustic scans have shown the presence of scratches remaining from the surface treatments. Magnitude and phase line scans ( $f = 200$  Hz, penetration depth  $\approx 30 \mu\text{m}$ ) across the surface of an as-received  $\text{SiO}_2$  specimen (Figures 5a and 5b) give no indication of any defects. After grinding and polishing, a randomly positioned set of photoacoustic magnitude scans mapped out the remaining scratch shown in Figure 6. The lines in Figure 6 are spaced  $50 \mu\text{m}$  apart, indicating that the scratch is a large defect and should easily be observed by optical scattering NDE tests although a casual inspection by eye did not detect the defect prior to the photoacoustic measurements. Subsequent investigation of the polished surfaces under an optical microscope did detect a number of residual scratches. The large signal to noise ratio in the figure suggests that the photoacoustic effect has the sensitivity to detect much smaller flaws in a systematic surface scan of these specimens.

Porosity: The porosity of ceramic components has long been a quality control variable. Because  $\mu$  is a function of the effective K as well as of  $\rho$ , both of which are functions of the specimen porosity, thermal waves can be expected to be sensitive to variations in porosity. Therefore, a set of alumina specimens of varying porosity has been made and thermal wave phase and magnitude photoacoustic measurements were made as a function of frequency.

The specimens were uniaxially pressed to 103 MPa and fired in air. The firing procedure consisted of placing the specimens in the furnace at 800 C, increasing the temperature to 1600 C in approximately an hour (see Fig. 7), following which the specimens were withdrawn after various lengths of time. The specimens were then sectioned on a diamond saw and the cross-sections were potted together in epoxy for polishing, optical measurements, and photoacoustic measurements. The polishing procedure was the same as that outlined above for the surface damage tests. Because each of the specimens experienced the same surface preparation, any surface roughness effects in the thermal wave measurements are expected to be related only to variations in porosity. In addition, because no binder was used, no surface absorption effects related to partial binder burnout in the different specimens will occur.

Before the photoacoustic measurements were made, the percentage porosity of the specimens was measured using standard pore counting techniques and is expressed in percentage of the surface area taken up by pores.

Figure 8 shows magnitude measurements for the specimen removed from the furnace as soon as 1600 C was reached. Measurements were made at 5 positions on the specimen and the vertical lines show the resulting standard deviation. For this specimen, the porosity was measured as  $30.8 \pm 5.4\%$ . Figure 9 shows

the same type of data for a specimen which was held at 1600 C for 118 hr. For this specimen, the porosity was  $3.0 \pm 2.6\%$ . There are marked differences between the two sets of figures, suggesting that thermal waves do detect the difference in porosity between the two samples. Analytical interpretation of these signals is difficult because of the influence of unknown surface roughness, optical absorption, and light to heat conversion efficiencies, especially as these parameters vary with porosity changes. However, variations in these parameters are expected to be directly related to variations in porosity, since other parameters have been held constant. Therefore, the thermal wave results suggest that, at the least, the thermal wave signal could be empirically calibrated to give porosity values for a given material and processing treatment. Alternatively, thermal waves could be used to calculate thermal diffusivities as a function of porosity. Some work in this direction has already begun on other materials<sup>6</sup>.

#### SUMMARY:

The development of thermal wave techniques as NDE tools has reached the level at which practical tests need to be considered. One of the most useful applications of thermal waves would be to the NDE of ceramics, materials for which there are currently very few NDE tools.

Two applications of thermal wave NDE of ceramics have been discussed. Feasibility of using photoacoustic and mirage thermal wave techniques to detect both damage resulting from preparation of optical surfaces in vitreous silica and porosity in alumina has been investigated using photoacoustic frequency dependence measurements. While residual surface scratches were shown to be detected easily, no indication was found of a subsurface residual

damage layer in silica. On the other hand, thermal wave signals were found to be sensitive to porosity changes in alumina.

ACKNOWLEDGEMENTS:

I gratefully acknowledge the support given this work by the Office of Nondestructive Evaluation at N.B.S.

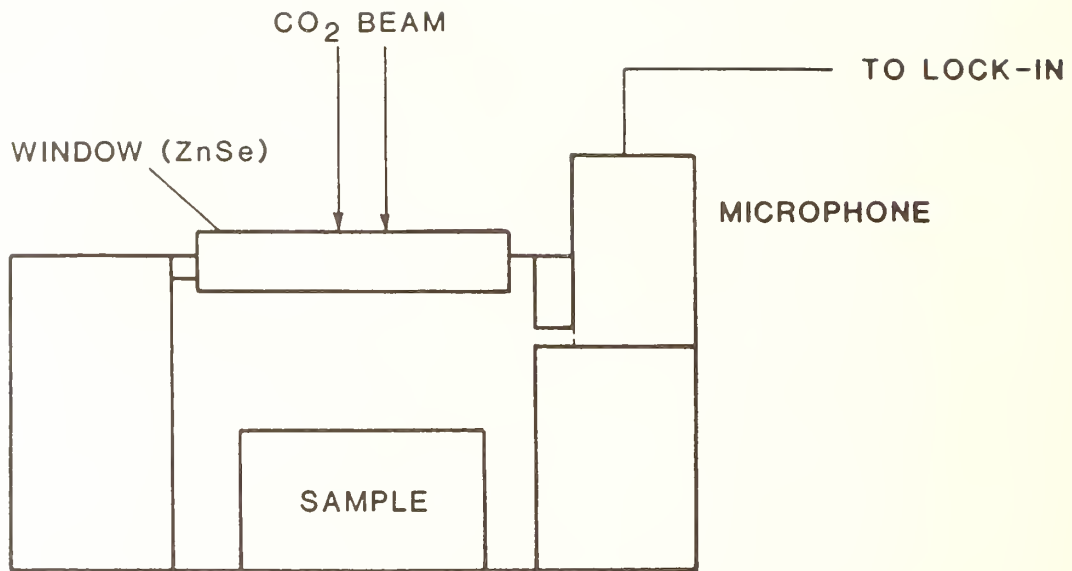
Table I:

<u>Material</u>	<u>Frequency (Hz)</u>	<u><math>\mu</math> (<math>\mu\text{m}</math>)</u>
SiO <sub>2</sub>	20	93
	2000	9
Al <sub>2</sub> O <sub>3</sub>	20	285
	2000	29
SiC	20	1000
	2000	100

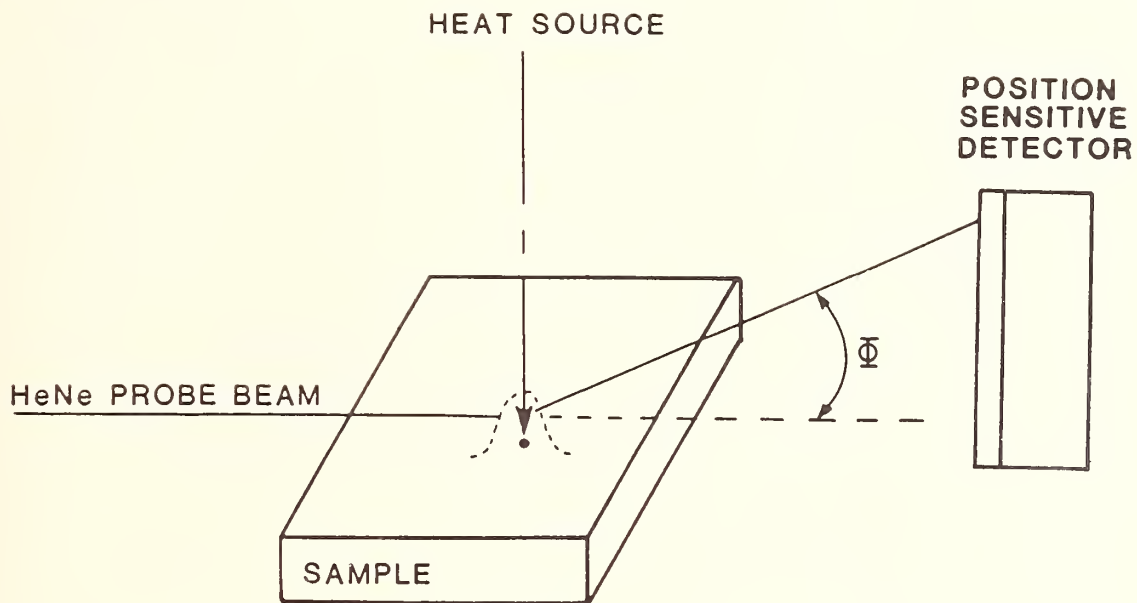
## REFERENCES

1. G. Birnbaum and G.S. White, in Nondestructive Testing, Vol. 7 (R.S. Sharpe, ed.), Academic Press, Inc. London, pp. 259-365 (1984).
2. A. Rosencwaig and A. Gersho, J. Appl. Phys. 47, 64-69 (1976).
3. L. Aamodt and J. Murphy, J. Appl. Phys. 52, 4903-4914 (1981).
4. A. Rosencwaig and G. Busse, Appl. Phys. Lett. 36 (9), 725-727 (1980).
5. A. Rosencwaig, J. Opsal and D.L. Willenborg, J. de Phys. 44 (10), C6-483-C6-489 (1983).
6. B.K. Bein, S. Krueger and J. Pelzl, Can. J. Phys. 64, 1208-1216 (1985).

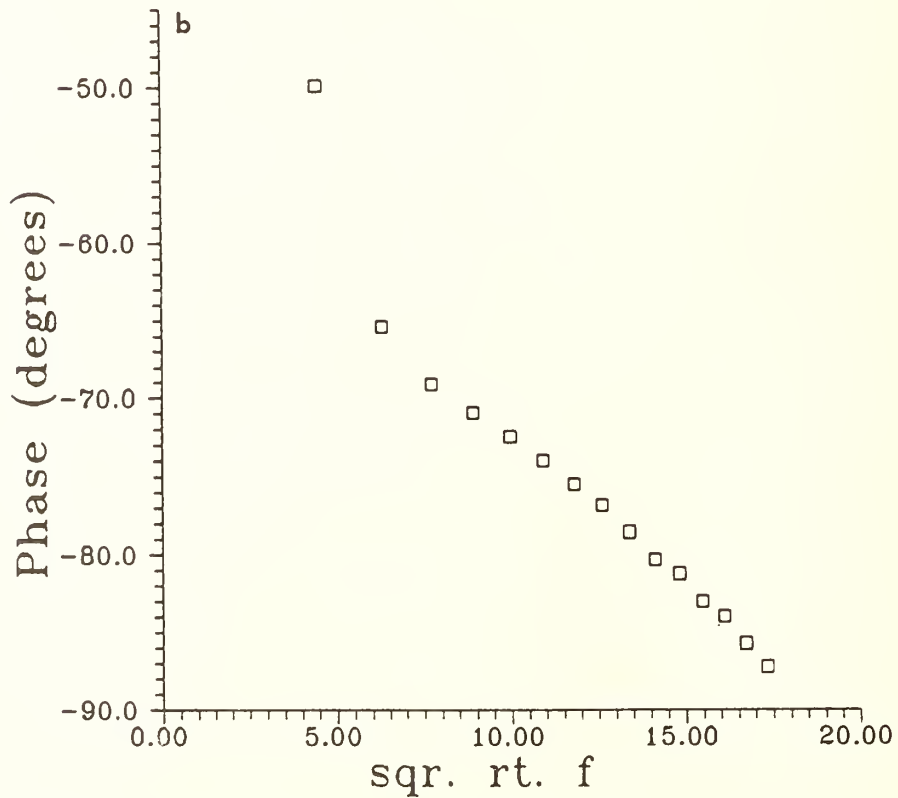
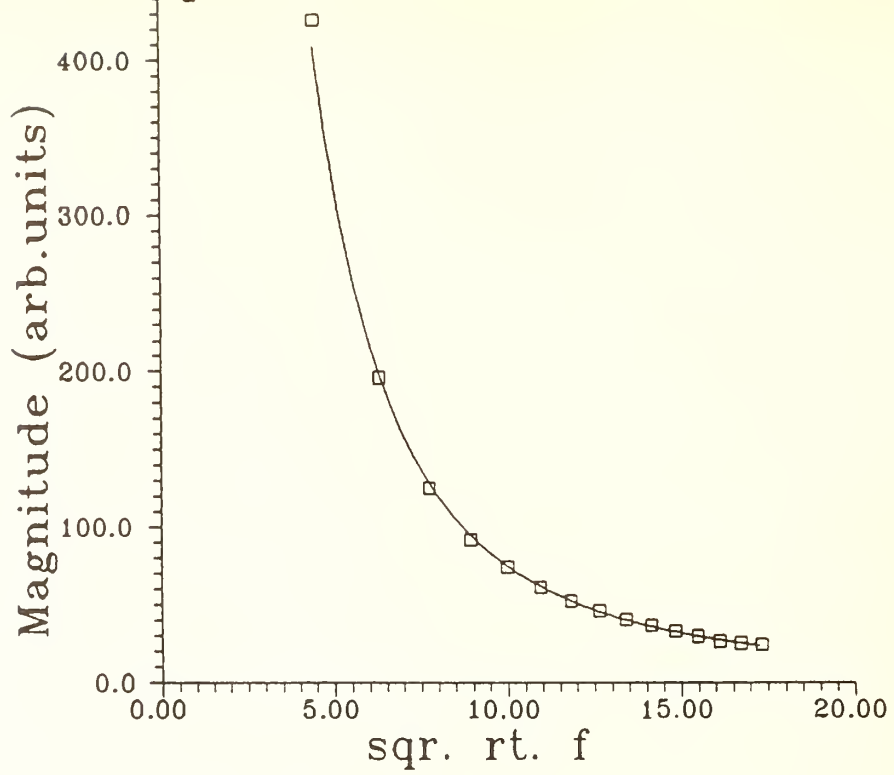
\* Work done while a visiting scientist at N.B.S.



1. Schematic diagram of a photoacoustic cell. A modulated heating beam from a CO<sub>2</sub> laser passes through the ZnSe window into the sealed chamber where it is incident upon the sample. The heated surface causes a pressure variation in the air above the sample which is detected by the microphone.

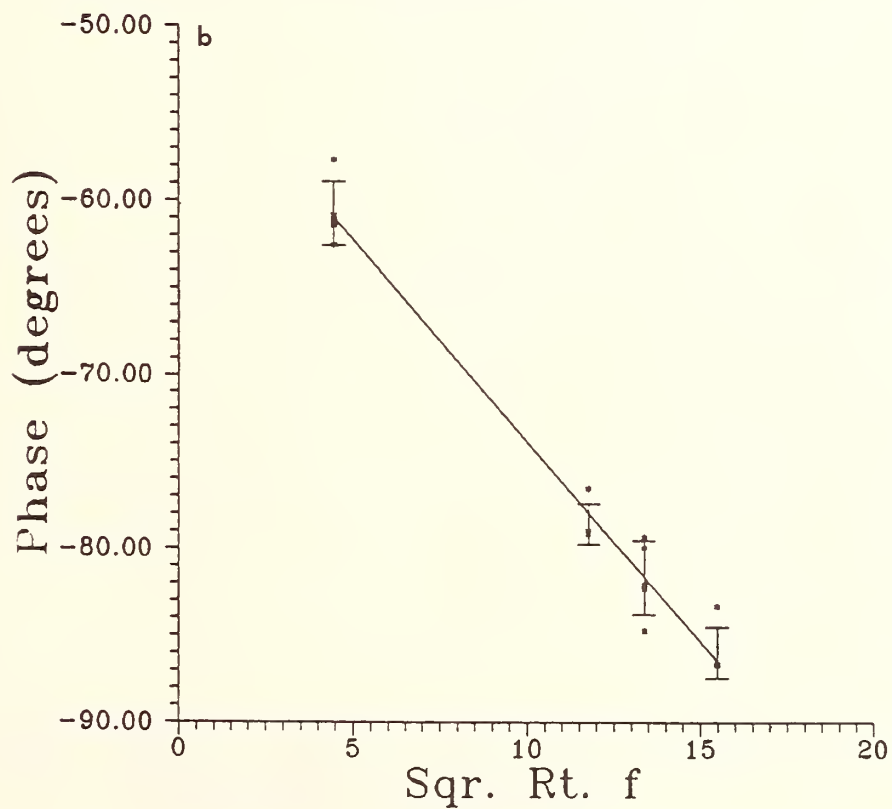
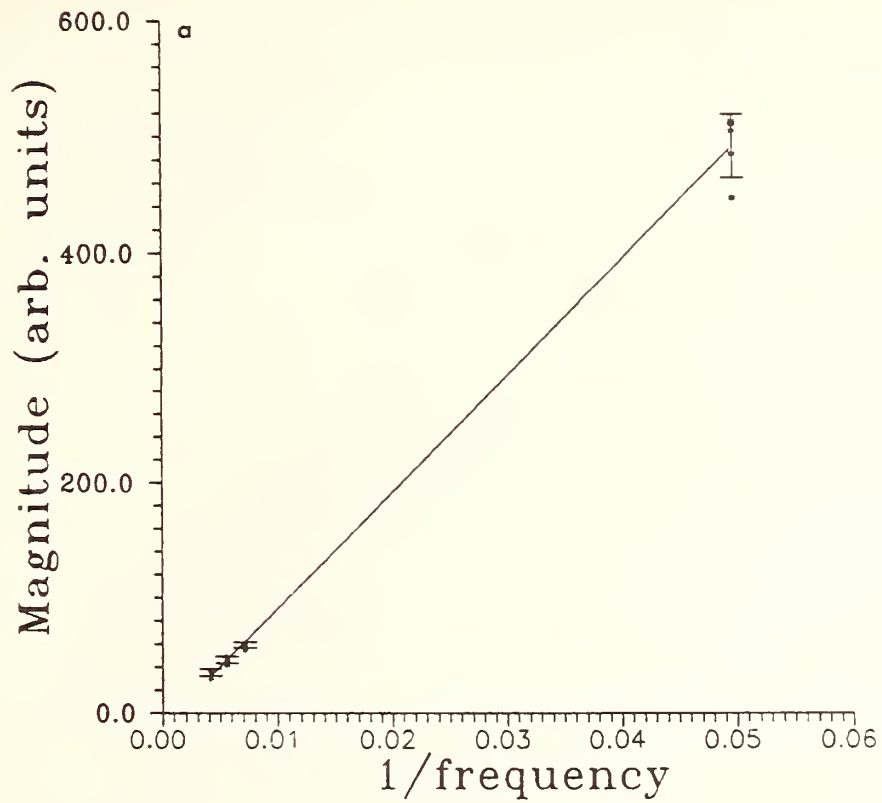


2. Schematic diagram of the mirage effect. A modulated source heats the sample surface. The surface then reheats the atmosphere, causing an index of refraction ( $n$ ) gradient above the heated sample surface. A HeNe probe beam, passing through the heated atmosphere is deflected at the same frequency as the sample is heated. The resulting deflection,  $\Phi$ , is detected by a position sensitive detector.



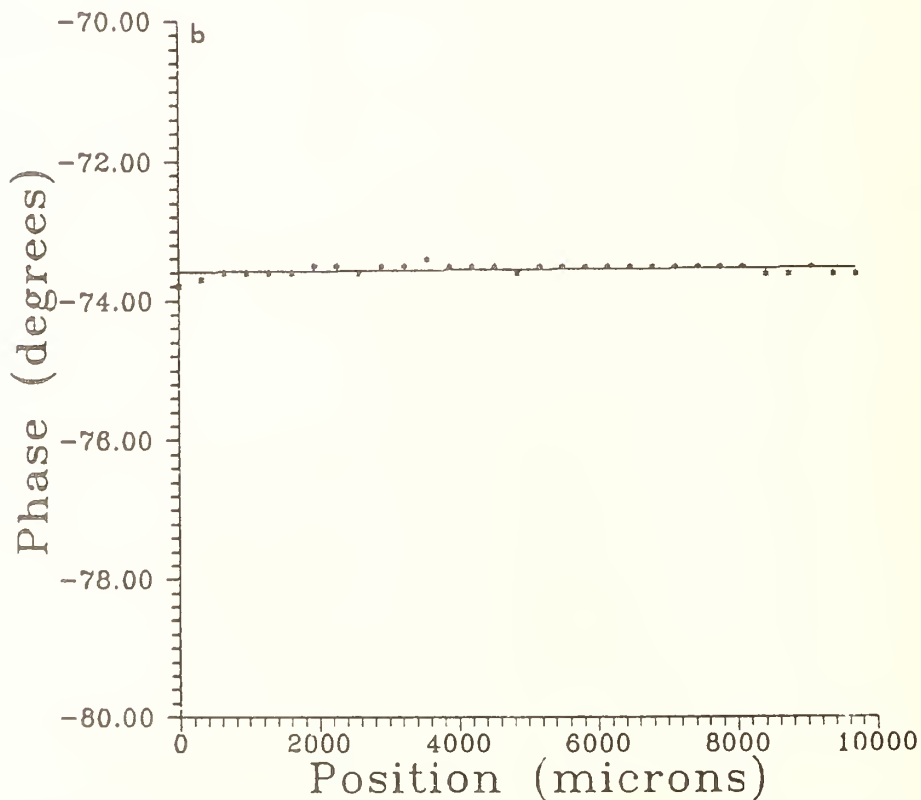
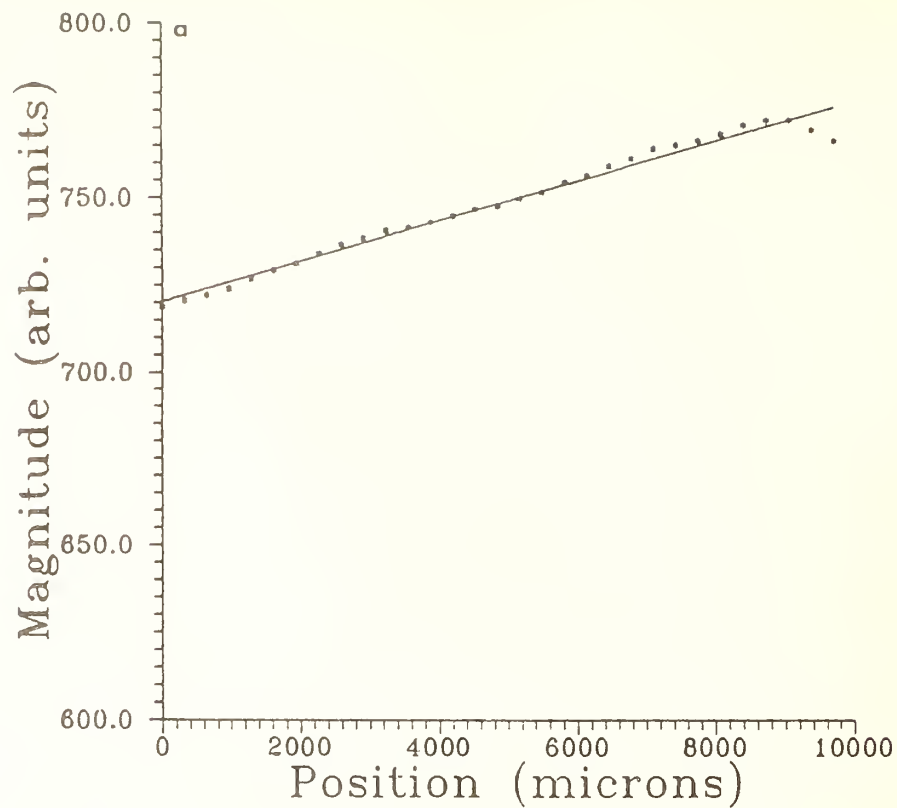
3. a) Magnitude signal of the mirage effect for a deflection of the probe beam normal to the sample surface. The sample has been ground and then polished.

b) Corresponding phase data for the same sample position and time as shown in Figure 3a.



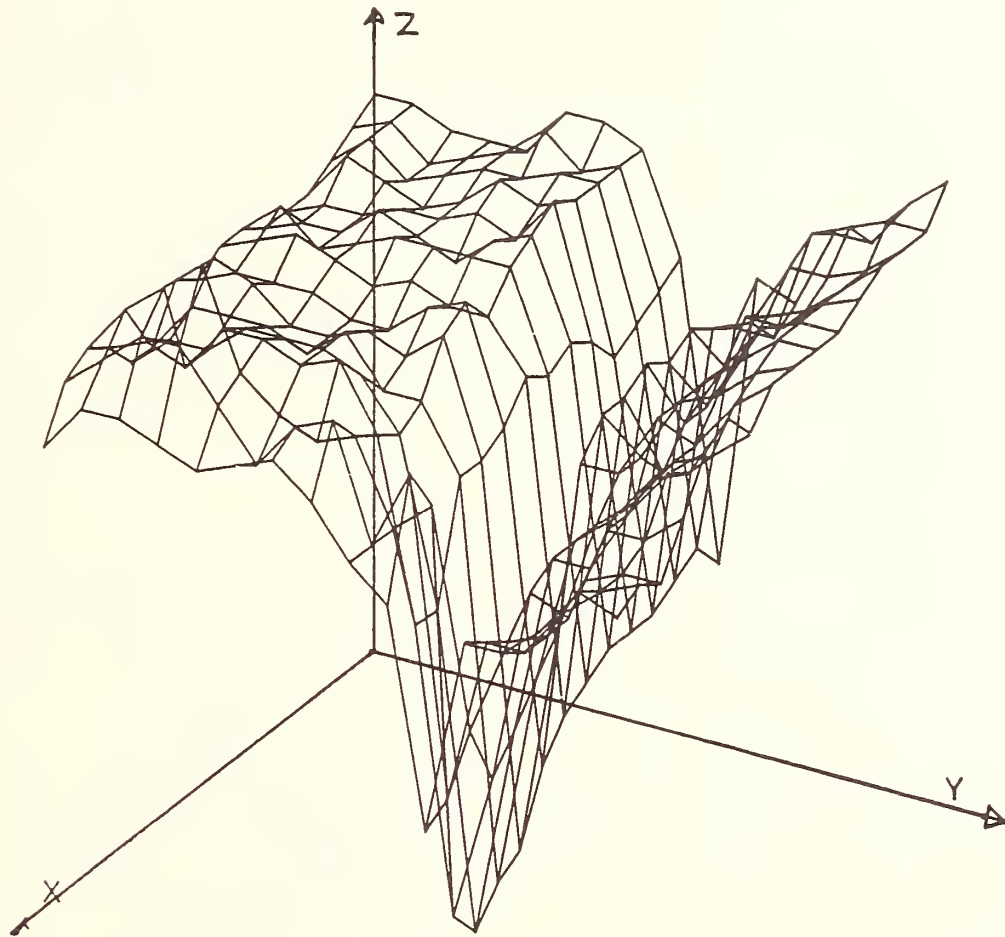
4. a) Photoacoustic magnitude data for a specimen which has been ground and polished.

b) Photoacoustic phase data for a specimen which has been ground and polished.

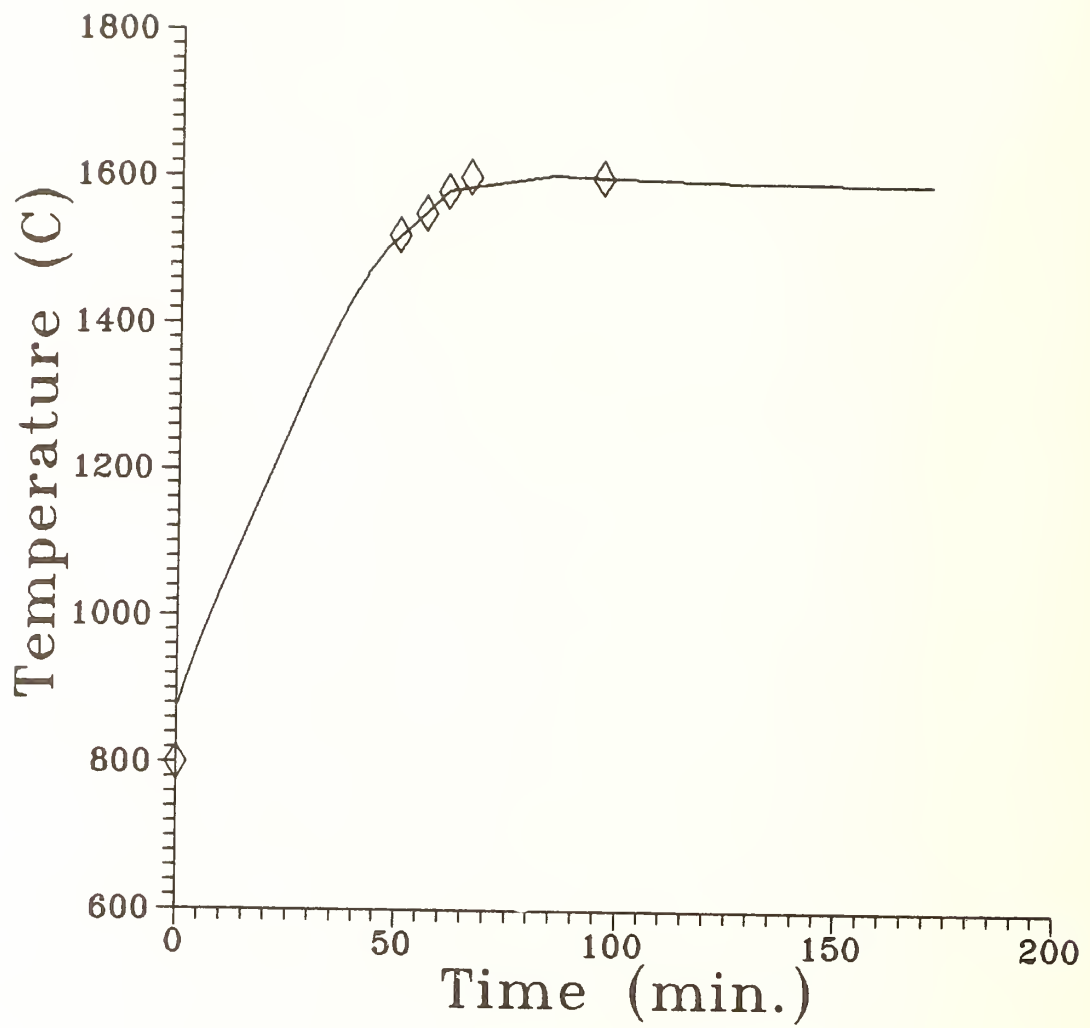


5. a) Photoacoustic magnitude scan across the surface of an as-received sample. The lack of structure indicates no detectable surface damage.

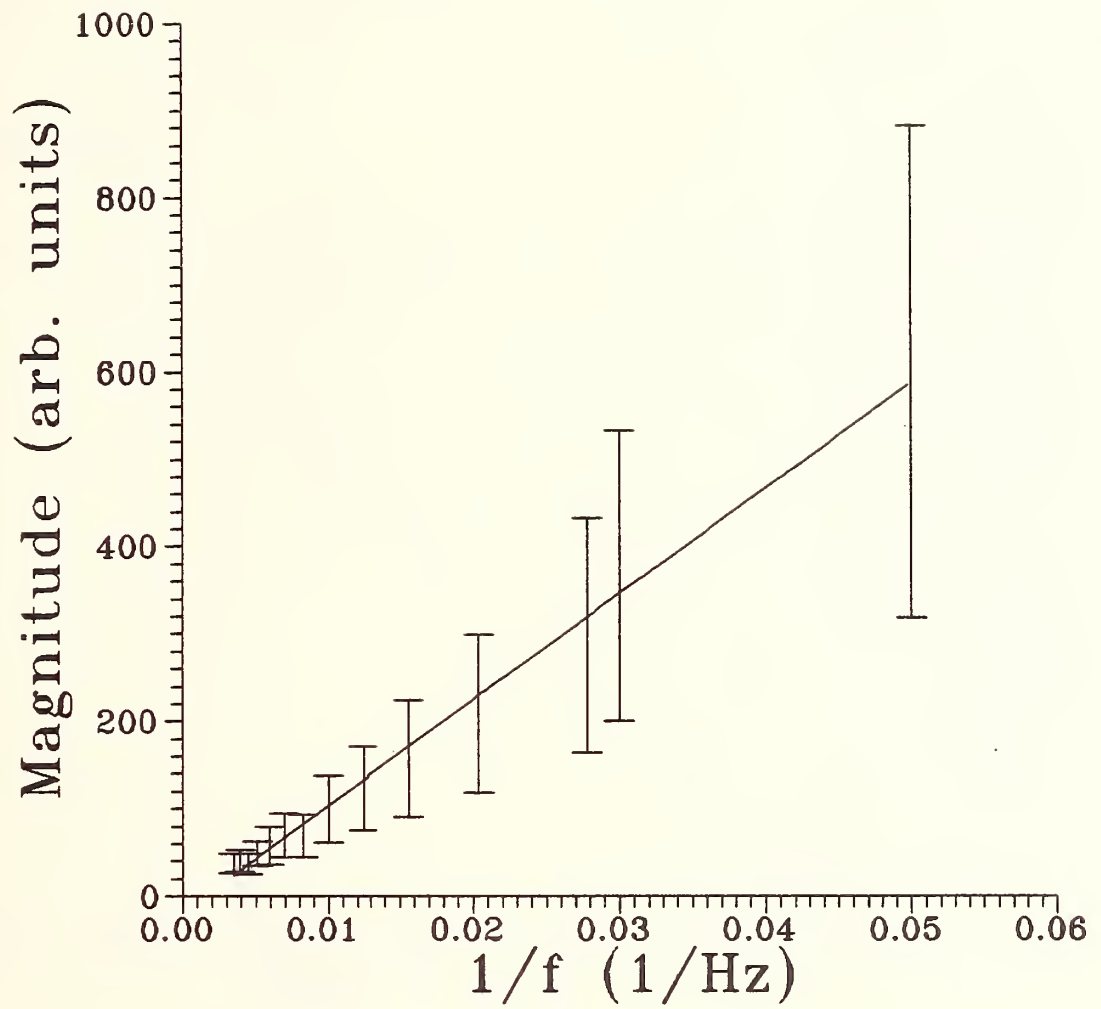
b) Photoacoustic phase scan across the same sample surface as in Figure 5a. Again, no indication of damage is observed.



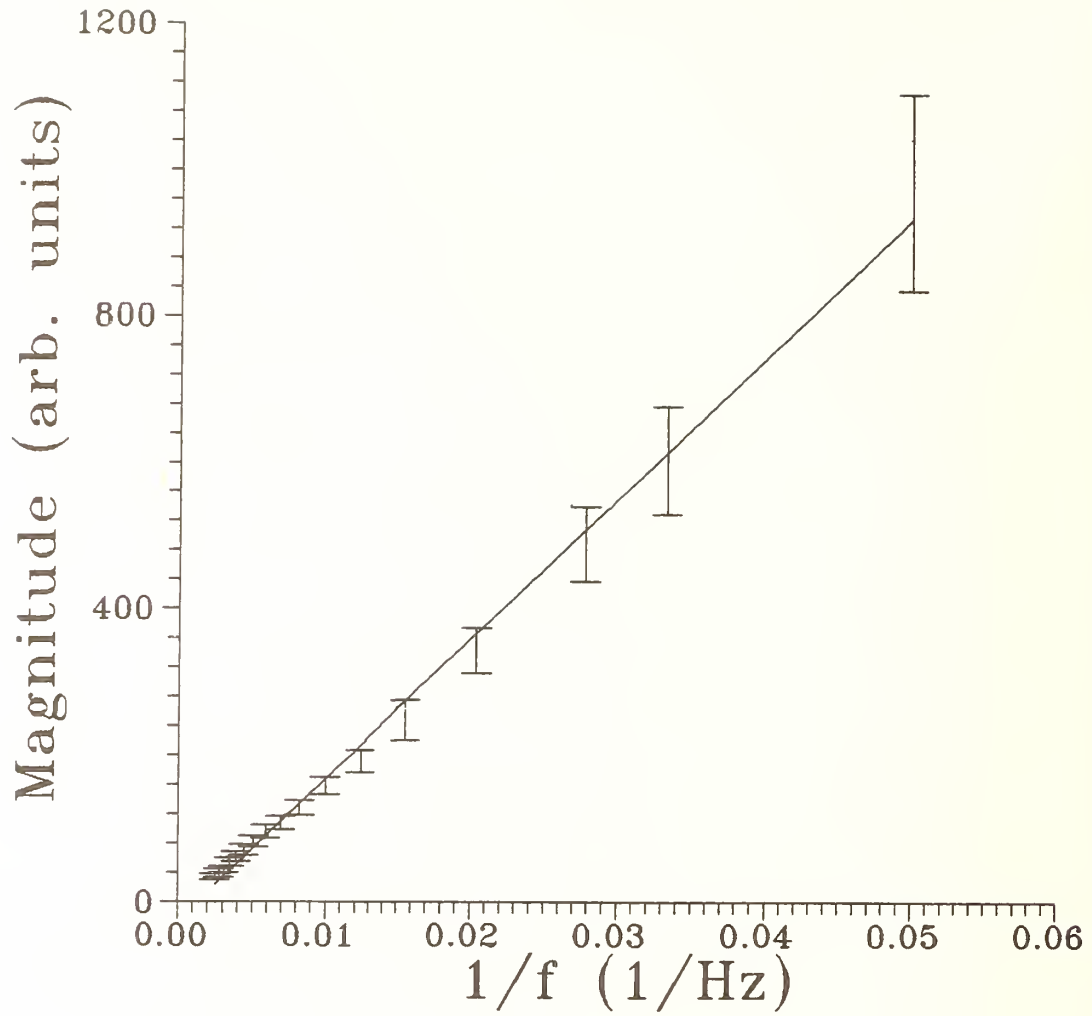
6. Photoacoustic image of sample after grinding and polishing, showing the presence of a remaining scratch.



7. Furnace temperature plotted as a function of time during the firing treatment of the alumina specimens.



8. Photoacoustic magnitude measurements of the alumina specimen with 30.8% porosity as a function of heating frequency.



9. Photoacoustic magnitude measurements of alumina specimen with 3% porosity as a function of heating frequency.

A. Hecht, E. Neumann, P. Rose

Introduction

Non-oxide ceramics are mainly used at high-temperatures or for wear-resistant parts. Typical materials are silicon-carbide (SiC) and silicon-nitride (Si<sub>3</sub>N<sub>4</sub>). Due to the brittleness of ceramics, even very tiny defects (<50 μm) may cause failure. Consequently high-frequency ultrasonic testing (UT) should be practiced for the detection of defects which are smaller than e. g. 50 μm. First attempts have been made by developing a 120 MHz-UT-equipment [1] Since the transmission-factor of the couplant/material-interface becomes very frequency dependent at such high frequencies, problems might occur to get an ultrasonic impulse passing through the interface if the surface is not polished [2]. Also the material's attenuation has to be considered: Usually, the attenuation of sintered ceramics is very low even at frequencies above 100 MHz, but can reach very high values for cast-ceramics at lower frequencies (20 MHz).

This paper presents results of 25 MHz and 50 MHz ultrasonic testing of reaction-bonded silicon-infiltrated silicon-carbide (SiSiC) containing approx. 12% free silicon, and of hot-pressed silicon-nitride (HPSN). Some of the UT results are compared with low-energy radiographic images.

Ultrasonic test equipment "ABAKUS"

All devices of "ABAKUS", which was developed as a multi-purpose UT-equipment [3-5], are displayed in Figure 1. These devices are commercially available and may be combined in various arrangements to realize the different UT-techniques, e. g. B-scan, C-scan, etc. [3].

UT of ceramic materials was carried out first by using a 25 MHz focussing transducer in immersion technique with the specimen completely under water. Figure 2 shows typical echo traces of UT in immersion technique, where a front surface echo and a backwall echo can be distinguished. To detect small defects, the amplification has to be increased. If the transducer is placed directly over a flaw, an additional echo occurs. Its amplitude can be measured by the ultrasonic analyzer's peak level detector after having gated out a distinct depth-zone of the specimen. The start point of this depth-zone is influenced by the length (duration) of the front surface echo. This length is approximately 4 mm in Figure 2, if the materials thickness is 10 mm. The latest stop point of the evaluable depth-zone is fixed directly by the beginning of the backwall echo.

An important criterion for the selection of an appropriate focussing transducer is the focal distance (distance between transducers front surface and focal point on the acoustical axis). As the ratio between the sound velocities of ceramics and couplant water is approx. seven, the focal distance in ceramics is approx. a seventh of its value in water. Consequently, transducers with a long focal distance should be selected for the inspection of thicker parts, if available.

All measurements presented in this paper are UT C-scans, where the specimen is scanned and the amplitude  $A$  measured within a fixed depth-zone. Amplitude resolution is 8 bit. The data are then displayed as  $A(x,y)$ , where  $x,y$  are spatial coordinates. Figure 3 shows the experimental set-up for a C-scan recording by "ABAKUS". An additional characteristic of this set-up is a spectrum analyzer used as a bandpass filter with variable bandwidth and center-frequency. This is a measure to suppress the electrical noise and consequently increase the flaw detectability. The bandpass-filtered signals are then recorded by a transient-recorder and the maximum amplitude evaluated by fast software.

computer-aided equipment is a useful tool for detecting, monitoring and evaluating defects. Digital image analysis should be an additional means to compare results of ultrasonic and radiographic testing. Detected defects can be evaluated additionally by use of focussing transducers of higher frequency and taking microscopic C-scans for flaw sizing as well as regarding carefully the A-scans at the defect positions. This might be a suitable method for flaw-type characterization.

#### Acknowledgement

This work was carried out at the German Federal Institute for Materials Testing (Bundesanstalt für Materialprüfung (BAM)), Berlin. The destructive preparation of the HPSN-specimen was carried out at Elektroschmelzwerk Kempten (ESK). The authors thank all persons who contributed to this report.

#### Authors

A. Hecht is with BASF Aktiengesellschaft, ZEW/BFZ-L443, 6700 Ludwigshafen, German Federal Republic. E. Neumann and P. Rose are with Bundesanstalt für Materialprüfung (BAM), Fachgruppe 6.2, Unter den Eichen 87, 1000 Berlin 45, German Federal Republic.

the ultrasonic transducers sound field. In some cases the coincidence is good, in others not so good. This is most likely caused by the different depth-sensitivity of the focussing ultrasonic transducer.

Further examinations were made by taking microscopic ultrasonic C-scans of interesting regions with a 50 MHz focussing transducer. Figure 11 shows the ultrasonic image of an inclusion 1 mm below the surface that was detectable by both UT and RT. As the defect appeared as a white spot on the radiographic image, one could be certain that it was an inclusion. Figure 12 shows the ultrasonic A-scan at the defect position of maximum amplitude. No single echo occurs, but a long sequence of various echoes caused by circumferential and other types of waves. This is in accordance with [9], where the echo traces resulting from spherical inclusions could be predicted.

Figure 13 shows the A-scan of a flaw 0.5 mm below the surface, that was detectable only by UT. Only one distinct flaw echo occurs. Consequently this could be no spherical shaped defect. The ultrasonic footprint-shaped image of this flaw is shown on the left side of Figure 14. Its planar size was estimated with  $0.8 \times 0.35$  mm by a 6 dB-drop method (this method can be applied because of the very small focussing diameter). A micrograph of the defect (see Figure 14, right) was obtained after grinding 0.5 mm of the specimen's thickness. The defect was a flat shaped region of porosity with the dimensions  $0.75 \times 0.36 \times 0.1$  mm and was not detectable by RT because of the very small size in depth direction.

### Conclusion

As most of the defects in the inspected specimens were much bigger than 50  $\mu\text{m}$ , satisfactory results could be obtained even at a test-frequency as low as 25 MHz. However further basic work is necessary to cope with all the problems arising. A

area on the right side is caused by a Si-vein, which is only a few  $\mu\text{m}$  thick but of large extension. All these defects are displayed in Figure 7, where "A" is an optical image and "B" and "C" are SEM-images. SiC appears dark and the free silicon white.

Figure 8 shows a photograph of that cross-section of the SiSiC-plate where the Si-vein is located (see top view, Figures 4 - 6). In this side-view the Si-vein appears as a thin white line. In addition two areas of different density are visible, caused by different Si-concentrations in the SiSiC microstructure. Such areas can be detected non-destructively by computer X-ray tomography [8]. Figure 8 points out, that only those parts of the Si-vein are detectable by UT in normal incidence, which are located perpendicular to the incident direction. Additional UT in oblique incidence would be necessary to detect the complete Si-vein area in the examined specimen.

#### Ultrasonic testing of HPSN

The inspected specimen was a 9 mm thick crescent-shaped plate, the length of the secant line is 110 mm. Again the specimen was inspected twice by taking one C-scan from each side. Figure 9 shows the superposition of these two C-scans as well as a photograph taken from a radiographic image (30 kV tube-voltage). Only few white spots caused by absorptive inclusions are visible, but the original radiographic image displays many more flaw indications.

In order to compare the ultrasonic and radiographic results only the small marked areas in Figure 9 are considered. These areas are shown magnified in Figure 10. The flaw images from the UT C-scan above are also projected as lines into the radiographic image below. UT indications are of a bigger size than the indications from radiographic testing (RT) due to

All the measured C-scans  $A(x,y)$  are stored in the computer, where mathematical transformations or other signal analyses may be carried out after the measurements have been taken [5]. The data can also be transferred into a digital image-processing system, which is normally used for X-ray film evaluation [6] in the BAM. This image-processing system allows to combine, transpose, or superimpose different UT C-scans, and even superimpose UT C-scans with radiographic images. It also offers different measures of image enhancement. All figures containing C-scans in the next chapter are photographs from the image-processing system screen.

### Ultrasonic testing of SiSiC

Properties of SiSiC are characterized in [7]. The inspected specimen was a 10 mm thick plate containing several natural defects. The C-scan in Figure 4 displays all the flaw indications (echoes, see Figure 2) in a depth zone of 4 - 10 mm. (This limited range results from the "dead zone" of the front surface echo in Figure 2). The echo amplitude  $A$  is represented by 255 grey-scale values in accordance with the 8 bit resolution of the used transient-recorder.

If the specimen is turned around (and the coordinate system too), the depth zone of 0 - 6 mm can also be inspected (see Figure 5). Both Figures 4 and 5 look very similar, as most of the flaws are located in the overlapping depth zone of 4 - 6 mm. Figure 6 is the superposition of Figures 4 and 5, and displays all detected flaws in the complete volume of the specimen.

Destructive follow-ups showed, that all the spherical shaped indications are caused by voids or local Si-enrichments, which cannot be distinguished yet. The straight line in the middle of Figure 6 is the ultrasonic image of a "worm-hole", accompanied by Si-enrichments. The larger

## Abstract

Plates of different ceramic materials have been inspected with a computer aided ultrasonic test equipment at frequencies of 25 and 50 MHz. The measured ultrasonic C-scans were compared with radiographic images by transferring all data into a digital image processing system. The detectability of different types of defects is discussed. Flaw sizes can be estimated by taking microscopic C-scans with focussing high-frequency transducers, and flaw type characterization can be carried out by recording particular features of the ultrasonic A-scan.

## References

- [1] Goebbels, K., Reiter, H., Hirsekorn, S., Arnold, W.: "Non-Destructive Testing of High-Temperature and High-Strength Ceramics". Proceedings of the 12<sup>th</sup> Int. Conference in Science of Ceramics, Saint-Vincent, Italy, June 27 - 30, 1983, pp. 483-494
- [2] Generazio, E. R.: "The Role of the Reflection Coefficient in Precision Measurement of Ultrasonic Attenuation". Materials Evaluation 43 (1985) 8, pp. 995-1004
- [3] Hecht, A., Thiel, R., Voß, U.: "A Computer Controlled Equipment for Different Ultrasonic Measurement Techniques". Proceedings of the 3<sup>rd</sup> European Conference on NDT, Florence, October 15 - 18, 1984, pp. 145-155
- [4] Neumann, E., Hecht, A., Schnitger, D., Voß, U., Gieschler, W.: "Computer Aided Ultrasonic Testing of Fibre Reinforced Plastics". Proceedings of the 3<sup>rd</sup> European Conference on NDT, Florence, October 15-18, 1984, pp. 35-47
- [5] Güttner, F., Limpert, R., Steinhoff, U.: "Ultraschallprüfung von Hochleistungsverbundwerkstoffen". Zeitschrift für Werkstofftechnik 17 (1986)4, S. 135-147
- [6] Heidt, H., Rose, P., Raabe, P., Daum, W.: "Digital Image Processing for Radiography in Nuclear Power Plants". Proceedings of the 7<sup>th</sup> Int. Conference on NDE in the Nuclear Industry, Grenoble (France), 1985, pp. 317-319
- [7] Willmann, G., Heider, W.: "Siliziumcarbid (SiSiC), ein neuer Werkstoff für den Apparatebau". Zeitschrift für Werkstofftechnik 14 (1983), S. 135-140

- [8] Goebbels, J., Heidt, H., Kettschau, A., Reimers, P.:  
"Computer X-ray Tomography of Ceramic Materials".  
Proceedings of the 2<sup>nd</sup> Int. Symposium on Ceramic Mate-  
rials and Components for Engines, Lübeck, April 14-17,  
1986
- [9] Sachse, W.: "The Scattering of Elastic Pulses and the  
Nondestructive Evaluation of Materials".  
Materials Evaluation 35 (1977) 10, pp. 83-106

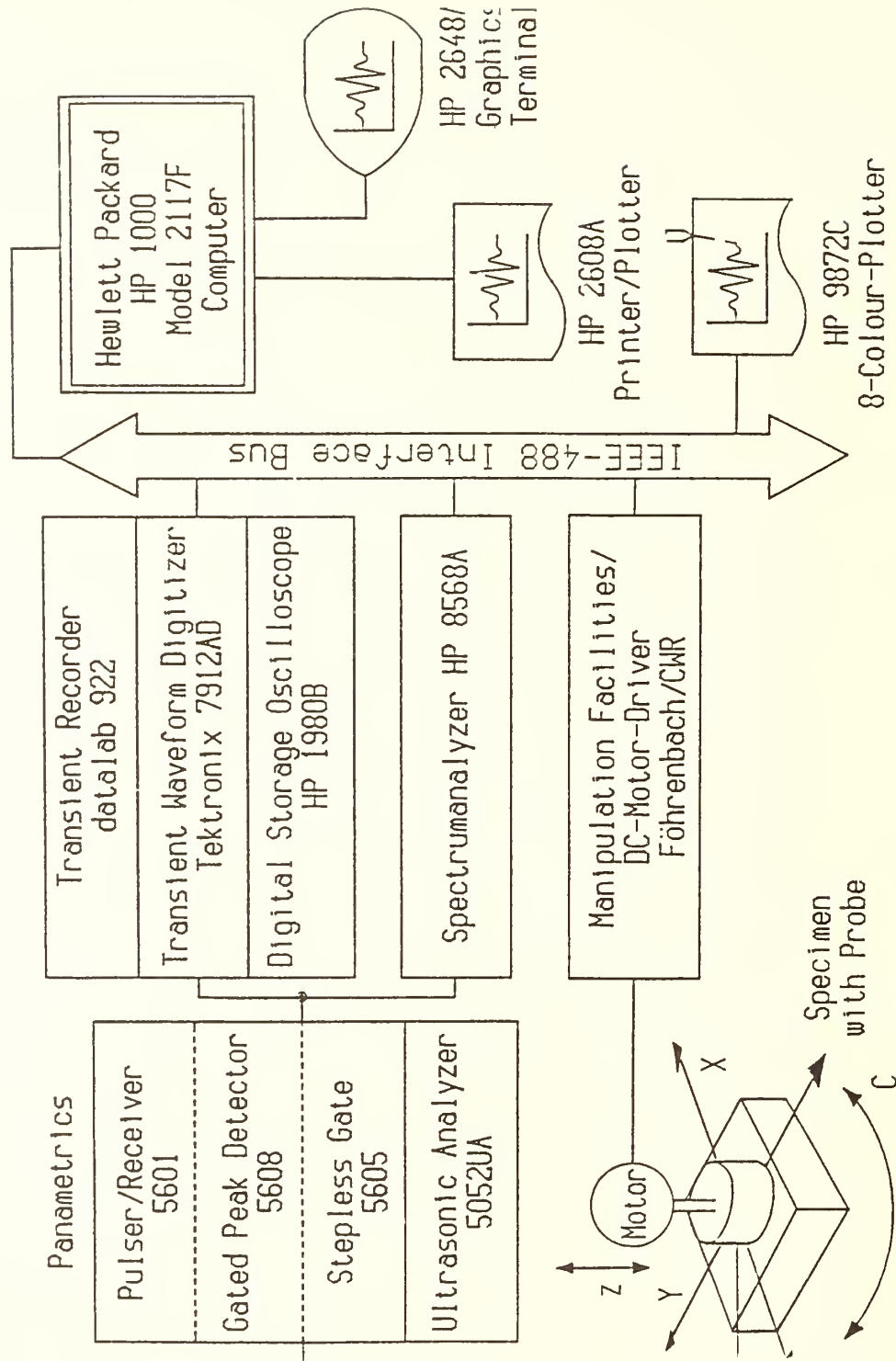


Fig. 1: Block diagram of the used multi-purpose ultrasonic testing equipment "ABAKUS"

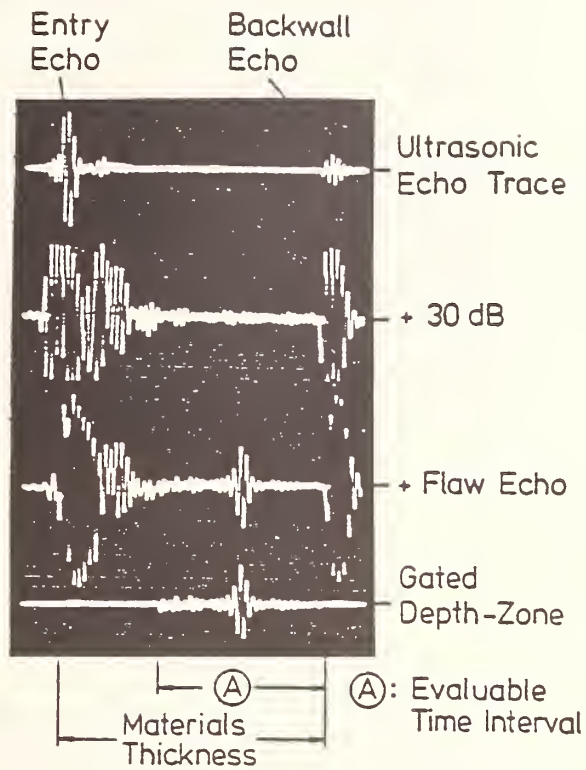


Fig. 2: Ultrasonic testing of ceramic plates; typical echo traces (A-scan)

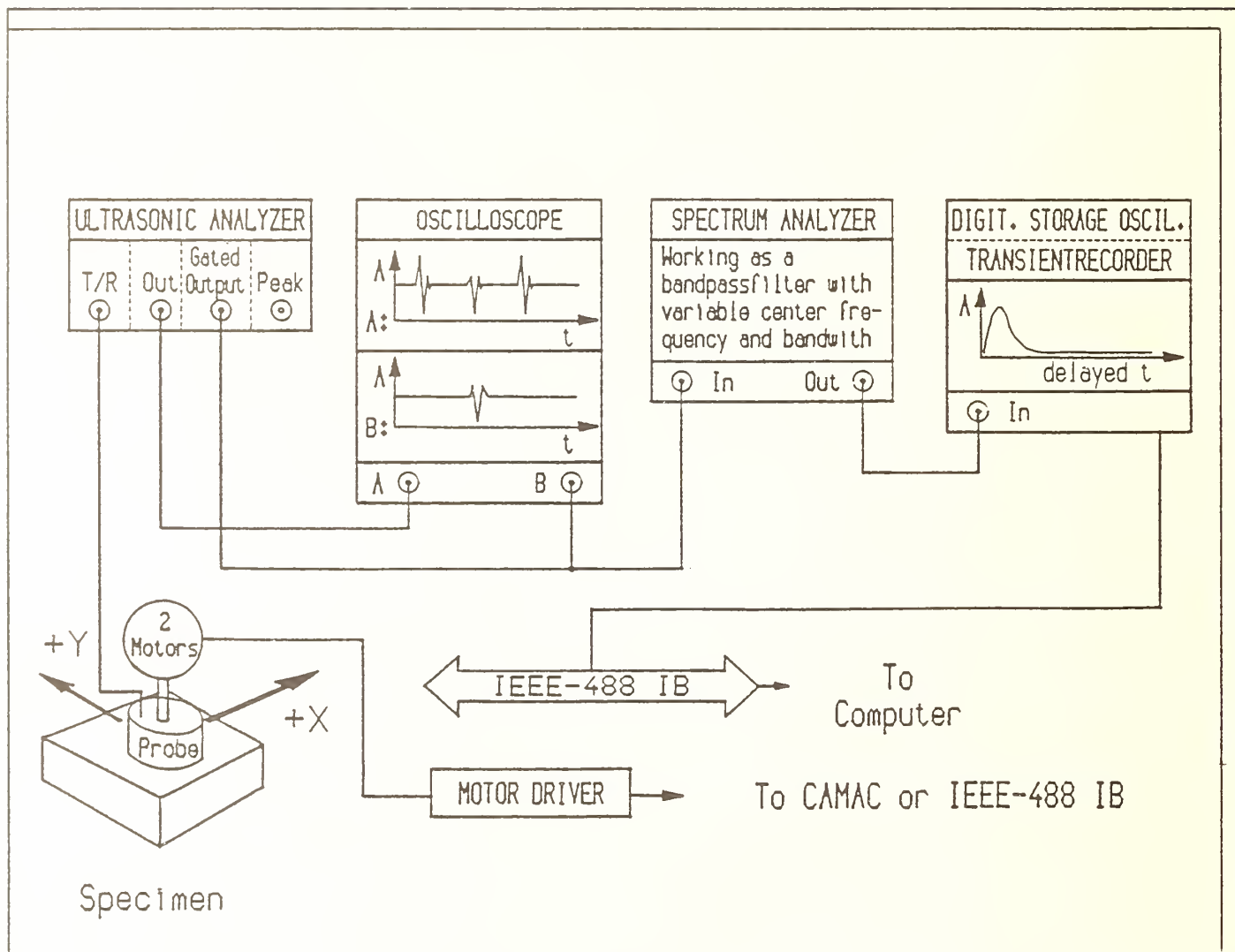


Fig. 3: Experimental set-up for the recording of C-scans by "ABAKUS"

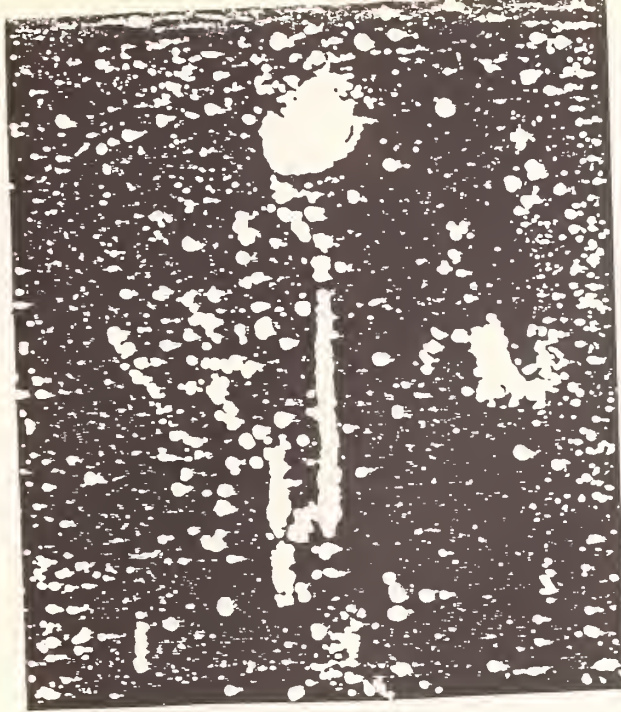


Fig. 4: Ultrasonic C-scan of SiSiC-plate (100 x 100 x 100 mm) with 25 MHz focussing transducer; depth zone 4 - 10 mm, resolution 0.25 mm

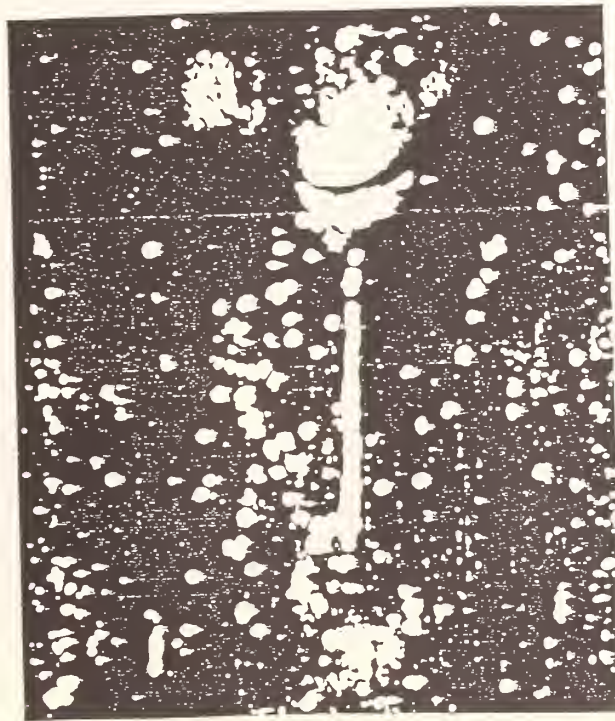


Fig. 5: Ultrasonic C-scan of SiSiC-plate (100 x 100 x 100 mm) with 25 MHz focussing transducer; depth zone 0 - 6 mm, resolution 0.5 mm; specimen turned around in immersion tank, data  $A(x,y)$  transposed

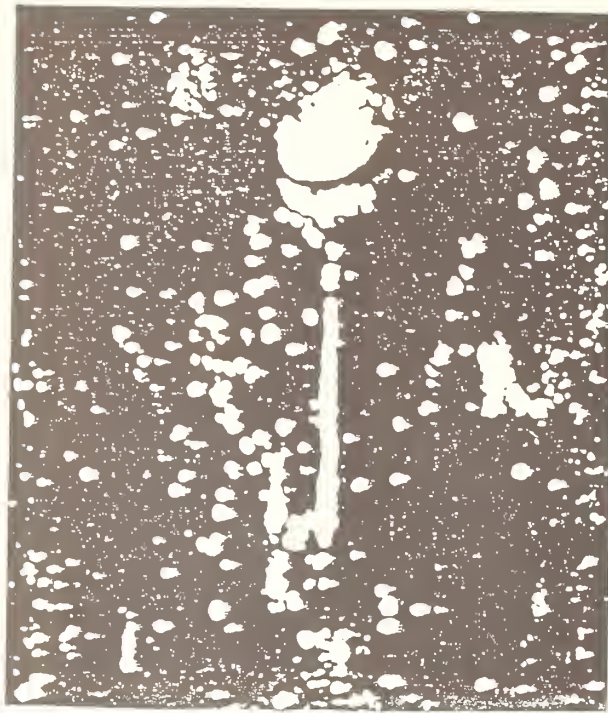


Fig. 6: Superposition of both C-scans of Figures 4 and 5;  
resultant depth zone 0 - 10 mm

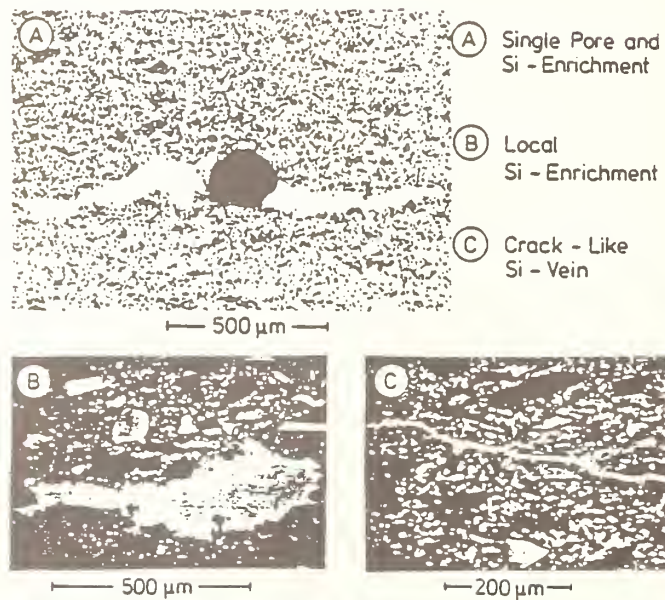


Fig. 7: Different types of flaws in SiSiC detectable with  
25 MHz focussing transducer

ULTRASONIC TESTING A - SCANS

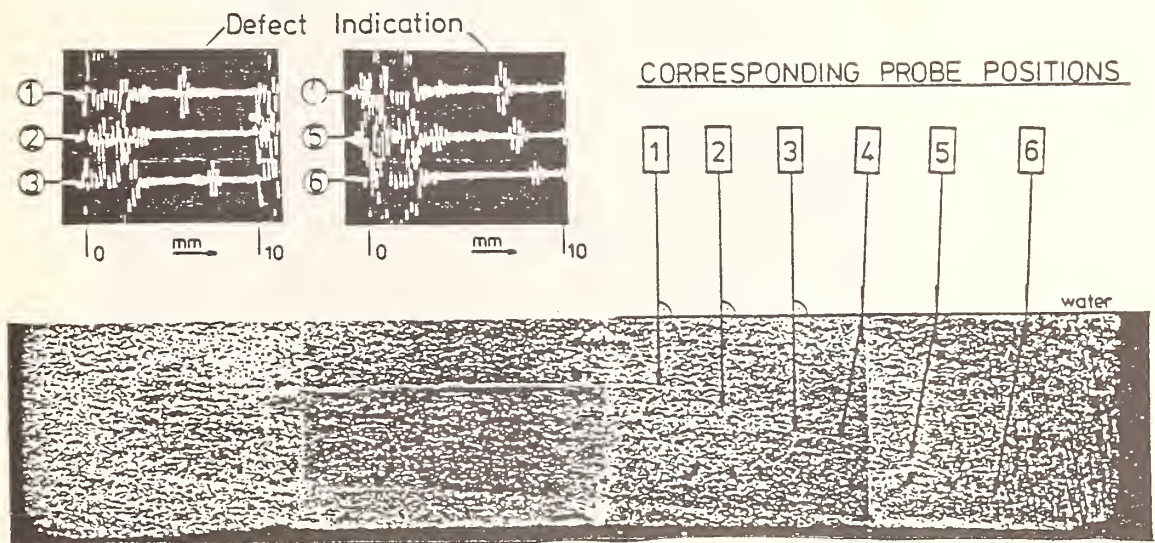


Fig. 8: Detection of a Si-vein in SiSiC by ultrasonic testing with 25 MHz focussing transducer

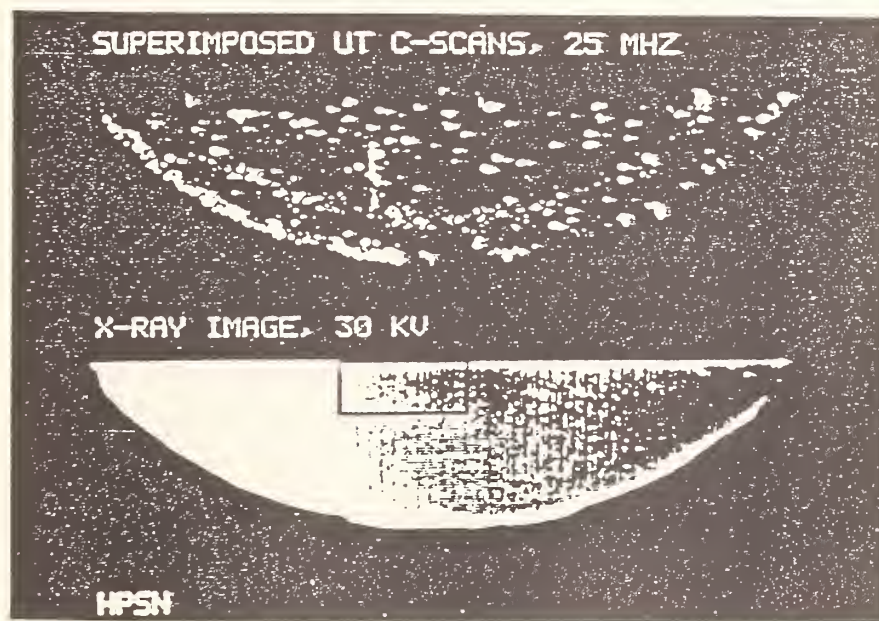


Fig. 9: Comparison of different NDT techniques at HPSN-specimen  
above: superimposed C-scans  
below: radiographic image, 30 kV  
note: Copying of radiographic images leads to much worse image quality

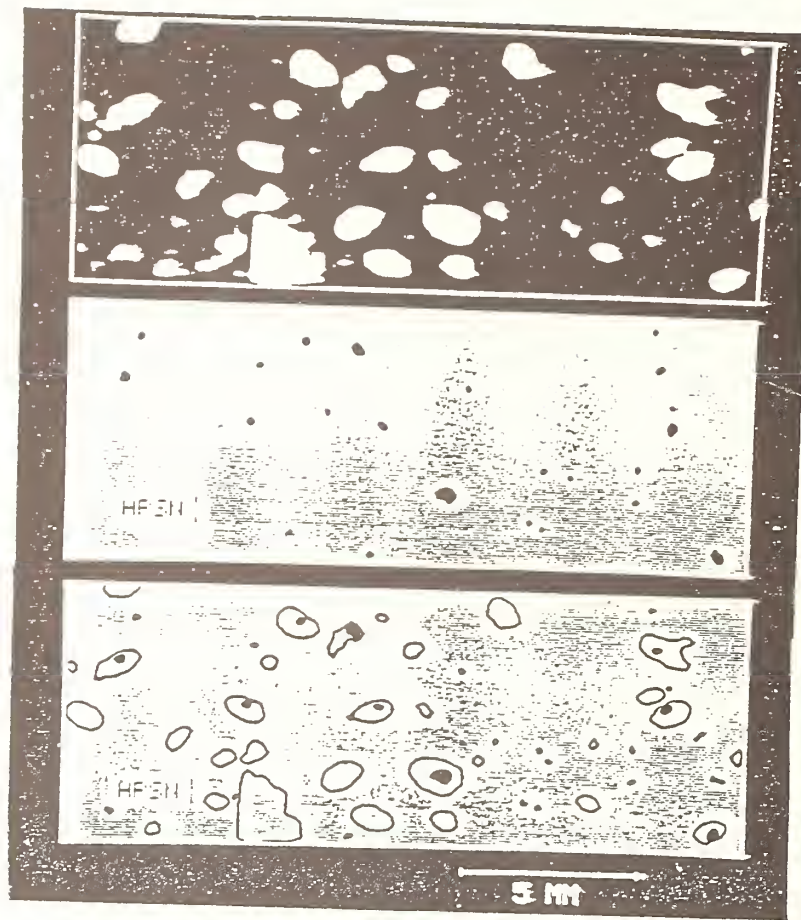


Fig. 10: Section of interest (taken from Figure 9 )  
above: ultrasonic C-scan  
middle: radiographic image after image-processing  
(detected inclusions as dark spots)  
below: radiographic indications encircled by larger  
ultrasonic indications from C-scan above

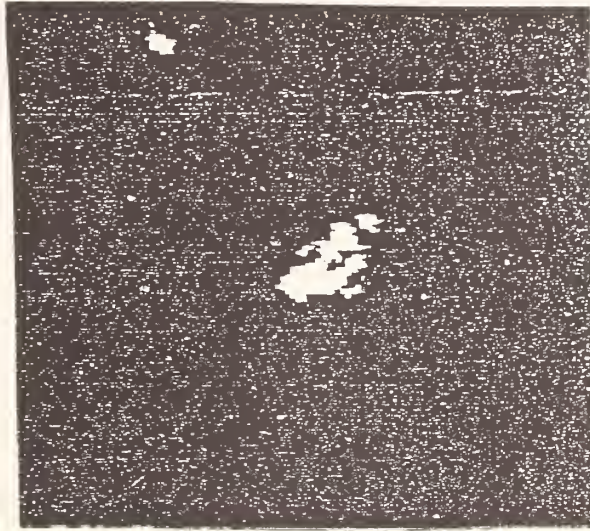


Fig. 11: Microscopic ultrasonic C-scan (2.5 x 2.5 mm) of defect detectable by UT and RT; 50 MHz focussing transducer, resolution 10  $\mu\text{m}$

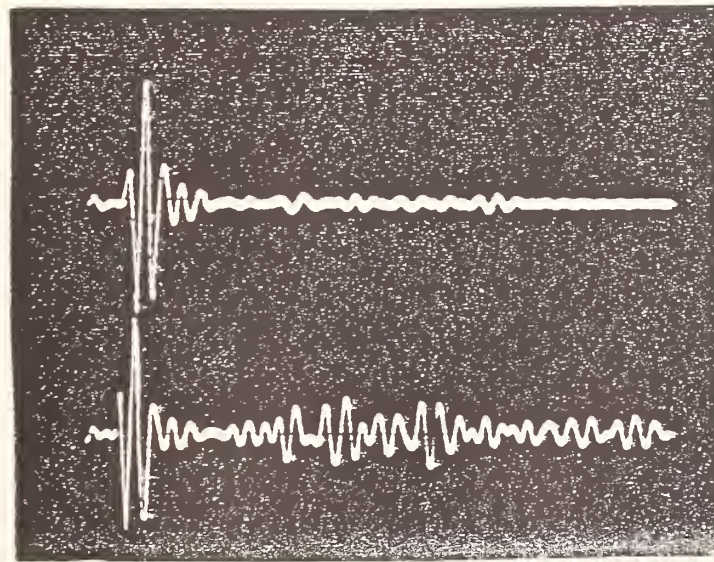


Fig. 12: Echo trace (1  $\mu\text{sec}$  full vertical scale) of larger indication of Figure 11  
above: only front surface echo  
below: additional sequence of flaw echoes, caused by circumferential waves (see [9])

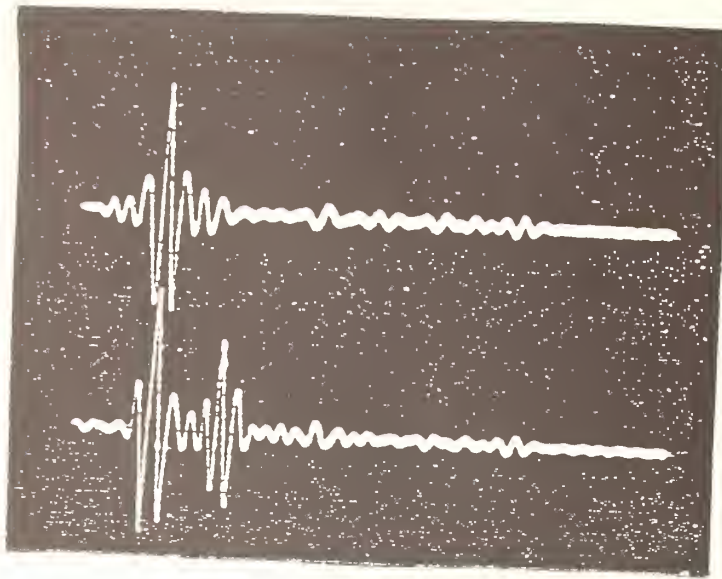


Fig. 13: Echo trace (1  $\mu$ sec full vertical scale) of defect detectable only by UT  
 above: only front surface echo  
 below: additional single flaw echo

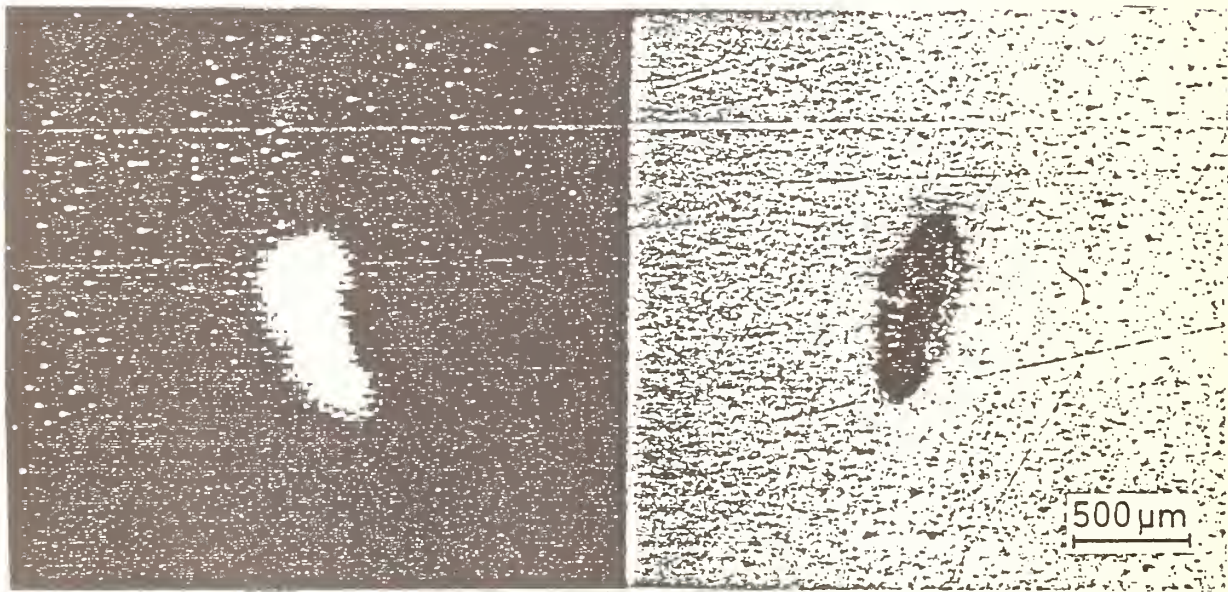


Fig. 14: Flat inclusion detectable only by UT  
 left: Microscopic ultrasonic C-scan (2.5 x 2.5 mm)  
 with 50 MHz focussing transducer; resolution 10  $\mu$ m  
 right: unetched micrograph (mirror image) after  
 grinding and polishing

Introduction

Computed X-ray tomography (CT) offers the great advantage to produce maps of the local X-ray absorption inside an object. In comparison to that conventional radiography gives only a projection image which means that the interpretation of such images is often complicated or impossible especially at complex object geometries. Together with the good density resolution this was the reason for the great success of CT in medicine since about 15 years. In this paper an insight will be given into the possibilities of CT to localize and characterize defects in ceramic components.

Development of BAM-Computertomograph

In general the medical tomographs are not suited to NDT applications. Therefore at BAM a group started with the development of a tomograph about 1978. After preliminary investigations with an experimental scanner, a very flexible machine was developed and installed in 1984.

Constructed for a wide range of industrial objects the tomograph cannot represent the most favourable solution for NDT of ceramics but the images made by this system can give the information needed to construct a CT-scanner for this special application.

The BAM-scanner has the following specifications:

- Mechanical system: 3 axis scanner table
  - Reproducibility and accuracy of the linear axis: 30  $\mu$ m
  - of the angle position: 0,01<sup>o</sup>
  - Maximum diameter of object: 1 m
  - Maximum weight: 1000 kg
  
- Detector system: 32 detectors (Photomultipliers with plastic scintillators)
  - Collimator: 1.2 mm width, 2 to 8 mm height
  - Single collimator: 0.2 mm width, 2 mm height

- Radiation sources: X-ray, 420 kV  
60-Co, 1.33 MeV (12 TBq)

### Experimentals

The quality of a tomograph and of the images taken with it is mainly determined by three parameters:

- spatial resolution
- density or contrast resolution
- artefacts or nonlinearities which depend on object geometry. A treatment of this group of effects is out of the scope of this paper.

The first two images are examples for the good density resolution of the CT-method.

Fig. 1 shows the hot pressed Silicon Nitride plate described in the paper of Hecht et al. The density resolution is 1.2 %. At the outer range of the plate a region with a lower density (the width is about 3.5 mm) is clearly detected.

Fig. 2 shows four tomograms of a Si impregnated Silicon plate. Two regions with different density can be distinguished. The histogram exhibits two peaks which correspond to a density difference of 2.7 %.

Whereas density variations can be analysed quantitatively such an analysis is difficult for defects with dimensions smaller than the spatial resolution. It depends on the focal spot size, the size of collimators and the distance between source, object table and detector system, or simply the magnification of the system.

Fig. 3 and 4 show the possibility of this method to detect defects even smaller than the spatial resolution and to distinguish between voids and inclusions.

Fig. 3 shows a gas turbine rotor with an inclusion in the rotor blade at  $90^{\circ}$ . The density of this inclusion is for minimum 19 % higher than the average density.

In the last figure are shown two adjacent tomograms of a Sintered Silicon Carbide rotor each with two different grey level representations. The upper images show the  $\pm 20\%$  range the lower the  $\pm 5\%$  range of the average density. The lower part of the two tomograms shows one respectively two voids (about  $150\ \mu\text{m}$  diameter) in the wheel nave.

### Conclusions

Computed X-ray tomography is a useful tool to detect density variations and defects like voids and inclusions in ceramic components. For a quantitative description of such defects a well suited tomograph with improved spatial resolution is needed.

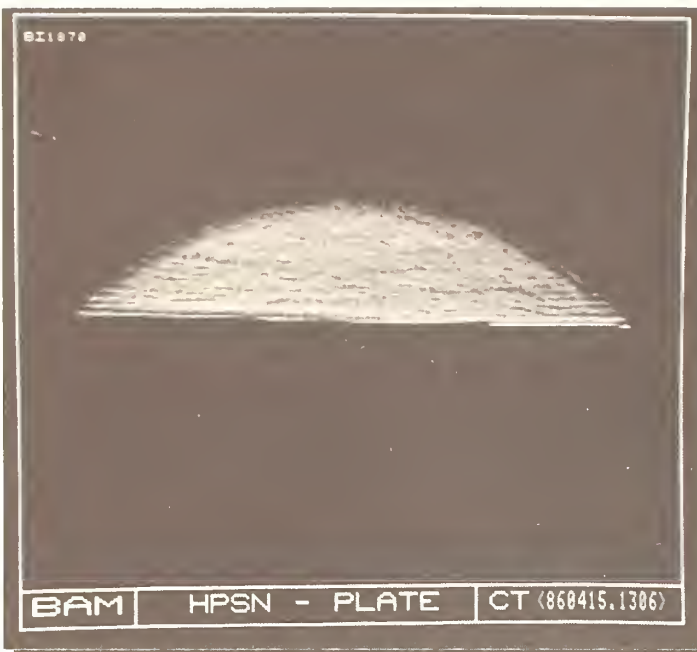


Fig. 1: Tomogram of a hot pressed Silicon Nitride plate

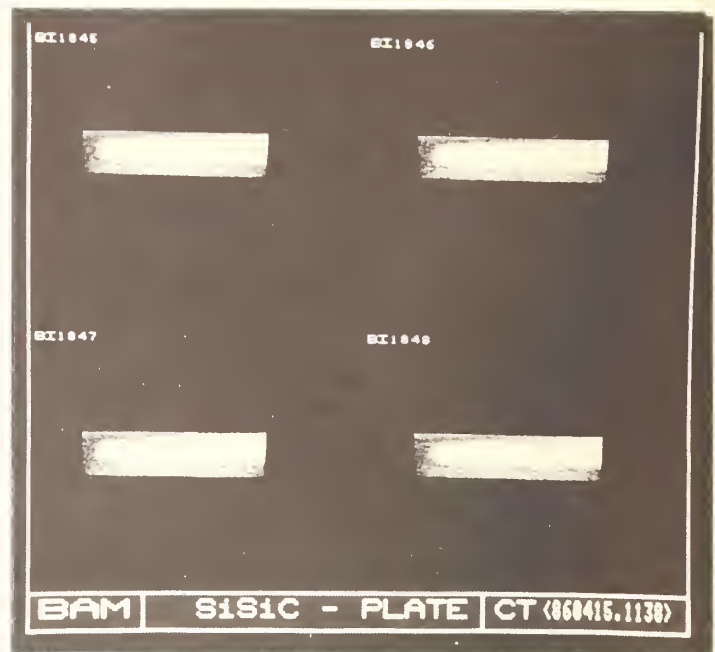


Fig. 2: Four tomograms of a Si impregnated Silicon plate

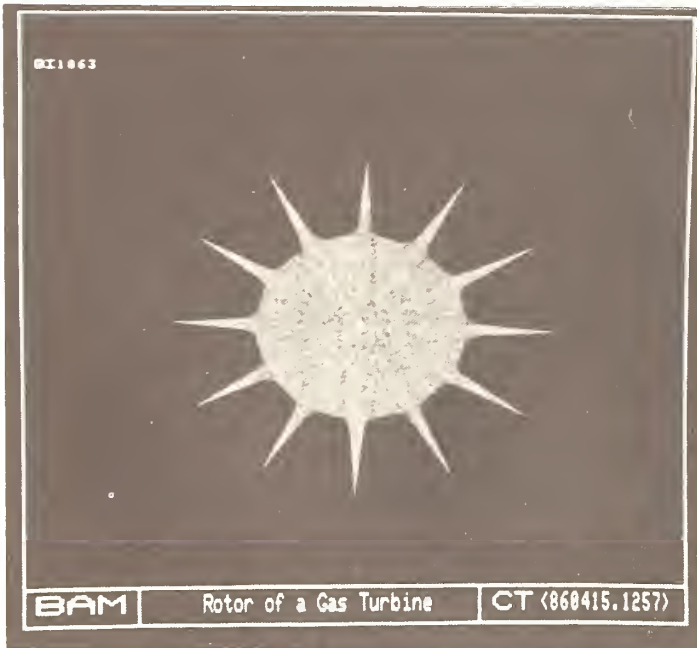


Fig. 3: Tomogram of a gas turbine rotor - Inclusion in the rotor blade at 90°

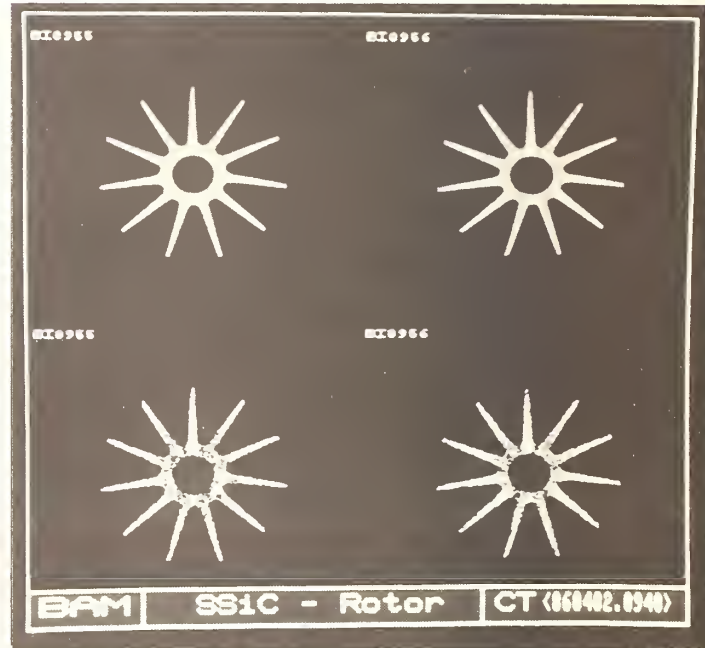


Fig. 4: Two tomograms of a Sintered Silicon Carbide rotor. Voids in the lower part of the wheel nave

NONDESTRUCTIVE CHARACTERIZATION OF CERAMIC MATERIALS:  
SMALL ANGLE NEUTRON SCATTERING

K. A. Hardman-Rhyne and E. R. Fuller, Jr.  
Ceramics Division, Institute for Materials Science and Engineering  
National Bureau of Standards, Gaithersburg, MD 20899

ABSTRACT

The use of small angle neutron scattering (SANS) is discussed as a nondestructive technique for characterizing ceramic materials. SANS is seen to be a method for quantifying distributed microstructural properties of ceramics that have been identified by alternate techniques. As such, SANS is a complimentary technique to other characterization methods. Two scattering regimes are emphasized: 1) diffraction for microstructural phenomena of less than 100 nm; and 2) beam broadening for microstructural phenomena from 100 nm to approximately 20  $\mu\text{m}$ .

INTRODUCTION

Small angle neutron scattering (SANS) techniques are used to study microstructural phenomena in the range of 1 to  $10^4$  nm in size. Since these techniques cover a wide range of sizes, they are particularly useful for studies of ceramic processing and distributed damage in ceramics. While many metal and alloy systems have used SANS techniques, only recently have experiments been conducted on ceramic materials. This is not surprising considering the difficulties inherent in analyzing SANS data on these materials. Often ceramics have several microstructural components present in the material. These include: residual pores from the sintering process, inclusions or impurities from starting materials, second phases, and microcracks or cavities from temperature and/or applied stress effects.

All these effects produce small angle neutron scattering. It is important either to eliminate all effects except the one of interest or to identify the effects through complementary techniques, such as electron or optical microscopy. While these complementary techniques can identify defects, voids, and second phases, SANS can quantify these effects throughout the bulk of the materials in a nondestructive way due to the general nature of neutrons.

Neutrons are an excellent nondestructive probe of microstructural features. Because they primarily interact with the nucleus of the atoms, neutrons are highly penetrating without disturbing the material. This penetration power allows the bulk of the material to be interrogated, whereas x-rays and other techniques are more sensitive to surface phenomena. Another strength of neutron scattering is its dependence on the chemical elements present in the material, through a quantity called the coherent scattering length. This scattering dependence varies in an

unsystematic way from one element to another, so that differences between elements with similar atomic numbers can be detected [1].

This paper will discuss NBS research using SANS to characterize ceramic materials. The main intention is to emphasize the advantages and limitations of SANS techniques and to spark interest in further SANS research on ceramics. The next section briefly describes the SANS instrument at NBS. The following section on SANS experiments is divided into two parts: 1) the diffraction scattering regime, which is applicable to small particles or defects in the range of 1 to 100 nm; and 2) the beam broadening scattering regime for defects and particles on the order of 0.1  $\mu\text{m}$  to 20  $\mu\text{m}$ . Theoretical aspects of small angle neutron scattering are not specifically discussed, but the interested reader is referred to the following articles [1-4].

### SANS INSTRUMENT

The SANS instrument at the National Bureau of Standards is described in detail elsewhere [5]; however, a diagram of the major components is shown in figure 1. The wavelength,  $\lambda$ , can be varied from 0.4 to 1.0 nm by selecting the appropriate speed of a rotating helical-channel velocity selector. This is particularly important in beam broadening experiments because the wavelength dependency of the neutron scattering is a necessary part of this analysis. Longer wavelengths are also useful in diffraction measurements, when larger size particles or voids (>500 nm) are being examined and when multiple Bragg scattering from the crystal structure of the material is to be avoided. To obtain longer wavelengths in a reasonable time period, a cold source is needed in the reactor to lower the neutron thermal equilibrium temperature, and shift peak intensities to larger wavelengths. The SANS facility at NBS is currently adding a cold source, which will increase the neutron flux at the sample significantly and will result in shorter measurement times.

Two types of collimating apertures define the beam direction and divergence. One type consists of a pair of cadmium pin hole irises, one after the velocity selector and another before the sample chamber.

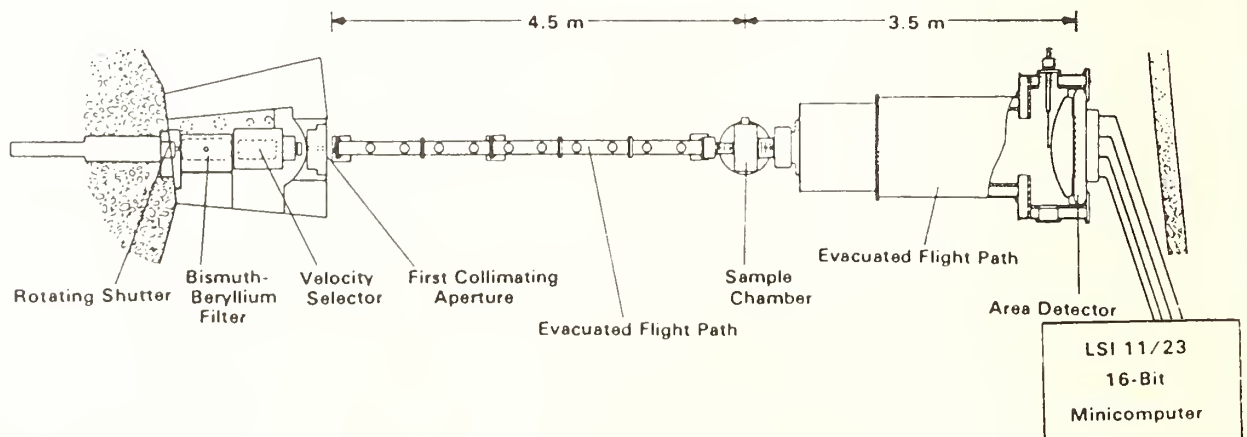


Figure 1. Diagram of the NBS small angle neutron scattering facility.

The other collimation system is for higher resolution measurements and consists of a set of channels in cadmium masks which effectively converge the neutron beam to a point at the center of the detector. A multiple sample chamber is available, which is computer controlled and can be used under vacuum. Single samples can be studied as a function of temperature from 12 to 1600 K. Horizontal and vertical field electromagnets are also available. Sample sizes are usually 10 to 25 mm in diameter and 2 to 30 mm thick. Uniform thickness is essential for analyzing the results.

The scattered neutrons are detected on a 640 mm X 640 mm position-sensitive proportional counter which is divided into 128 columns and 128 rows and has a spatial resolution of 8 mm in each direction. A dedicated minicomputer processes the signals from the detector and stores the data. The angle between the incident beam and the scattered beam is the scattering angle,  $\epsilon$ . The magnitude of the scattering vector  $Q$  is  $(4\pi/\lambda)\sin[\epsilon/2]$ , which is approximated by  $2\pi\epsilon/\lambda$  in the small angle limit.

## SANS EXPERIMENTS

Diffraction and beam broadening measurements are quite different and are usually obtained in different configurations of the SANS instrument. Diffraction experiments probe for microstructural phenomena in the range of 1 to 100 nm. The SANS detector is usually located directly behind the sample so that the incident beam is centered in the middle of the detector. The experiment generally requires 6 to 12 hours and a beamstop is used to eliminate scattering from the incident beam. Sample thickness is kept small (2 to 6 mm) to minimize multiple scattering effects. Absorption and incoherent neutron scattering should be reduced for best results in most SANS experiments with ceramic materials.

The beam broadening effect is wavelength ( $\lambda$ ) dependent with the most sensitive results occurring at  $\lambda$  greater than 0.7 nm. Typical experiments require only 3 minutes to 2 hours depending on:  $\lambda$ ; the void or particle size; the density; and the sample thickness. The incident beam is set off to one side of the detector, away from the beamstop, as the exact center of the neutron beam is needed to analyze the data. This can be done without harming the detector because the peak intensity is greatly reduced in the broadened state. Cadmium foil can be used to reduce further the scattered beam intensity over the entire detector. The samples should be measured at three wavelengths or more for best results. Also thicker samples, 5 to 30 mm, are desirable to increase the number of scattering events.

### Diffraction Regime

Most SANS experiments are in the diffraction region and in ceramics are concerned with inhomogeneities such as voids, cavities, microcracks, precipitates, sintered porosity, inclusions, nucleation, and growth of second phases. In principle, it is possible to determine quantitatively particle size, shape, size distribution, surface area and other microstructural values. Examples of SANS experiments with ceramic materials include the following: formation and growth of heterogeneities in glass by A. F. Wright [6]; creep cavitation in sintered alumina [7-8] and in silicon carbide [9-10] by R. A. Page and co-workers; growth and coarsening of pure and doped  $ZrO_2$  by A. F. Wright, S. Nunn and N. H. Brett

[11]; microcracks in sintered  $\text{YCrO}_3$  by E. D. Case and C. Glinka [12]; Fe and W inclusions in hot-pressed  $\text{Si}_3\text{N}_4$  by N. J. Tighe, K. A. Hardman-Rhyne, and Y. N. Lu [13]; and powder characterization and ceramic processing by K. A. Hardman-Rhyne, K. G. Frase, and N. F. Berk [14-16]. The study characterizing microcracks in sintered  $\text{YCrO}_3$  [12] will be briefly discussed here as it illustrates the pertinent features of SANS characterization.

To simplify interpretation of SANS data, systems with only two components, such as a matrix material and either precipitates or voids, are preferred. However, one way to avoid the complexities of analyzing a multiple component system is to run a control sample. This was done in the  $\text{YCrO}_3$  microcrack experiment [12].  $\text{YCrO}_3$  is a material which is sintered around 1750 °C, thereby establishing its microstructure (porosity, grain size, etc.), but which undergoes an apparent phase transition around 1100°C. Thus, if the material is quenched from above 1100 °C, microcracks as well as pores are present in the final material. However, if the material is annealed at 1050 °C, the microcracks can heal and only the pores remain. Thus, by subtracting the neutron scattering data of a healed  $\text{YCrO}_3$  sample from that of a microcracked sample, a difference scattering distribution, called  $I_{\text{DIFF}}$ , can be obtained, which is due only to the microcracks in the material. These difference spectra can then be analyzed to obtain quantitative information regarding the microcracks.

SANS data can be analyzed in two extremes of scattering angle,  $Q$ . For small  $Q$ , the so-called Guinier region [17], scattering is assumed to occur from sharp-edged, randomly oriented scattering centers of a given geometry. The scattering intensity in this regime is generally given by

$$I \sim V_p^2 \exp[-R_g^2 Q^2/3], \quad (1)$$

where  $V_p$  is the volume of a particle (or scattering center) and  $R_g$  is the particle's radius of gyration with respect to its center of gravity. However, a slightly different functional form for the Guinier region is obtained when the scattering from microcracks is modeled after randomly oriented thin disks of thickness  $2H$  and diameter  $2a$  [18]:

$$I \sim 2V(V_p n_p / Qa)^2 \exp[-H^2 Q^2/3], \quad (2)$$

where  $V$  is the sample volume seen by the neutron beam,  $n_p$  is the number of microcracks per volume, or the microcrack number density, and  $QH < 1 \ll Qa$ . This low  $Q$  fit to the data ( $I_{\text{DIFF}}$ ) can be seen in figure 2. This low  $Q$  scattering regime directly provides information about the microcrack opening,  $2H$ , by plotting the logarithm of the intensity times  $Q^2$  versus  $Q^2$ .

For the other extreme of scattering behavior, the high  $Q$  or Porod region, the scattering intensity has a  $Q^{-4}$  dependence [18]. The Porod region is more sensitive to smaller dimensions of the scattering centers and results in a characteristic Porod length which measures the total surface area to volume ratio, if absolute intensities can be determined. For the microcrack data, the total surface area of microcracks was estimated from the high  $Q$  data by normalizing to the scattering from water. Figure 3 shows the logarithmic function of  $I_{\text{DIFF}}$  versus the scattering vector  $Q$ . The solid line is a Porod [18] functional fit which describes the data at large  $Q$  ( $Q > 0.03 \text{ \AA}^{-1}$ ) and can be expressed in the following form:

$$I \sim (2\pi/V)(S/Q^4), \quad (3)$$

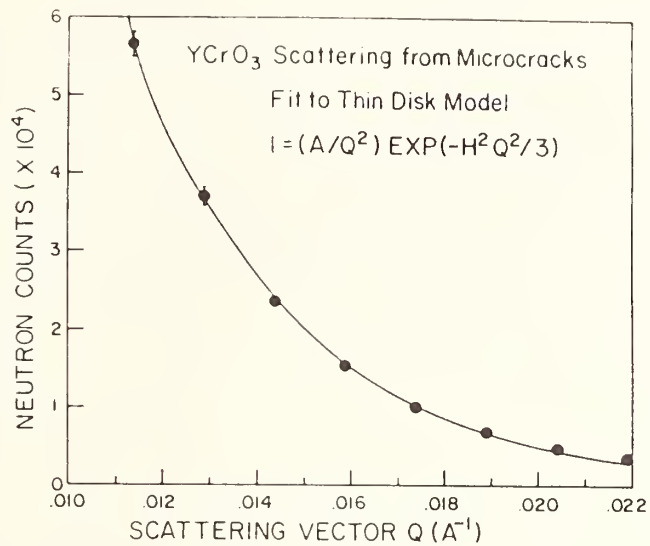


Figure 2. The low Q scattering data from microcracks in a 7 mm thick specimen of YCrO<sub>3</sub>. The solid line is a least-squares fit to a scattering function for randomly oriented thin disks of thickness 2H. From Ref. [12].

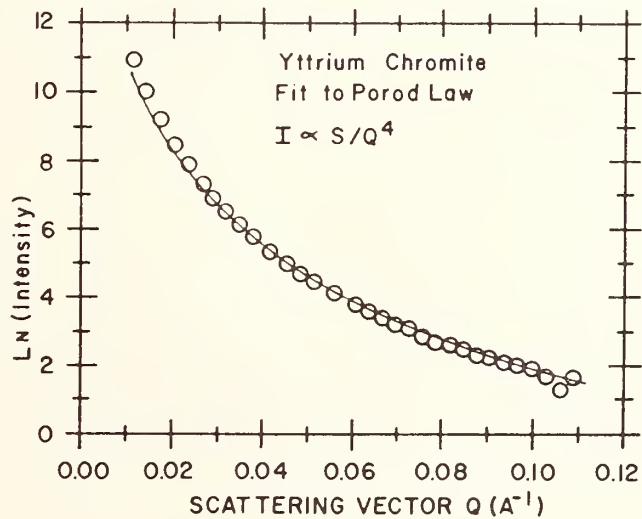


Figure 3. The net scattering due to microcracks from a YCrO<sub>3</sub> specimen. The solid line is a least-squares fit to a Porod law. From Ref. [12].

where  $V$  is the sample volume seen by the neutron beam and  $S$  is the total surface area of the scattering centers. Since  $H \ll a$ ,  $S/V \sim \pi \langle a^2 \rangle n_p$ , where  $\langle a^2 \rangle$  is the average square of the microcrack radius.

Since the SANS data alone do not provide a complete characterization of the microcrack sizes,  $a$  and  $H$ , and microcrack number density,  $n_p$ , these measurements were complimented by elasticity measurements on the specimens. The decrement in elastic modulus with microcracking gives a measure of  $\langle a^3 \rangle n_p$ , where  $\langle a^3 \rangle$  is the average of the radius cubed, thus allowing the mean microcrack radius and microcrack number density to be calculated. These microcrack parameters have been calculated and agree well with similar parameters in the literature [12]. They are as follows: microcrack number density ( $4.7 \times 10^8 \text{ cm}^{-3}$ ), volume fraction ( $2.6 \times 10^{-3}$ ), and crack opening displacement (25 nm). The mean microcrack radius of  $5.7 \mu\text{m}$  corresponds well with the measured grain size of  $6 \mu\text{m}$ , and is consistent with a model of localized stress induced microcracks.

Further SANS diffraction experiments of distributed damage due to stress and temperature are expected as this technique becomes familiar in ceramic research. Although optical and electron microscopy can identify small defects in advanced ceramic materials ( $<10 \mu\text{m}$ ), SANS can quantify the size, shape and distribution of these defects in the bulk of the material. These results, coupled with failure tests, can help in understanding and improving the structural reliability of advanced ceramic materials.

### Beam Broadening Region

Porosity is a critical aspect in the densification process of a sintered ceramic material. To elucidate the extent of such porosity, a quantitative study with SANS has been conducted at NBS to determine average pore size. Rather than restricting the SANS measurements to the typical 1 to 100 nm size regime of SANS diffraction, we have explored the neutron beam broadening region by extending the SANS characterization into the tens of micrometers size regime [4,14]. This extension of SANS technique to larger sizes is an important development, because it allows a greater overlap of SANS characterization with other NDE techniques. In addition, as this new regime of scattering analysis has developed, it has found use in numerous other ceramic processing applications, e.g., powder characterization [14-15]. The technique is illustrated here by a characterization of the porosity in a  $\text{YCrO}_3$  material.

Two samples of  $\text{YCrO}_3$  were fabricated from pure powders by isostatic pressing at 207 MPa (30,000 psi); and one of the samples was sintered. The density of the "green" compact (the unfired ceramic) was approximately 57% of theoretical density and that of the sintered material was approximately 94%. The starting ceramic powder, with approximately 30% of theoretical density, was also examined. Since beam broadening measurements are wavelength dependent, SANS experiments were taken at six or seven of the following wavelengths: 0.485, 0.545, 0.625, 0.700, 0.800, 0.900, 0.950, 1.00 nm. The observed scattering revealed a striking difference between the samples as illustrated in figures 4(a) and 4(b), which are SANS spectra for the sintered and "green" compact specimens, respectively. The sintered material [figure 4(a)] shows little wavelength dependence. In contrast, the "green" compact reveals dramatic beam broadening that is strongly wavelength dependent [see figure 4(b)]. This dependence is illustrated in figure 5 by plotting the normalized intensity versus scattering vector  $Q$

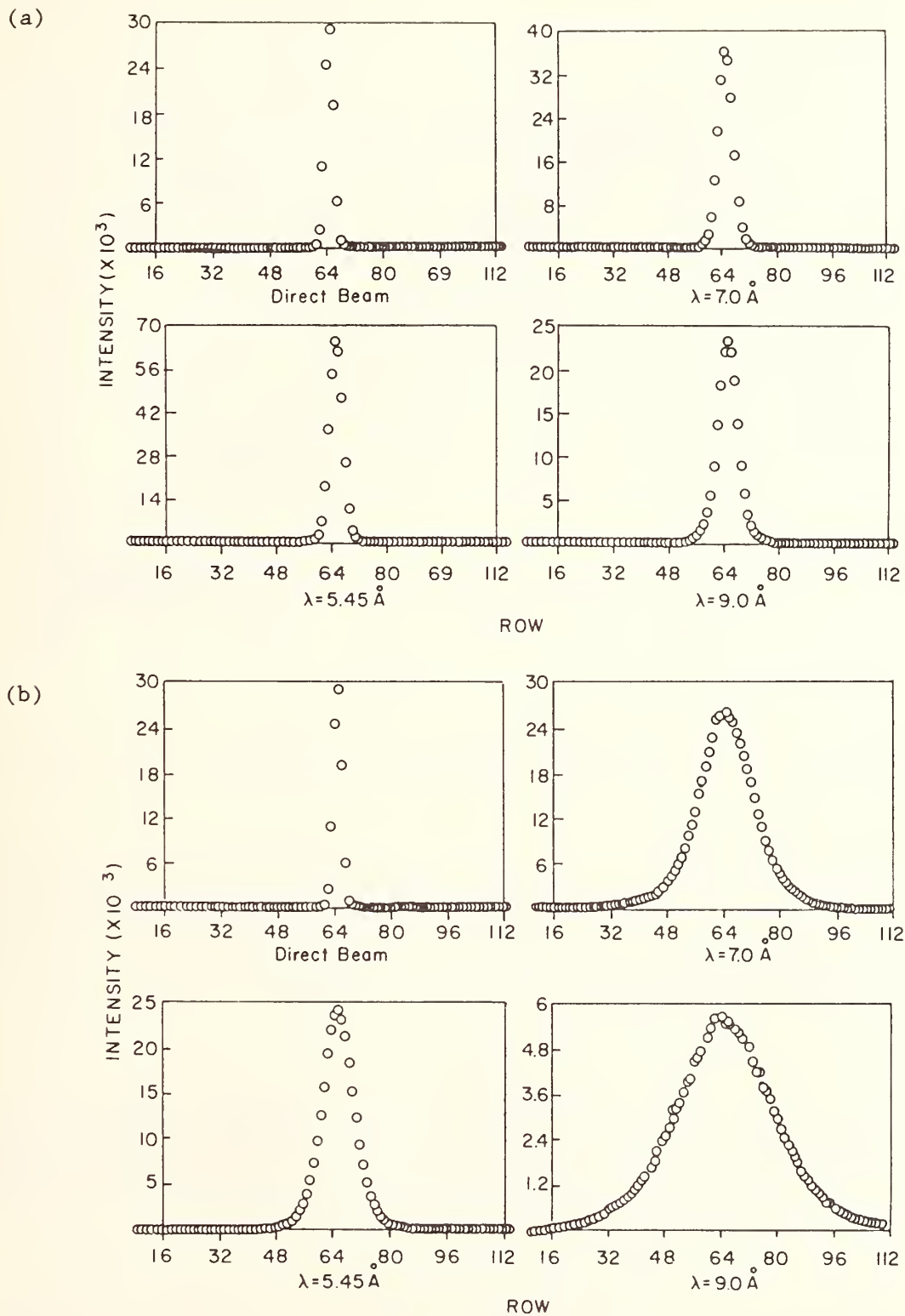


Figure 4. SANS spectra at three wavelengths (a) for a sintered compact of  $\text{YCrO}_3$  and (b) for a "green" compact of  $\text{YCrO}_3$ . Plotted is the scattering intensity versus a linear column slice (detector row number) through the center of the scattering plane.

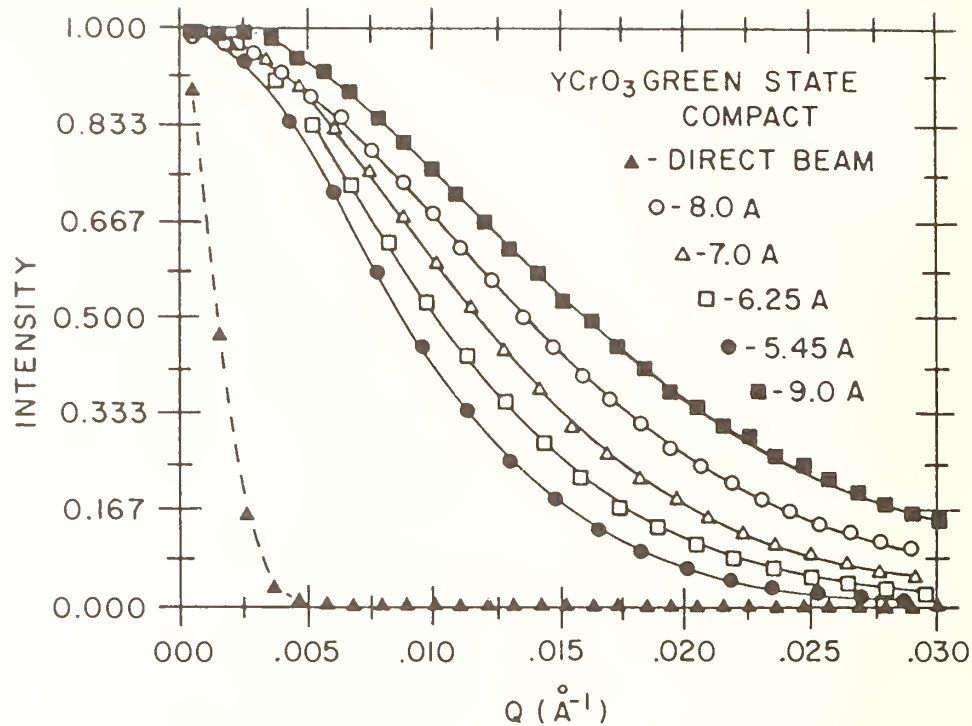


Figure 5. Normalized scattering intensity versus scattering vector,  $Q$ , for SANS from a "green"  $\text{YCrO}_3$  compact at five wavelengths.

for five wavelengths.

The direct beam is wavelength independent with respect to the scattering angle,  $\epsilon$  and is defined in part by the instrumental collimation. Beam broadening data can resemble a Gaussian distribution at low  $Q$  values, where the full width at half maximum,  $\Delta\epsilon$  can be determined by the Gaussian standard deviation parameter  $\sigma_G$  as shown below:

$$I = I_0 \exp[-Q^2/2\sigma_G^2] \quad (4)$$

For full width a half maximum  $\Delta Q = 2.355 \sigma_G$ . Since  $Q = 2\pi\epsilon/\lambda$ , the angular variation,  $\Delta\epsilon$ , is given by  $0.3748 \lambda\sigma_G$ . The  $\Delta\epsilon$  value contains both the beam broadening scattering and that due strictly to the direct (unscattered) beam, thus the contribution from the direct beam,  $\epsilon_b$ , must be subtracted from the experimentally determined value,  $\epsilon$ , to obtain  $\Delta\epsilon$ :

$$\Delta\epsilon = [\epsilon^2 - \epsilon_b^2]^{1/2}. \quad (5)$$

Although the qualitative aspects of the data clearly demonstrate a strong effect of ceramic processing on the neutron scatterers population in these materials, quantitative measures of the particle or void size, shape and size distribution are less straightforward. Moreover, the neutron phase shifts are well within an intermediate range of values for which neutron scattering is not expected to be analyzable by multiple refractive

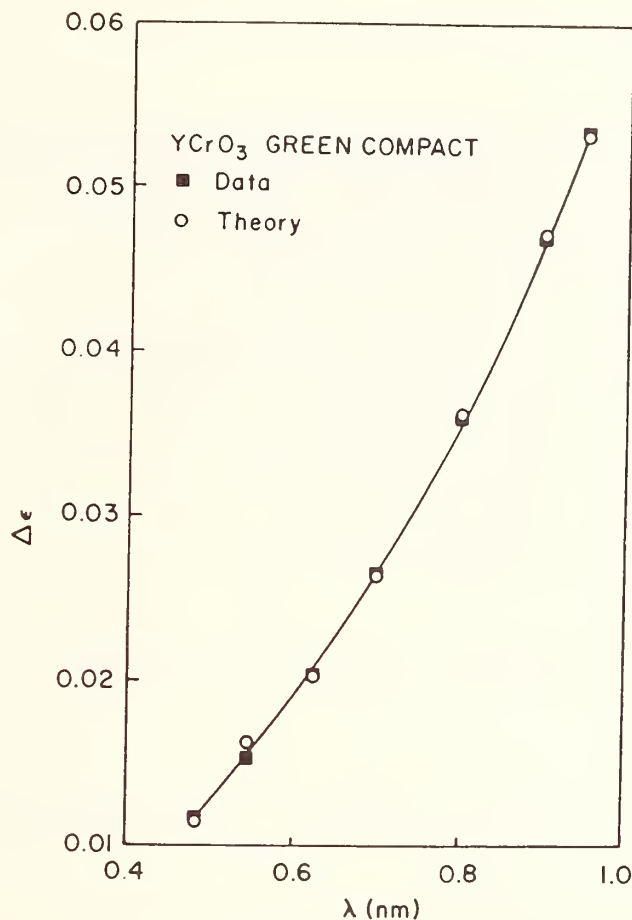


Figure 6. Full width at half maximum,  $\Delta\epsilon$  (in radians), versus the wavelength,  $\lambda$ , for voids in a "green"  $\text{YCrO}_3$  compact. The squares are the data and the circles are the  $\Delta\epsilon$  values derived from theory.

behavior alone. Therefore, a generalized beam broadening theory [4] relevant for this region and multiple refraction has been developed to quantitatively analyze the SANS data for densified ceramics and other distributed defects in this size regime. Radius, void (or particle) density ratio and shape factor can be obtained from this theory, which can be expanded to consider particle packing, polydispersivity and various shapes of particles and voids other than spheres. Excellent agreement of data and theoretical values for  $\Delta\epsilon$  can be seen in figure 6. The average radius void size in the  $\text{YCrO}_3$  "green" compact material is  $0.17 \mu\text{m}$  and has a void density ratio of 0.42 compared to the overall density ratio of 0.43.

The general beam broadening theory and SANS technique allows us to study the densification process in a nondestructive way. It is being extended to study the sintering of spinels ( $\text{MgAl}_2\text{O}_4$ ) as a function of temperature [16]. In-situ as well as other ceramic processing experiments are expected to develop fully the capabilities of this new approach in SANS. These techniques should also have applications in a number of other material disciplines, such as magnetic broadening effects, pores in metal alloys and colloidal chemistry.

## REFERENCES

1. Kostorz, G., Treatise on Materials Science and Technology, Vol. 15, ed., G. Kostorz, Academic Press, New York, 5-8 & 227-289 (1979).
2. Weertman, J. R., Nondestructive Evaluations: Microstructural Characterization and Reliability Strategies, eds. O. Buck and S. M. Wolf, American Institute of Mining, Metallurgical, and Petroleum Engineers, New York, 147-168 (1981).
3. Herman, H., Non-Destructive Evaluation of Materials with Cold Neutron Beams, report to Naval Air Systems Command, Contract No. N00019-77-M-0418, Washington, DC, December 1977.
4. Berk, N. F.; Hardman-Rhyne, K. A., *J. Appl. Cryst.* **18**, 467-472 (1985).
5. Glinka, C. J., AIP Conference Proceedings No. 89, J. Faber, ed., Neutron Scattering-1981, 395 (1981).
6. Wright, A. F., Neutron Scattering 1981 AIP Conference Proceedings, ed., J. Faber, 359 (1982).
7. Page, R. A.; Lankford, J.; Spooner, S., *J. Mater. Sci.* **19** [10], 3360-3374 (1984).
8. Page, R. A.; Lankford, J.; Chan, K. S.; Hardman-Rhyne, K. A.; Spooner, S., *J. Am. Ceram. Soc.* **70** [3], 137-145 (1987).
9. Page, R. A.; Lankford; Spooner, S., *Acta Metall.* **32** [9], 1275-1286 (1984).
10. Page, R. A. and Spooner, S., *J. Mater. Sci.* **21** [4], 1417-1422 (1986).
11. Wright, A. F.; Nunn, S.; Brett, N. H., in Proceedings of the Conference on Zirconia, Stuttgart, West Germany, 1983.
12. Case, E. D.; Glinka, C. J., *J. of Mater. Sci.* **19** [9], 2962-2968 (1984).
13. Tighe, N. J.; Hardman-Rhyne, K. A.; Lu, Y. N., *Ceram. Eng. & Sci. Proc.* **6**, 835-849 (1985).
14. Hardman-Rhyne, K. A.; Berk, N. F., *J. Appl. Cryst.* **18**, 473-479 (1985).
15. Hardman-Rhyne, K. A.; Frase, K. G.; Berk, N. F., *Physica B* **136B** [1-3], 223-225 (1986).
16. Frase, K. G.; Hardman-Rhyne, K. A., to be published.
17. Guinier, A., X-ray Diffraction, Chapter 10, W. H. Freeman and Company, San Francisco, 1963.
18. Porod, G., *Acta Phys. Austriaca* **2**, 255 (1948).

NBS/BAM - Symposium on  
Materials Research and Testing

Introduction to the Versailles Project on  
Advanced Materials and Standards (VAMAS)  
Technical Working Area: Wear Test Methods  
By: S. Becker and J. Lexow

In June 1982 at the Economic Summit of Versailles the Working Group "Technology, Growth and Employment" proposed a multilateral collaboration on science and technology. One of the recommendations concerned "Advanced Materials and Standards".

By now, several Technical Working Parties have been launched. The Technical Working Area "Wear Test Methods" has the following aims:

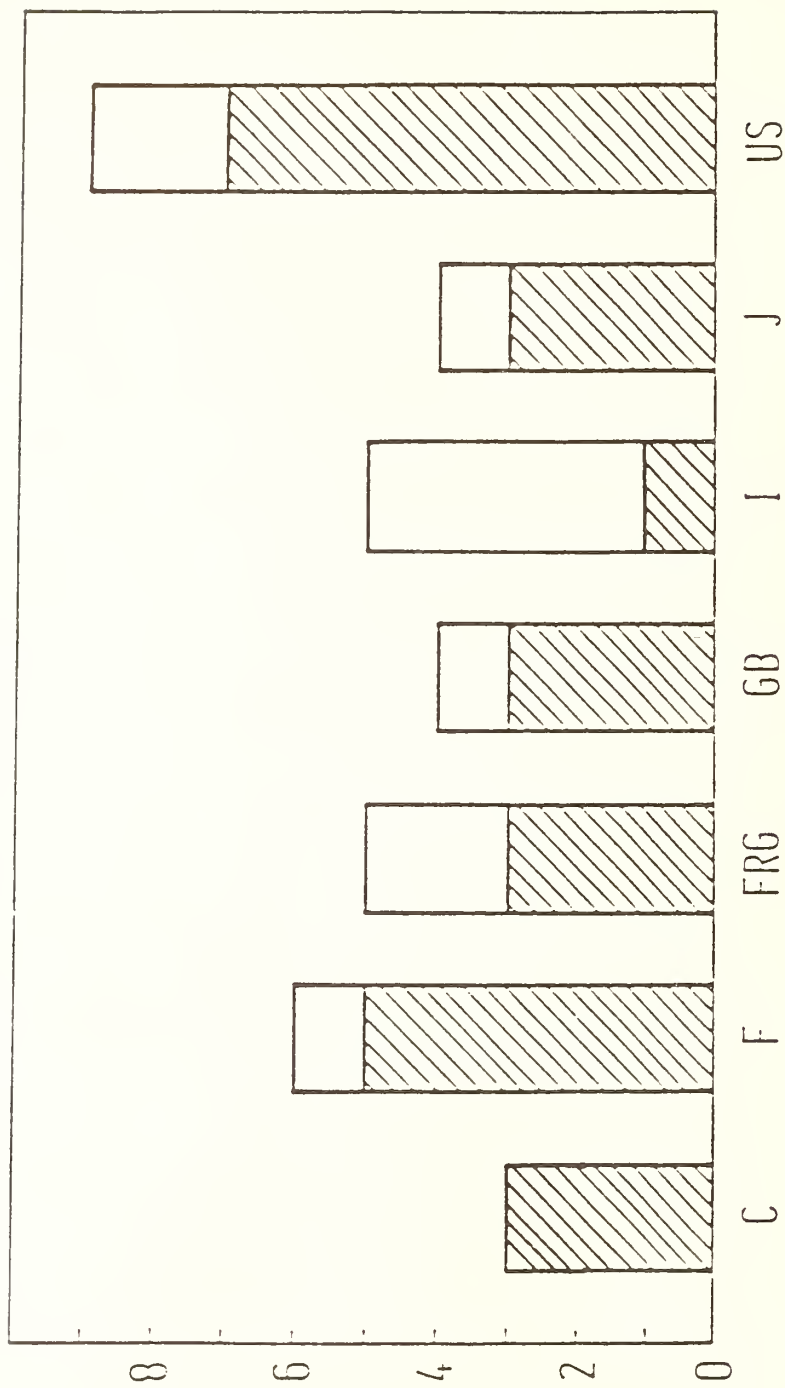
- Improvements of the reproducibility and comparability of wear testing by developing internationally agreed wear test methodologies.

- Characterization of the wear behaviour of "advanced" materials in comparison with conventional materials.

As a first step a Round Robin on the wear behaviour of a ball-on-disc sliding test system consisting of four pairings of  $\alpha$ - $\text{Al}_2\text{O}_3$  ceramic and steel (AISI52100) under agreed test conditions like load, sliding velocity, temperature and sliding distance was conducted. By May '86 about two thirds of the participants had already delivered their test results. The evaluation of the reports is now under way. It is rather difficult because of the many influencing factors that have to be considered.

For the different material combinations typical wear patterns were observed including for example material transfer (steel/steel and steel/ceramic) and very minor wear for the  $\text{Al}_2\text{O}_3$  couple. The viewgraphs 4 - 11 show some of the BAM-results.

The final results of the Round Robin will be communicated to the participants and to the public as soon as the evaluation has been completed.



□ number of participants ( 36 )

▨ number of reports sent in ( 25 ) as of May 1986

INSTRUCTION SHEET  
FOR VAMAS-PROJECT ROUND ROBIN  
WEAR TEST METHODS

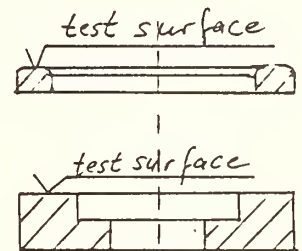
Please Perform Tests at the following Agreed Test Procedure \*

1. Test System

- Stationary ball (10mm diameter) against rotating disc (40mm outer diameter, 32mm wear track diameter)
- rotation in the horizontal plane
- direction of rotation of disc to be indicated by each laboratory
- Ball, disc and debris are to be collected and protectively stored in plastic containers.
- Holders for disc and ball are to the discretion of each laboratory.
- Please report (if possible) vibrations (e.g. vibration amplitudes and frequency distribution) of test rig at stated location.
- Report stiffness-data of the test rig (if available).

2. Materials

- Disc: AISI 52100  
alpha-Al<sub>2</sub>O<sub>3</sub>  
SiC )  
SiAlON ) to be supplied later  
Si<sub>3</sub>N<sub>4</sub> )  
Ball: AISI 52100  
alpha-Al<sub>2</sub>O<sub>3</sub>  
AISI 52100 coated with Ni as per N.B.S. ) in preparation



3. Atmosphere

Laboratory air (50±10% rel. humidity; 23±1°C)  
(If a different atmosphere is applied it will have to be documented and reported with the test results.)

4. Lubricant

No lubricant will be used in the first stage of the round robin tests.

5. Operating Variables

- Motion: Continuous unidirectional sliding
- Velocity: 0.1 m/s
- Normal Load: 10 N
- Temperature: 23±1°C
- Sliding distance: 1 km or  
until f=1.5 or  
until displacement due to wear = 1 mm
- Number of tests: 3 - 5

---

\*If other conditions are used please indicate them.

p.t.o.

## 6. Preparation of Surfaces

- Specimen are to be used as received, i.e. no mechanical surface finishing is necessary.
- Surfaces are to be cleaned immediately prior to each test.
  - a) Washing in freon ( $\text{Cl}_2\text{FC}-\text{CF}_2\text{Cl}$ ) is preferred to washing in ethylalcohol since the water content in the alcohol may corrode the metallic surfaces
  - b) Drying in warm air
  - c) Rinsing with hexane
  - d) Drying in a drying oven at  $110^\circ\text{C}$ , 30 min
- Chemicals of pure quality are to be used.
- Samples are to be stored and transported in desiccators.

## 7. Measurements

- a) Wear:
  - (Please define whether wear of ball, wear of disc, or total wear of both ball and disc are measured.)
  - Continuously measured and recorded
  - Specimens weighed before and after each test
  - Wear scar diameter on ball to be measured with an optical microscope
  - Wear of ball and disc
  - Profilogram results of both surfaces before and after the test
- b) Friction:
  - (Please define whether the friction force or the friction torque are measured.)
  - Submit a simplified graph giving the fluctuations at the beginning and at the end, minimum and maximum deviations during the test etc..
- c) Debris:
  - All debris is to be collected (See 1).

## 8. Post-Measurement Handling

- Indicate the sample number with a water resistant felt pen on the side of the disc which was not subjected to wear.
- Mark the worn area on the ceramic ball with a water resistant felt pen after each test; first with red, second with blue, third with green.
- After the first and second test turn the ceramic ball into a new position without contaminating the sample.
- Put the samples back into the bags immediately after the test and the examinations in order to avoid mixing.

## 9. Examination

Surfaces and debris are to be examined by optical color photography and SEM techniques. Photographs at standard magnifications 50x, 100x, 200x, 500x, 1000x

## 10. Report

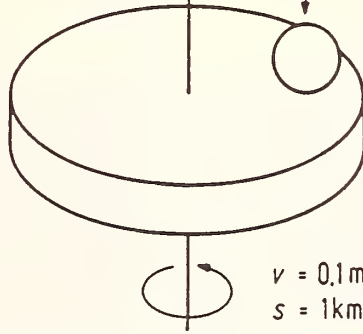
All results should be reported to Prof. Czichos by  
January 31, 1986.

Reports should in particular comprise:

- Information on the test setup
- Photographs of surfaces
- Graphs of wear and friction
- Additional information on deviations from agreed conditions or other information concerning the test.

$T = 23^\circ\text{C}$   
50% r.h.

$F_N = 10\text{N}$



$v = 0,1\text{m/s}$   
 $s = 1\text{km}$

Material pairings			Measurements
disc \ ball	steel	alumina	• Friction force
steel	kit 1	kit 2	• Wear (system, ball, disc)
alumina	kit 3	kit 4	• Wear surfaces (SEM, profilometry)

B A M  
Berlin

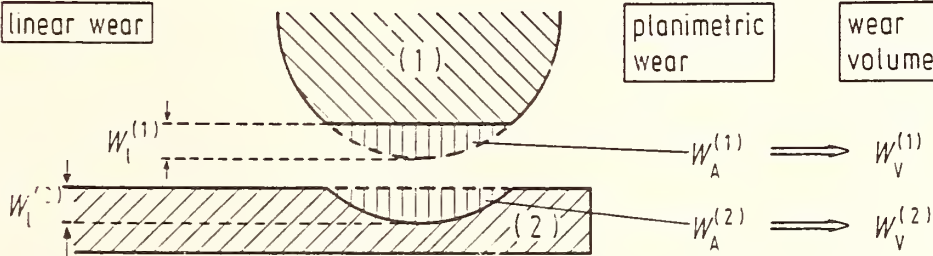
Wear test conditions

Becker  
86 52 1321

linear wear

planimetric wear

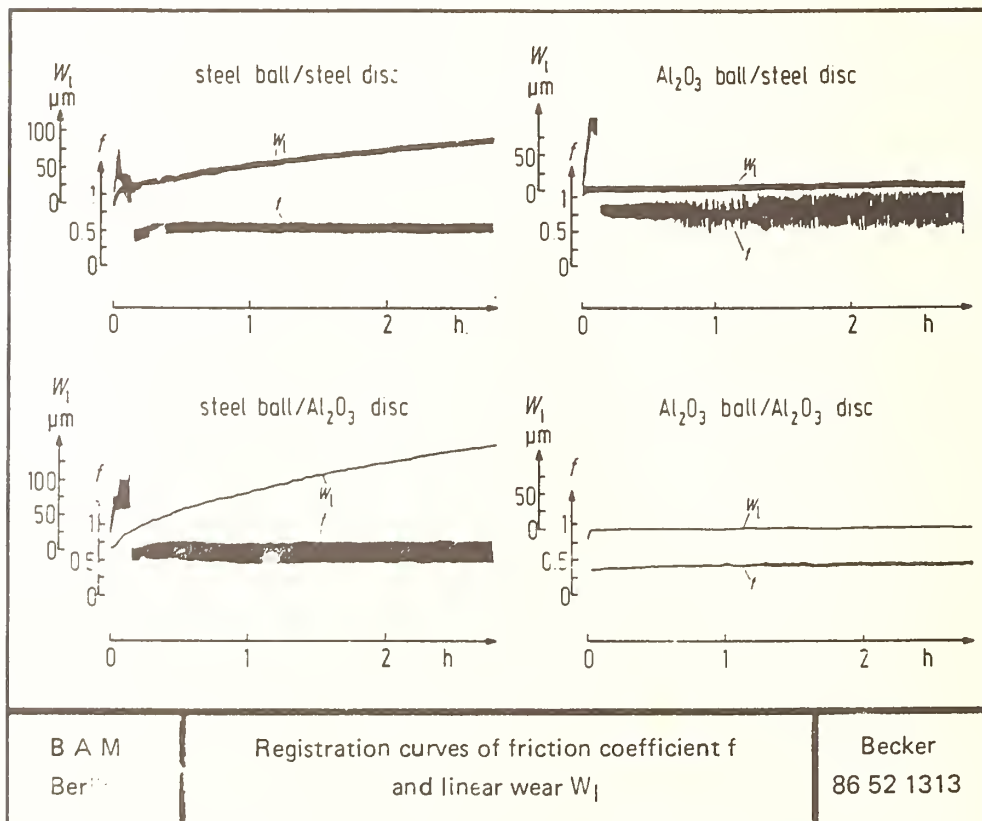
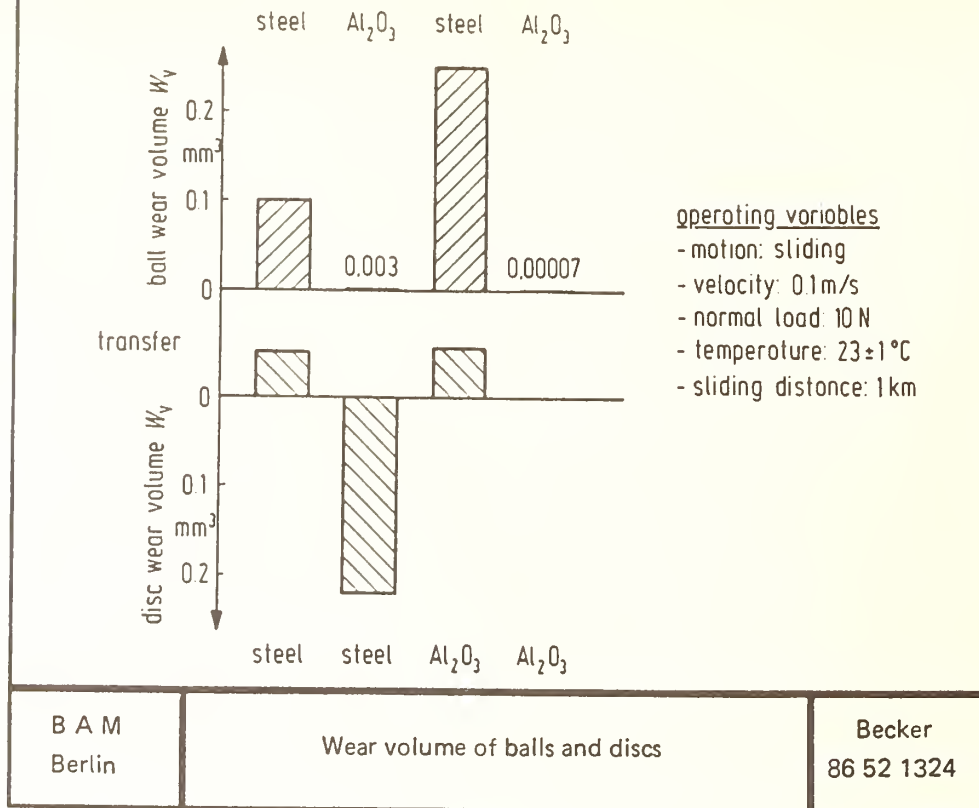
wear volume



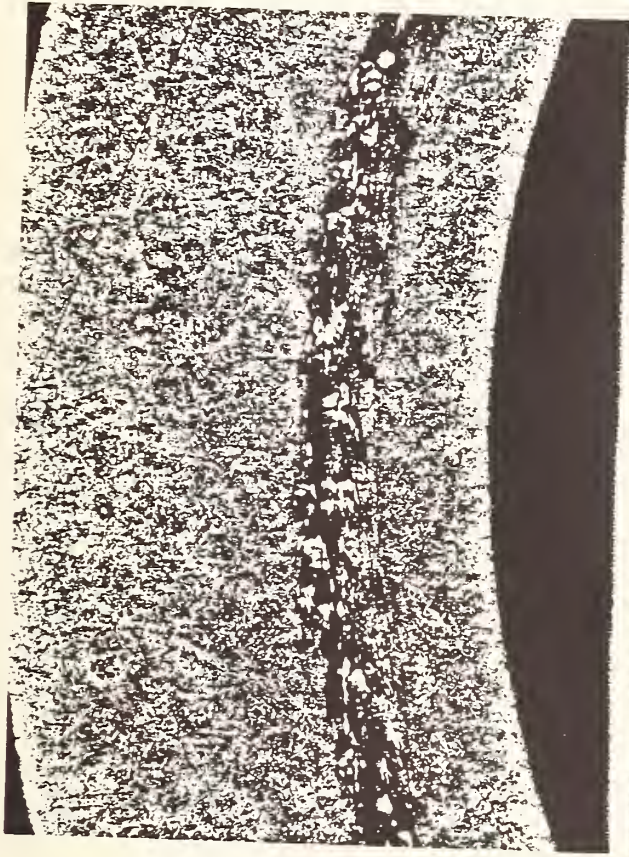
E A M  
Berlin

Evaluation of wear

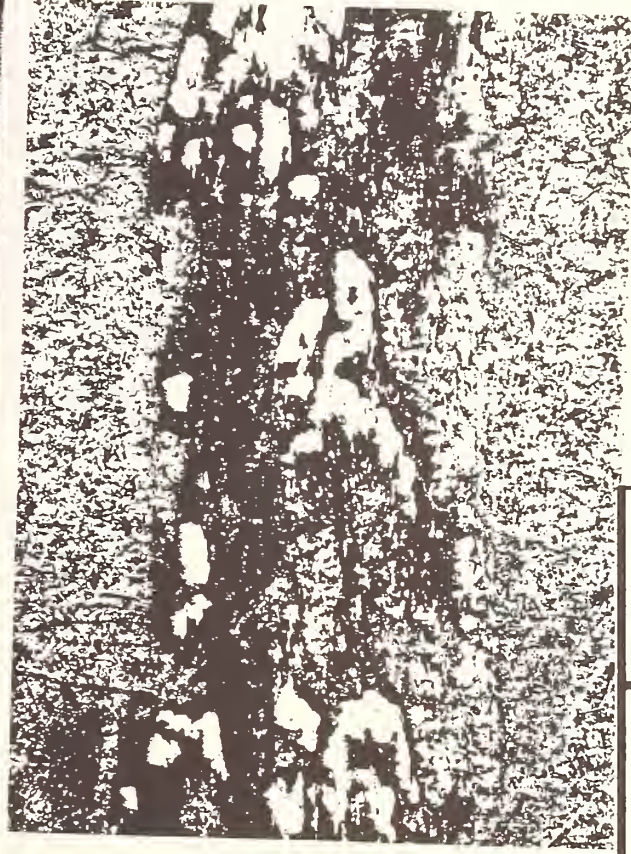
Becker  
86 52 1322



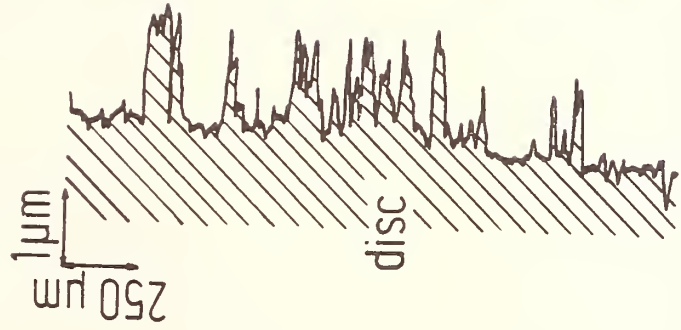
disc: 100 Cr 6 ( AISI 52100 )



1mm



200 μm



B A M  
Berlin

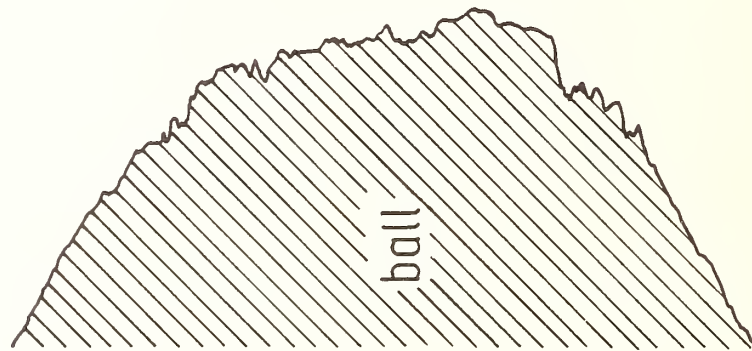
Wear track  
Kit 1: steel ball vs. steel disc

Becker  
86 52 1314

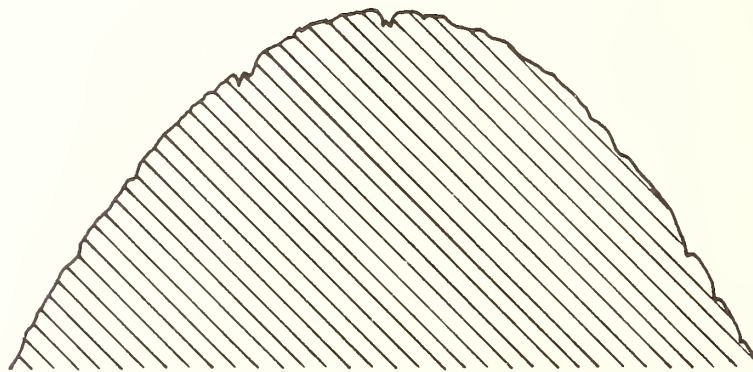
ball:  $\alpha - \text{Al}_2\text{O}_3$



100  $\mu\text{m}$



ball

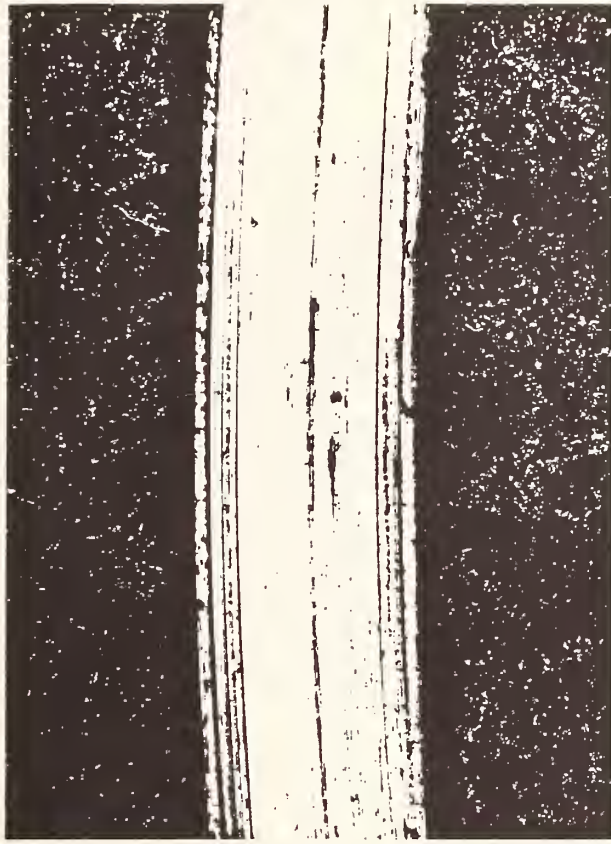


100  $\mu\text{m}$

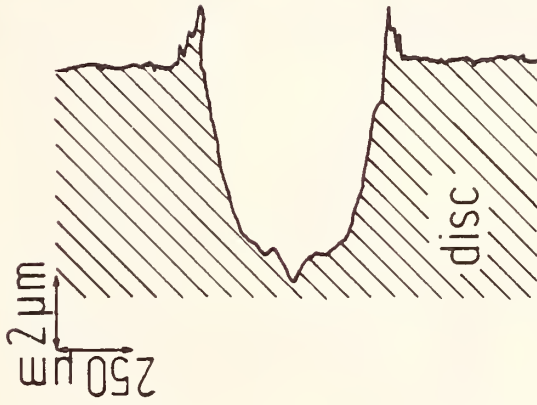
unworn surface      wear scar

B A M Berlin	Wear scar Kit 2: ceramic ball vs. steel disc	Becker 86 52 1316
-----------------	---	----------------------

disc: 100Cr6 ( AISI 52100 )



200  $\mu\text{m}$

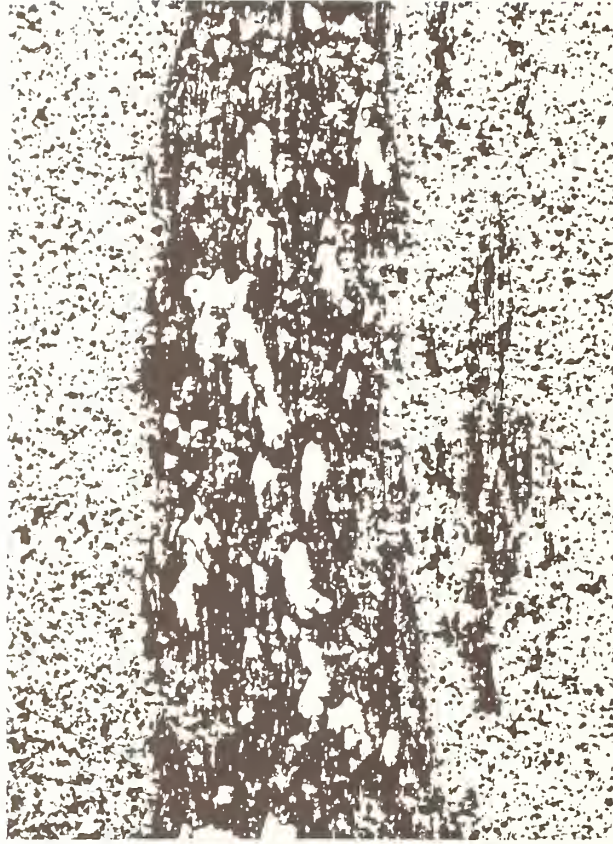
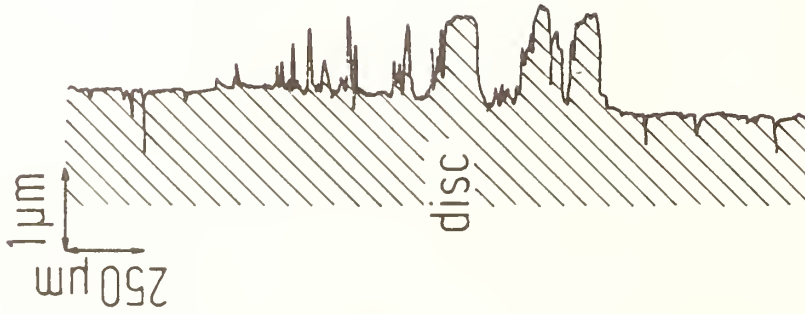


B A M  
Berlin

Wear track  
Kit 2; ceramic ball vs. steel disc

Becker  
86 52 1315

disc:  $\alpha - \text{Al}_2\text{O}_3$



B A M Berlin	Wear track Kit 3: steel ball vs. ceramic disc	Becker 86 52 1317
-----------------	--	----------------------

disc:  $\alpha$  -  $Al_2O_3$



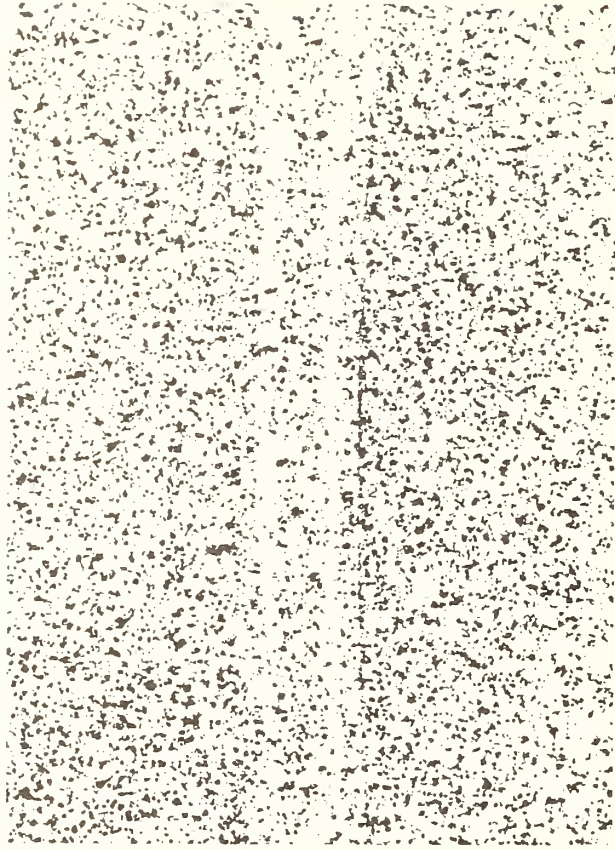
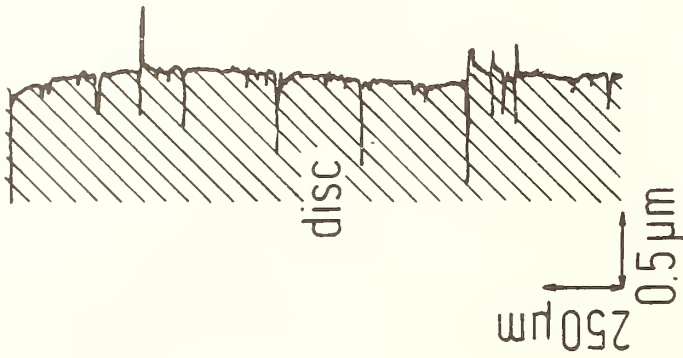
30  $\mu$ m



3  $\mu$ m

B A M Berlin	Steel transfer on ceramic disc Kit 3: steel ball vs. ceramic disc	Becker 86 52 1318
-----------------	--	----------------------

disc:  $\alpha - \text{Al}_2\text{O}_3$

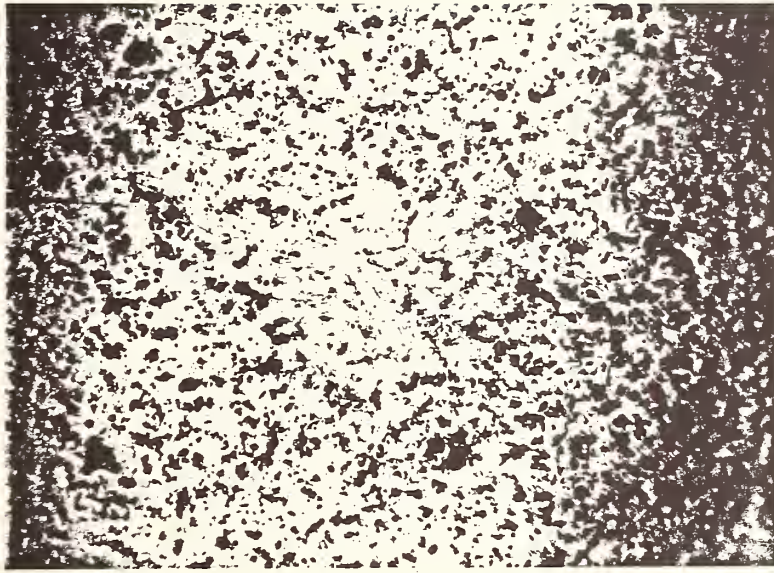


B A M  
Berlin

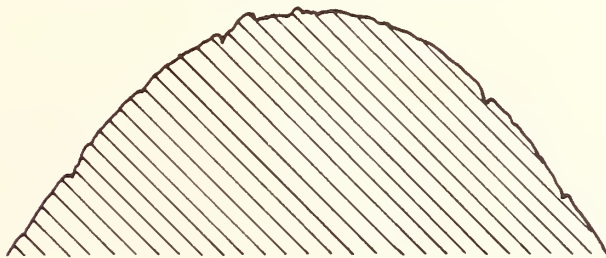
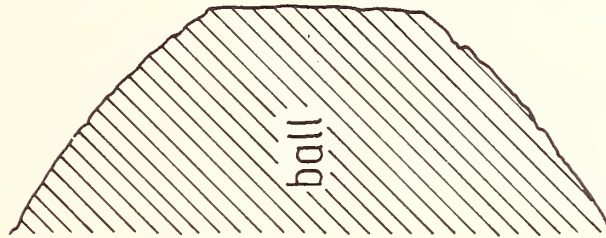
Wear track  
Kit 4: ceramic ball vs. ceramic disc

Becker  
86 52 1319

ball:  $\alpha - \text{Al}_2\text{O}_3$



100  $\mu\text{m}$



100  $\mu\text{m}$   
5  $\mu\text{m}$

unworn surface      wear scar

B A M Berlin	Wear scar Kit 4: ceramic ball vs. ceramic disc	Becker 86 52 1320
-----------------	---	----------------------

## Fretting of Ceramic Materials

by Dr.-Ing. Dieter Klaffke

Modern engineering ceramics are of world wide interest in many fields of technical applications.

The tribological behaviour of ceramics is not yet well known, investigations of friction and wear behaviour should accompany the further development of ceramic materials.

The fretting wear test (oscillating sliding motions with small stroke) is a useful tool for the study of tribological behaviour of materials; wear processes are concentrated on a small part of specimens so that wear volumes are to be evaluated with good accuracy.

A tribometer for fretting tests has been developed which enables to measure the friction force, the linear wear and the contact resistance during the tests. Fretting tests have been performed with different ceramic materials against ceramics and steels.

In fretting tests with steel (ball : AISI 52 100) against different ceramics the oxide-ceramics (alumina, partially stabilized zirconia) show much less wear than silicon nitride and silicon carbide.

In fretting test with ceramic cylinders against different steels with different thermochemical surface layers, again the oxides show less wear than the silicon-based ceramics. The lowest wear of the steel occurs if it is protected by a vanadium carbide layer.

Wear processes in the case of ceramic against ceramic are of pronounced heterogeneous character, showing peaks in the time behaviour as well of the linear wear as of the coefficient

of friction, caused by stochastically removing of hard wear particles. The coefficient of friction in the steady state is in all cases higher than 0.4 and for some combinations of ceramics as high as 0.9.

The humidity of surrounding atmosphere can have a pronounced influence on wear and friction behaviour. In dry air (5 % r.h.) the coefficient of friction is in the range 0.6 to 0.8 for SiC against itself and drops down to values below 0.2 for 95 % r.h. The wear volumes are about one order of magnitude greater in air of low humidity than at high humidity.

Specially in dry air wear processes show a pronounced two range behaviour, starting with high wear rate, than changing to mild wear at a transition point which seems to depend very sensitively on the relative humidity.

Fretting of Ceramic Materials

D. Klaffke

NBS/BAM-Symposium on  
Materials Research and Testing

Subject: Ceramic Materials

Berlin, 22.04.86

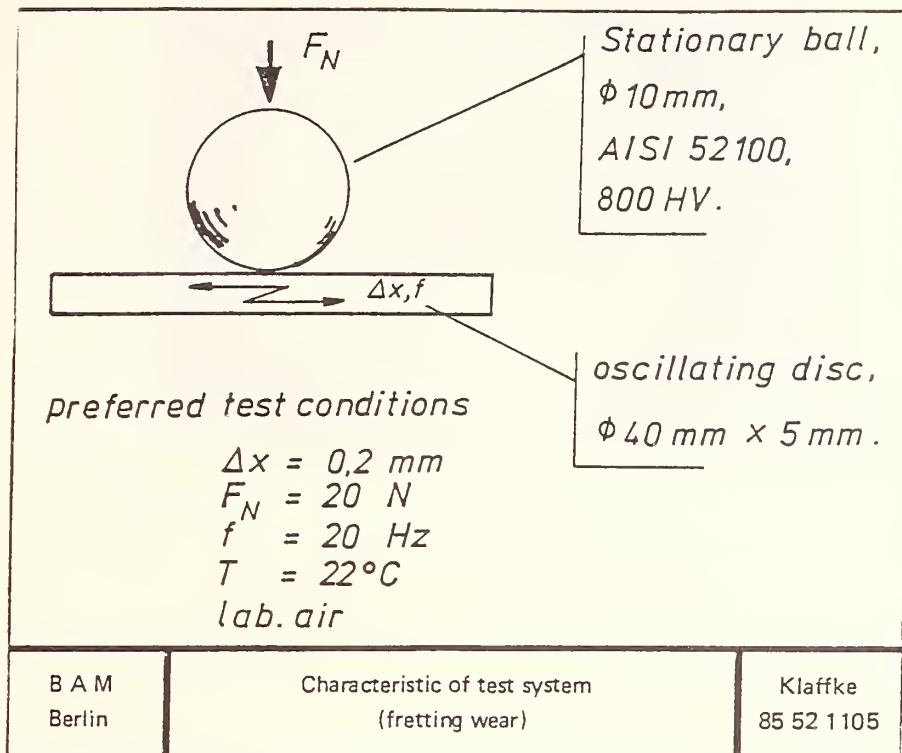


Fig. 1

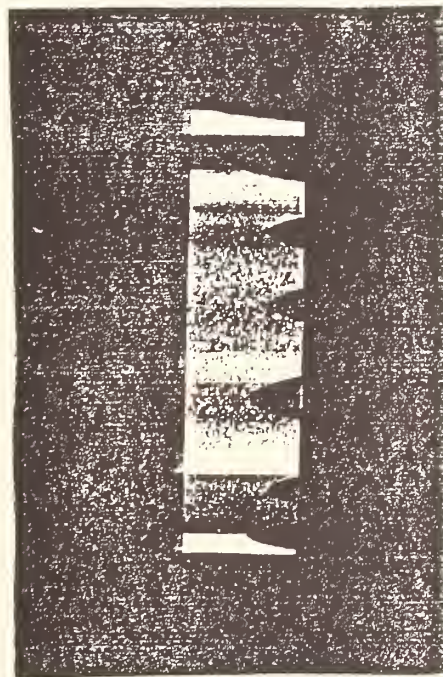


Fig. 2 Fretting test specimen (cylinder)

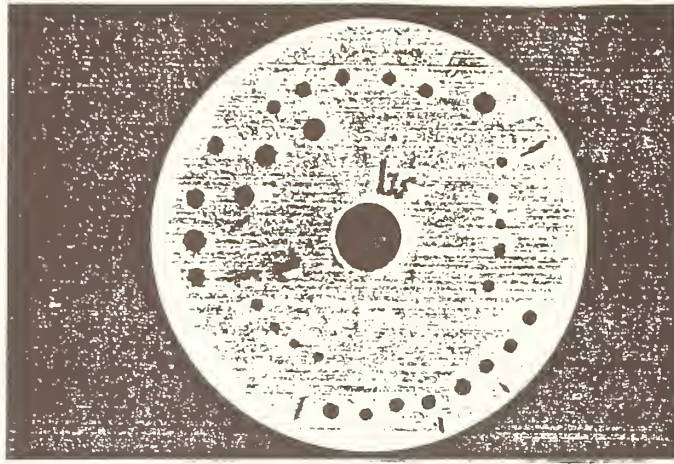


Fig. 3 Fretting test specimen (flat)

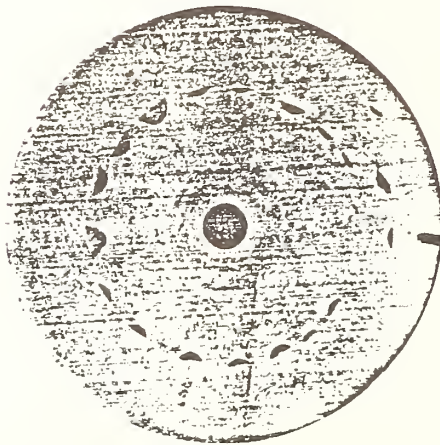


Fig. 4 Fretting test specimen (SiC)

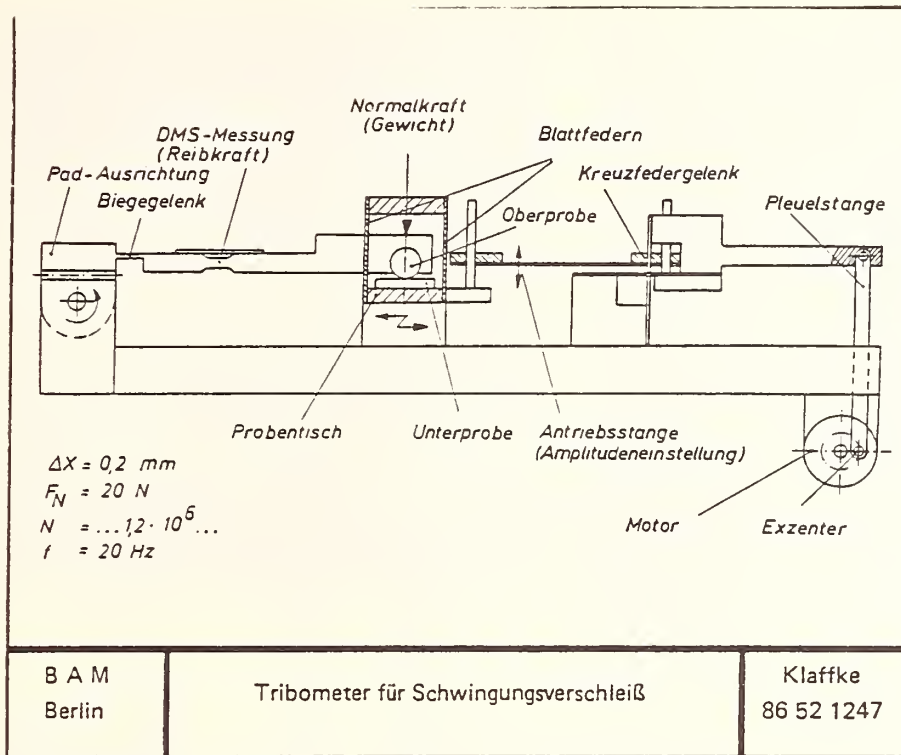


Fig. 5 Tribometer for fretting wear

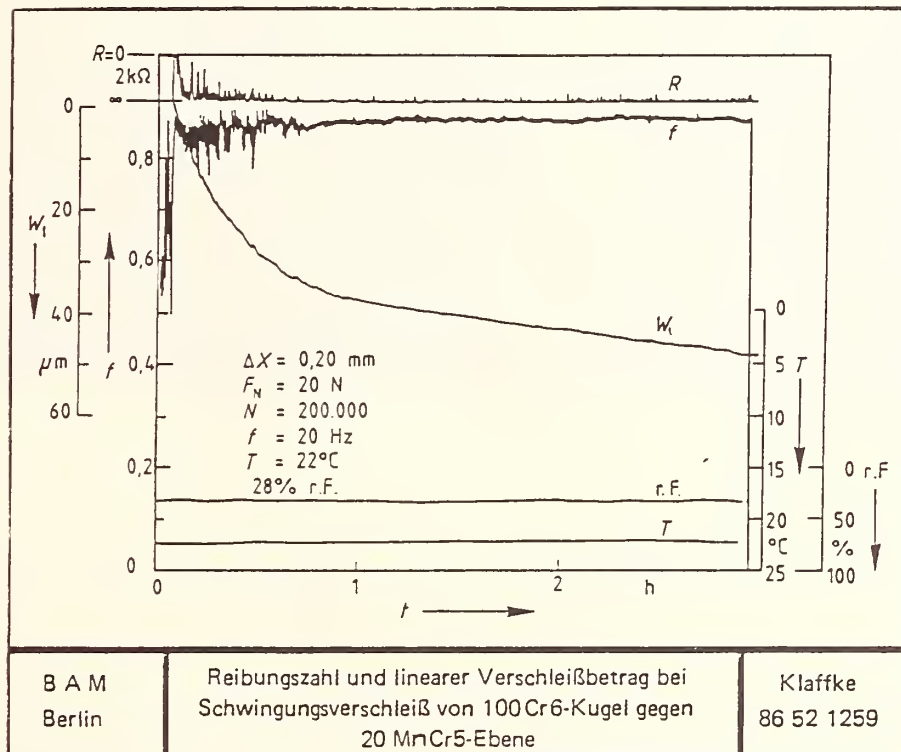


Fig. 6 Coefficient of friction and linear wear as function of time in a fretting test; steel/steel

Werkstoff	nähere Bezeichnung	Form	$R_a$	$\mu m$	$R_z$	Farbe
Si <sub>3</sub> N <sub>4</sub>	drucklos gesintertes	Zylinder	0.7		4.3	hell-
	Siliziumnitrid	Ebene	0.25		2.0	grau
ZrO <sub>2</sub>	MgO-teilstabilisiertes	Zylinder	0.8		5.0	gelb
	Zirkonoxid	Ebene	0.2		2.6	
Al <sub>2</sub> O <sub>3</sub>	Aluminiumoxid mit	Zylinder	1.6		9.8	weiß
	98,5 % Al <sub>2</sub> O <sub>3</sub>	Ebene	1.0		8.0	
SiSiC	Silizium infiltrier-	Zylinder	0.2		1.0	dunkel-
	tes Siliziumcarbid	Ebene	2.6		18.9	grau
SSiC	gesintertes Silizium-	Zylinder	0.1		0.9	mittel-
	carbid	Ebene	0.2		1.7	grau

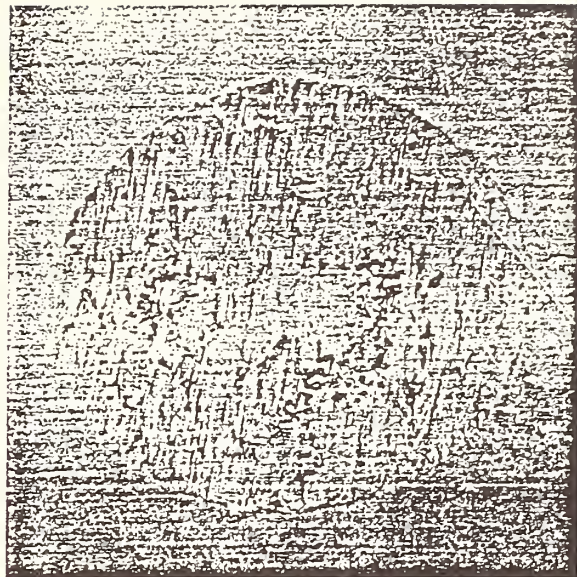
  

B A M Berlin	Zusammenstellung der untersuchten keramischen Werkstoffe	Klaffke 86 52 1249
-----------------	---	-----------------------

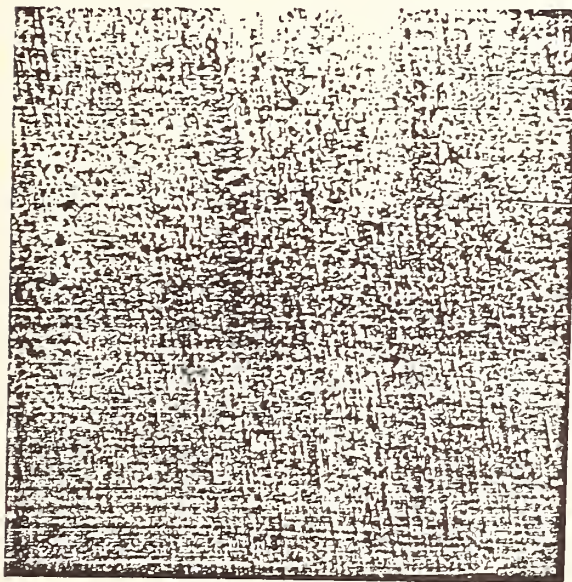
Fig. 7 Ceramic materials used in fretting tests



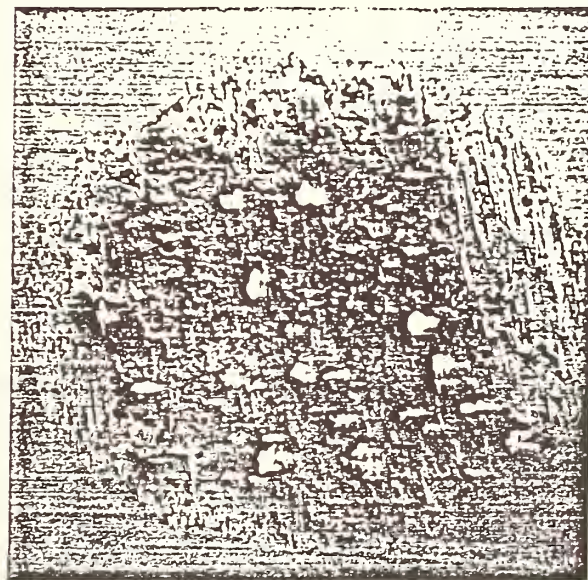
$Si_3N_4$



$ZrO_2$



$Al_2O_3$



$SiSiC$

Fig. 8 Wear scars (SEM) on steel balls after fretting tests against ceramics

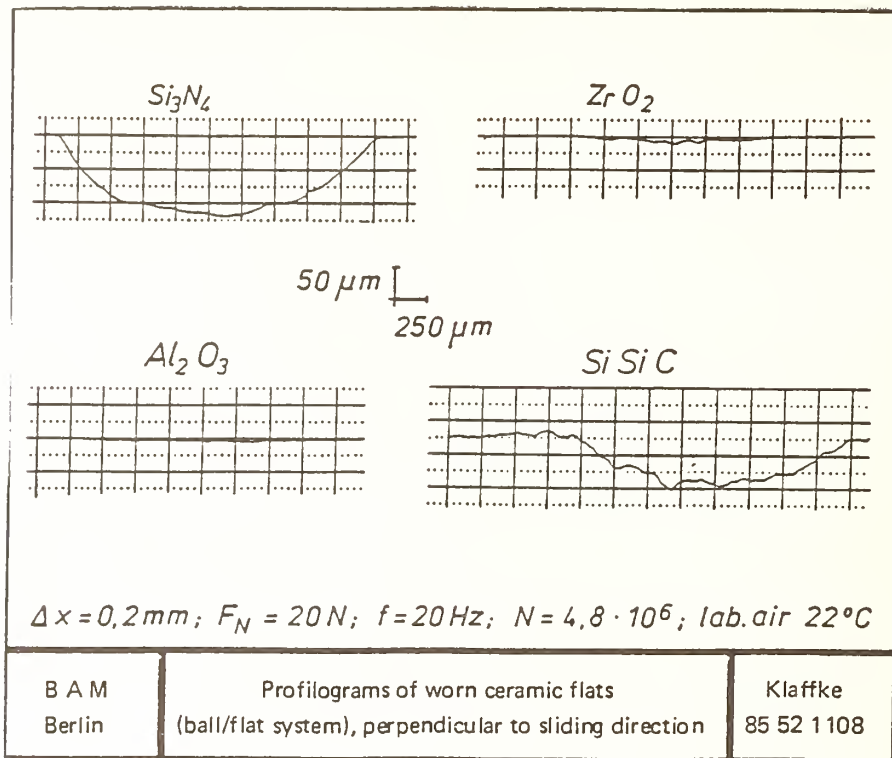


Fig. 9

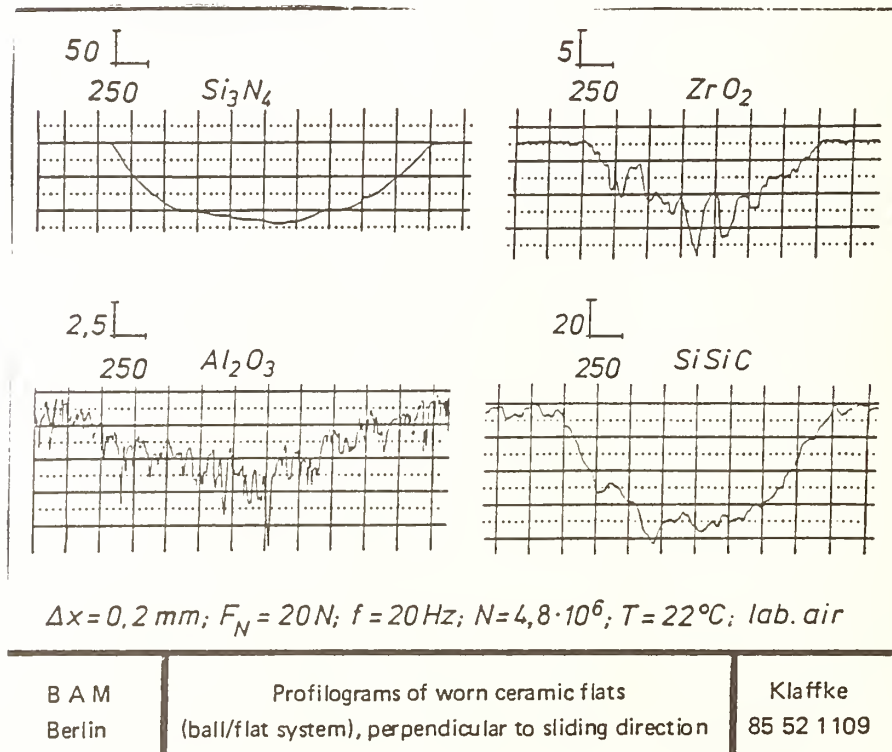


Fig. 10

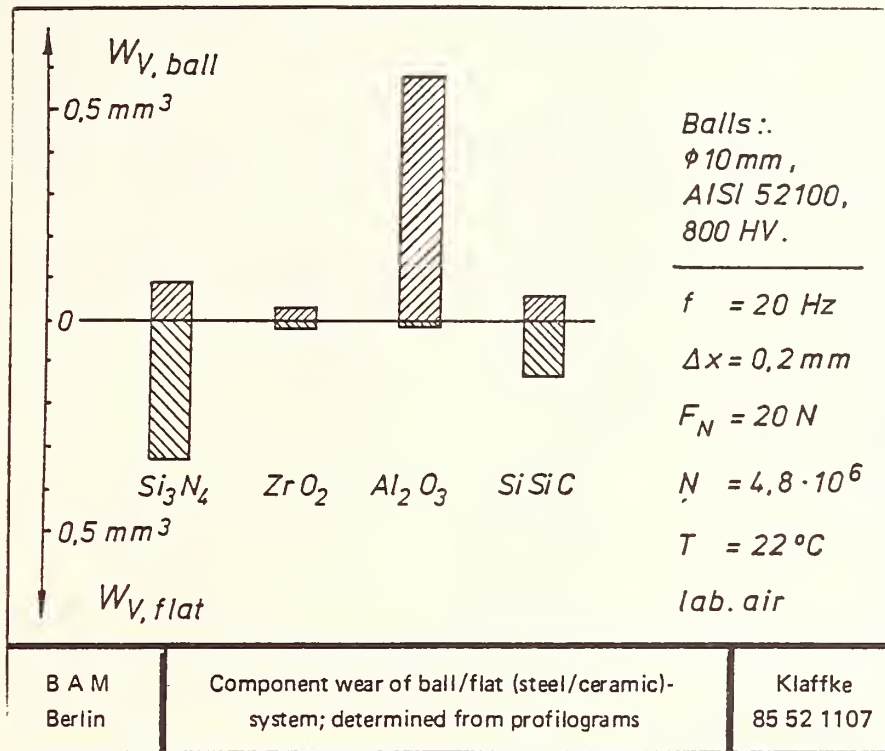


Fig. 11

Stahl	Wärme- behandlung	HV 0,2 (HV 0,4)	$R_a$ $\mu\text{m}$	$R_z$
90MnV8	Vergüten	400	.03	.28
90MnV8	Vanadieren	880	.13	1.03
90MnV8	Chromieren	(1120)	.03	.22
42CrMoS4	Vergüten	350	.03	.26
42CrMoS4	Borieren	(1500)	.09	.71

B A M Berlin	Zusammenstellung der untersuchten Stahlwerkstoffe	Klaffke 86 52 1250
-----------------	---	-----------------------

Fig. 12 Steel used in fretting tests against ceramic materials

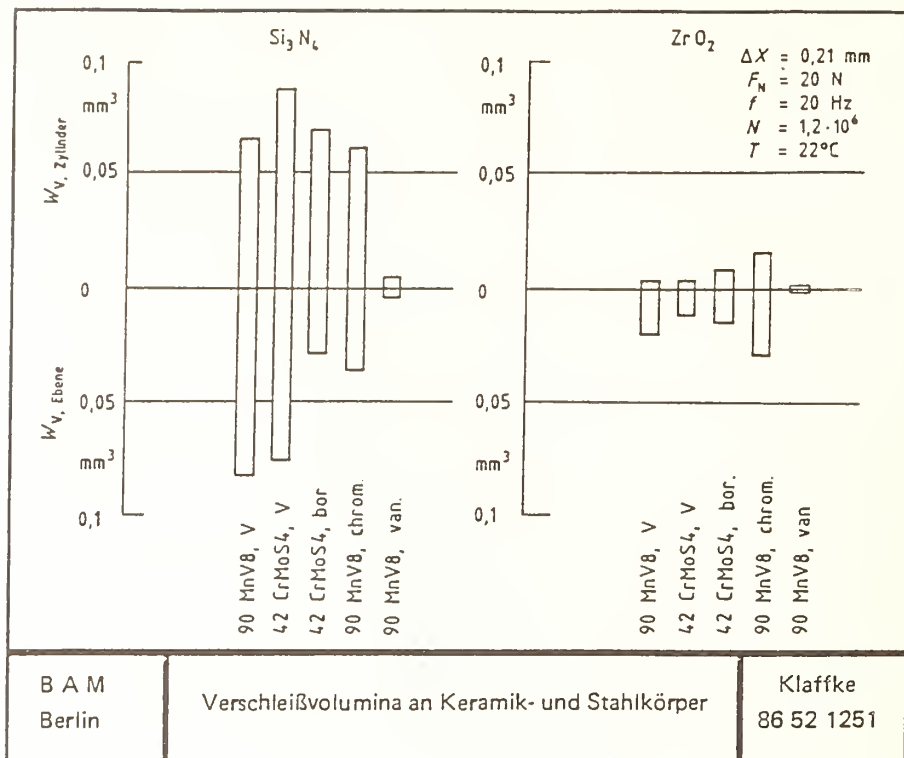


Fig. 13 Wear volumes of ceramic and of steel specimens after fretting tests

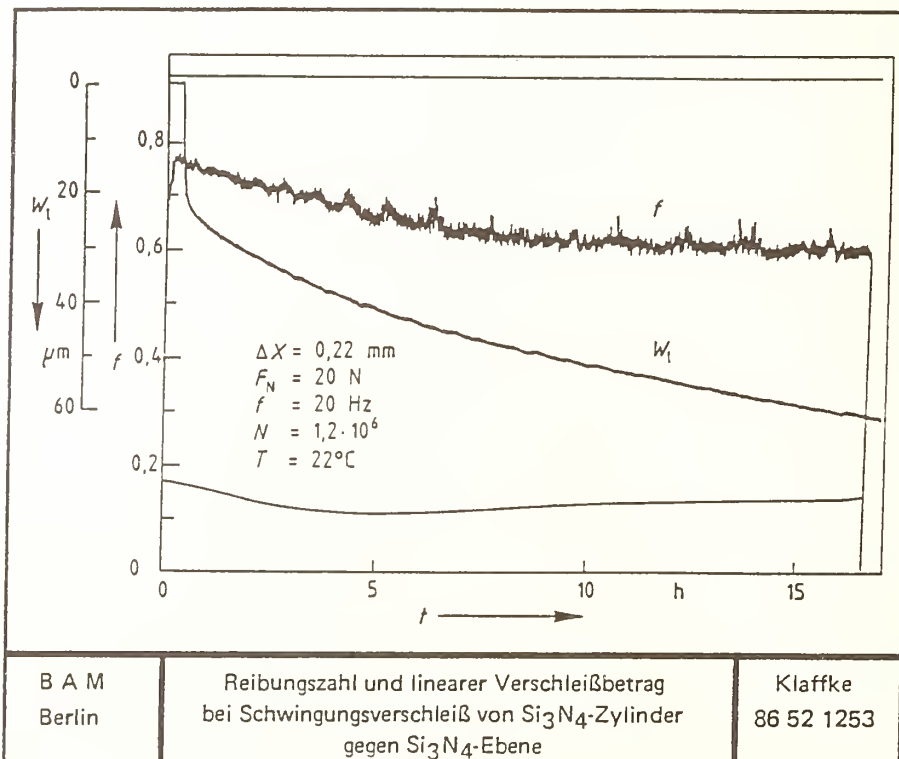


Fig. 14 Coefficient of friction and linear wear in a fretting tests;  $\text{Si}_3\text{N}_4 / \text{Si}_3\text{N}_4$

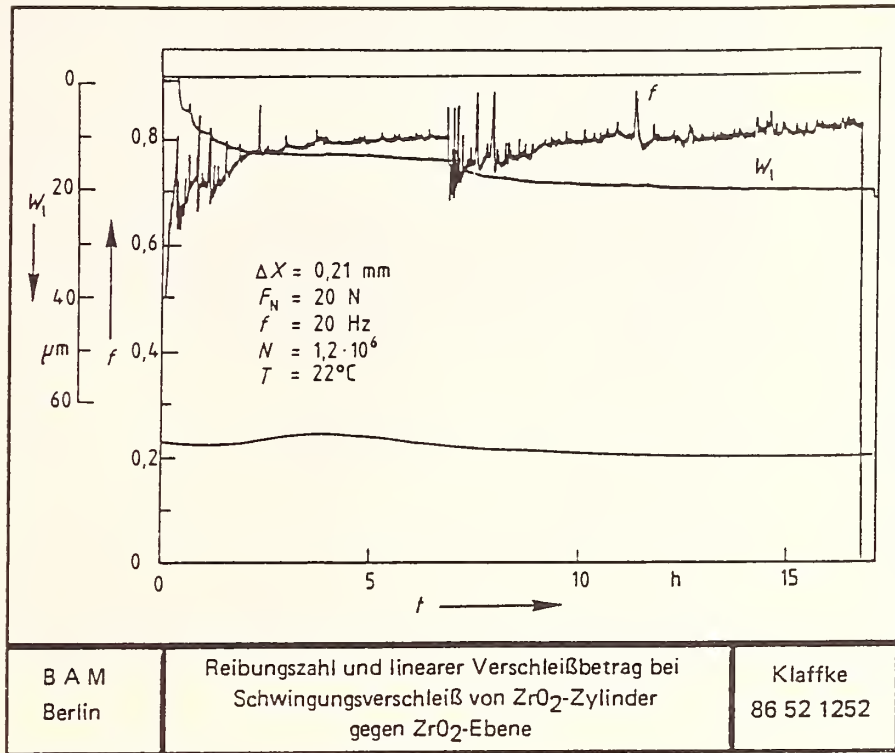


Fig. 15 Coefficient of friction and linear wear in a fretting test;  $\text{ZrO}_2 / \text{ZrO}_2$

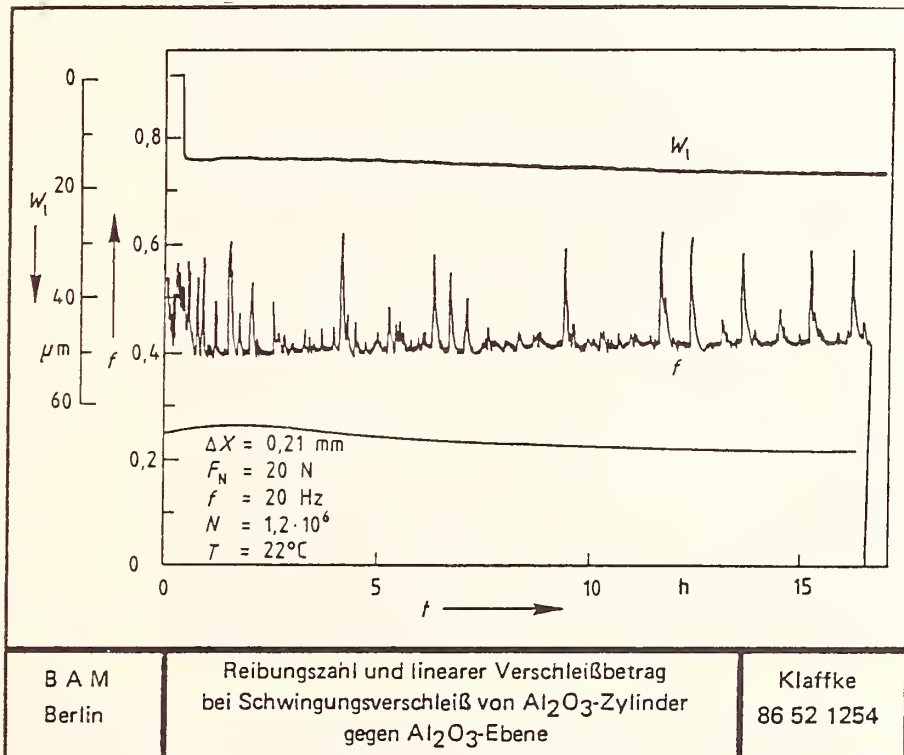


Fig. 16 Coefficient of friction and linear wear in a fretting test;  $\text{Al}_2\text{O}_3 / \text{Al}_2\text{O}_3$

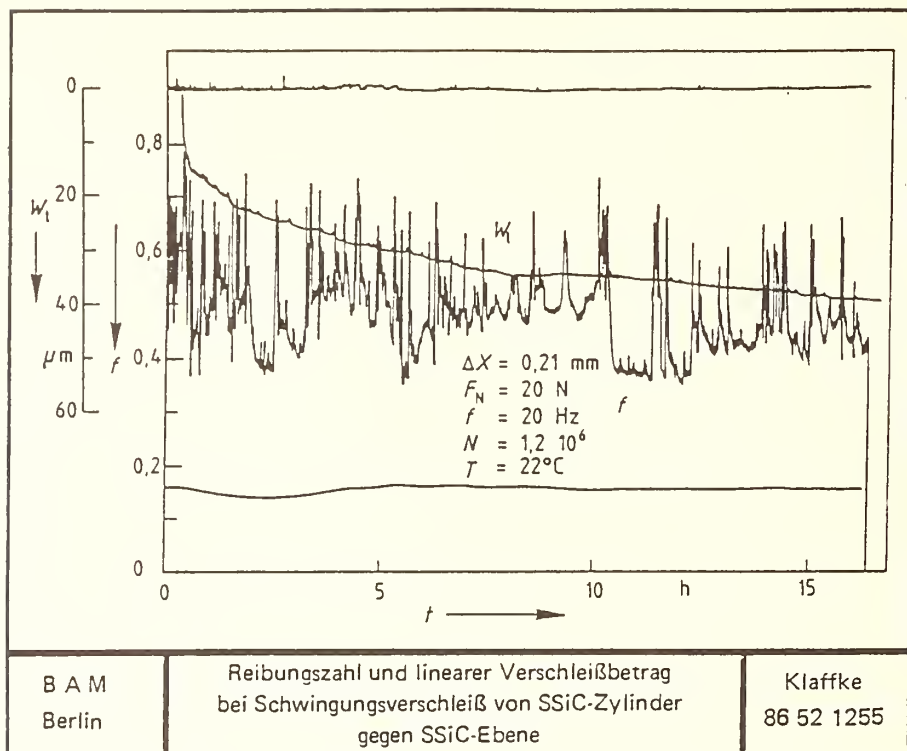
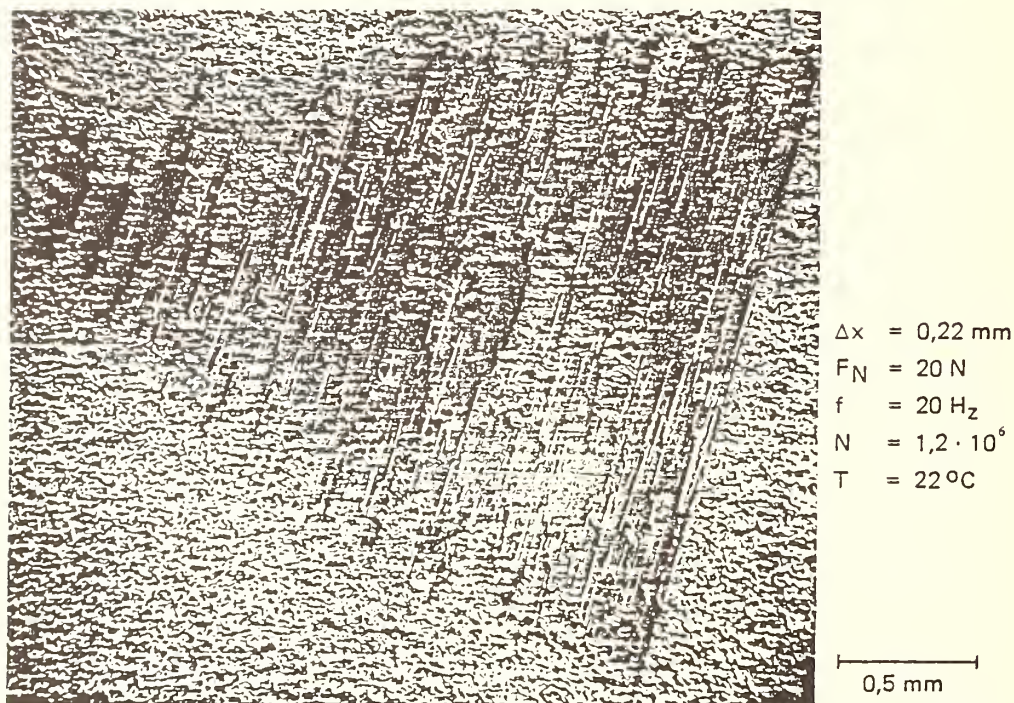
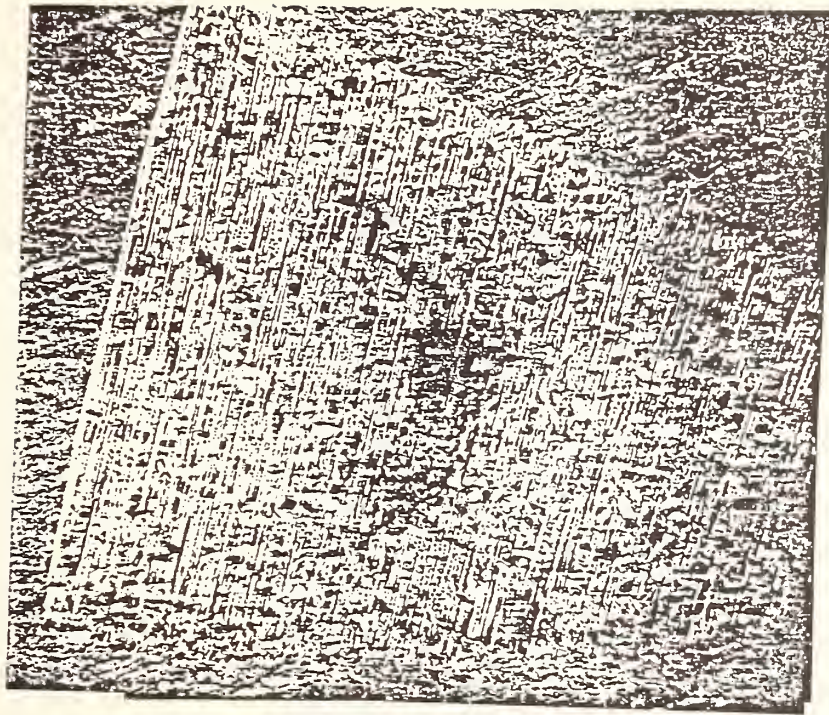


Fig. 17 Coefficient of friction and linear wear in a fretting test; SSiC/SSiC



B A M Berlin	REM Aufnahme der Verschleißspur in der $Al_2O_3$ -Ebene nach Schwingungverschleiß gegen SSiC-Zylinder	Klaffke 86 52 1258
-----------------	---	-----------------------

Fig. 18 SEM micrograph of wear scar on the  $Al_2O_3$  plane, counterbody; SSiC - cylinder

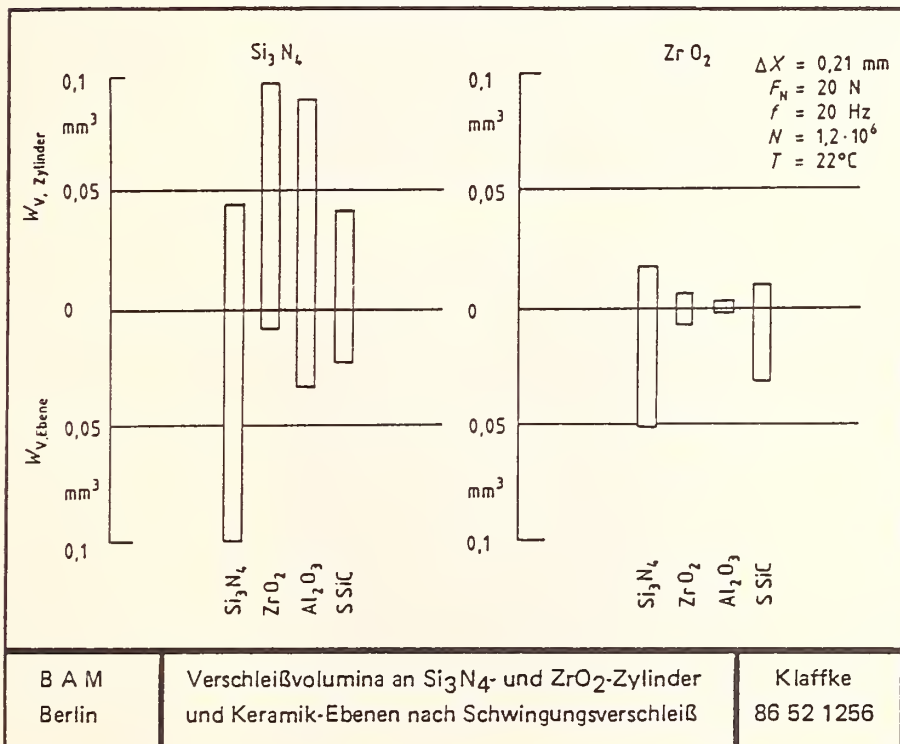


$\Delta x = 0,22 \text{ mm}$   
 $F_N = 20 \text{ N}$   
 $f = 20 \text{ Hz}$   
 $N = 12 \cdot 10^6$   
 $T = 22^\circ\text{C}$

0,5 mm

B A M Berlin	REM Aufnahme der Verschleißspur in der SSiC-Ebene nach Schwingungverschleiß gegen Si <sub>3</sub> N <sub>4</sub> -Zylinder	Klaffke 86 52 1257
-----------------	--	-----------------------

Fig. 19 SEM micrograph of wear scar on the SSiC plane counterbody Si<sub>3</sub>N<sub>4</sub> - cylinder



B A M Berlin	Verschleißvolumina an Si <sub>3</sub> N <sub>4</sub> - und ZrO <sub>2</sub> -Zylinder und Keramik-Ebenen nach Schwingungverschleiß	Klaffke 86 52 1256
-----------------	---	-----------------------

Fig. 20 Wear volumes at ceramic cylinders and ceramic planes after fretting tests

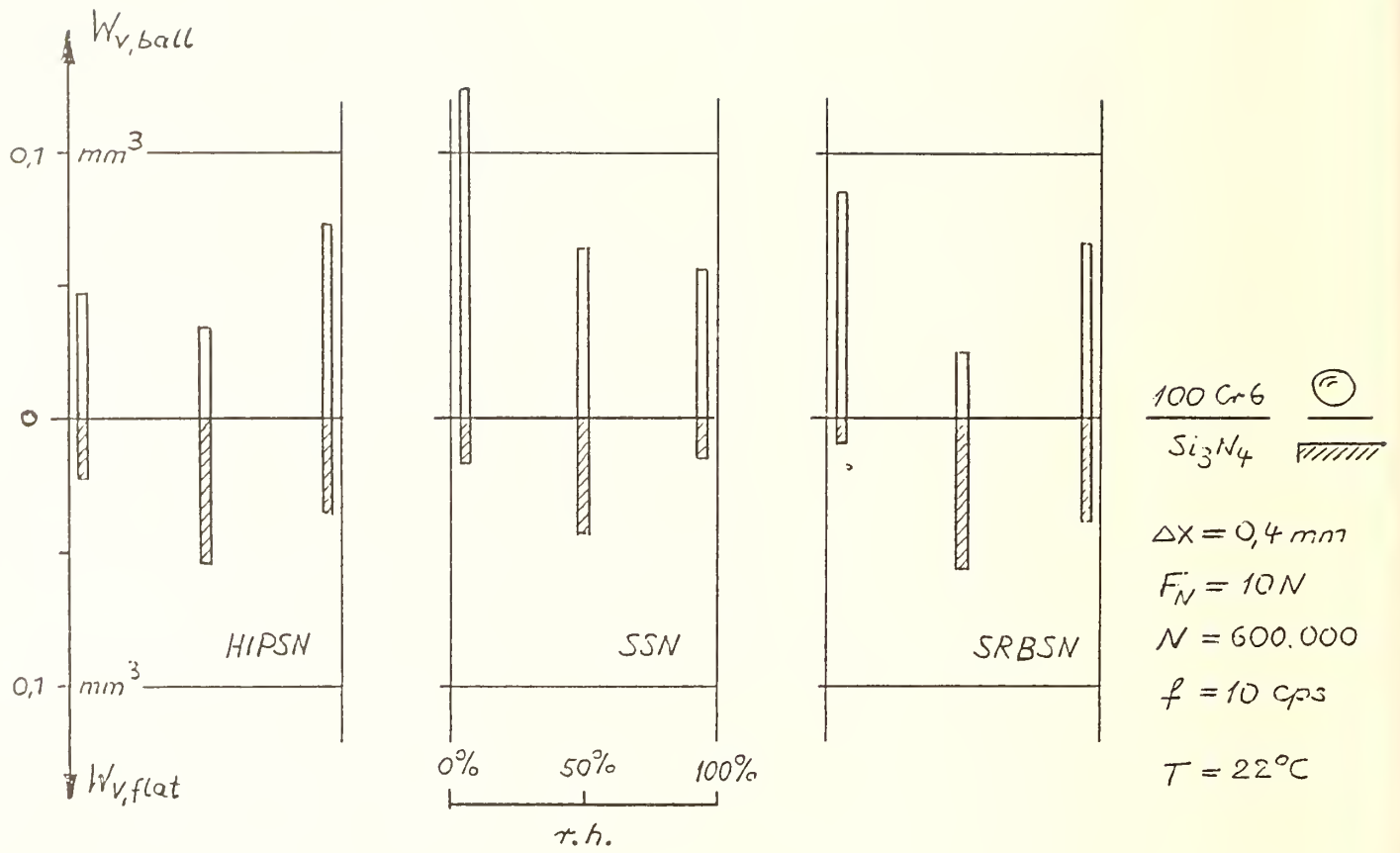


Fig. 21 Influence of humidity on wear volumes at steel balls and ceramic planes for three Si<sub>3</sub>N<sub>4</sub> modifications

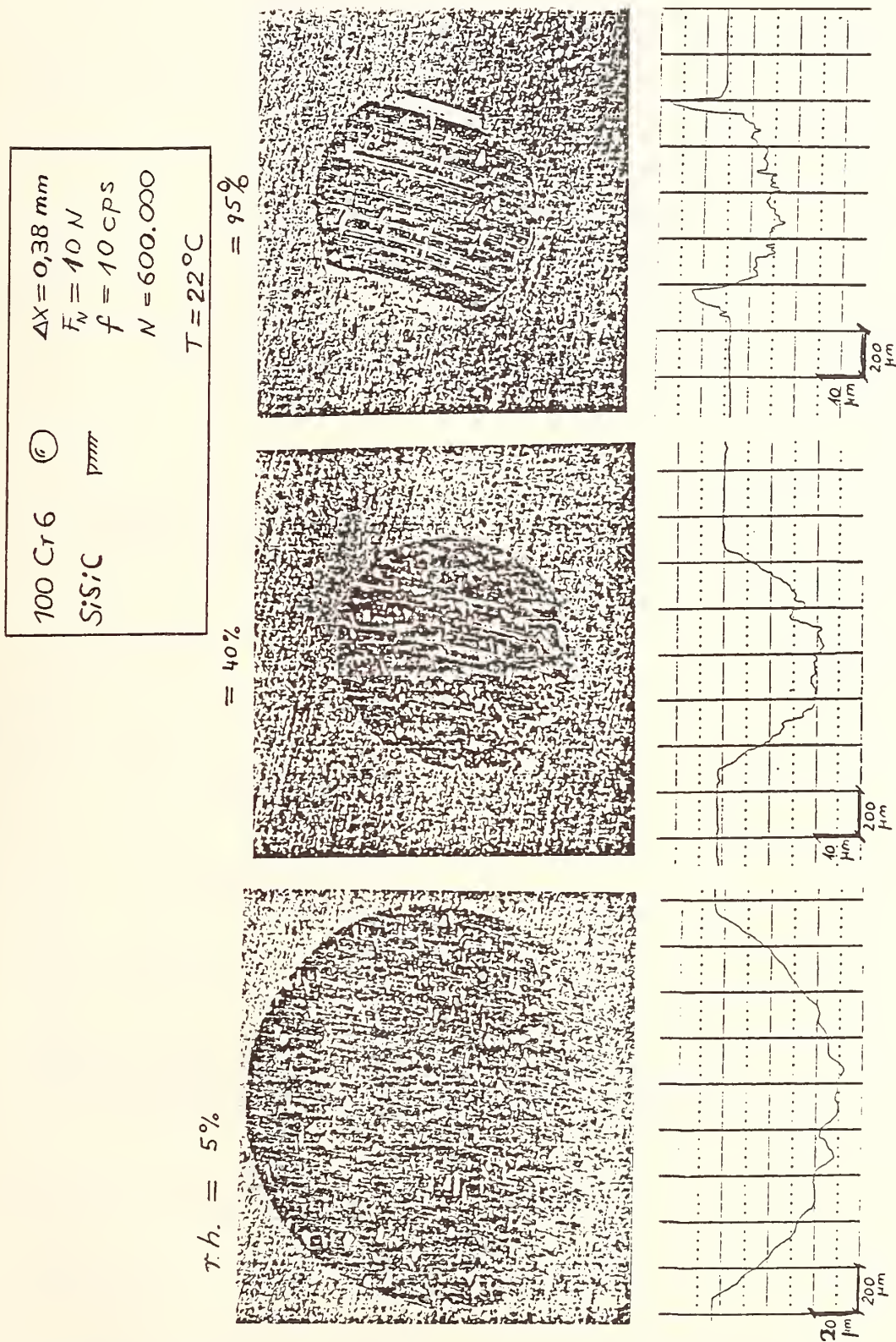


Fig. 22 Wear scars and profilograms of wear scars after fretting test; steel ball / SiC-flat; at different humidities

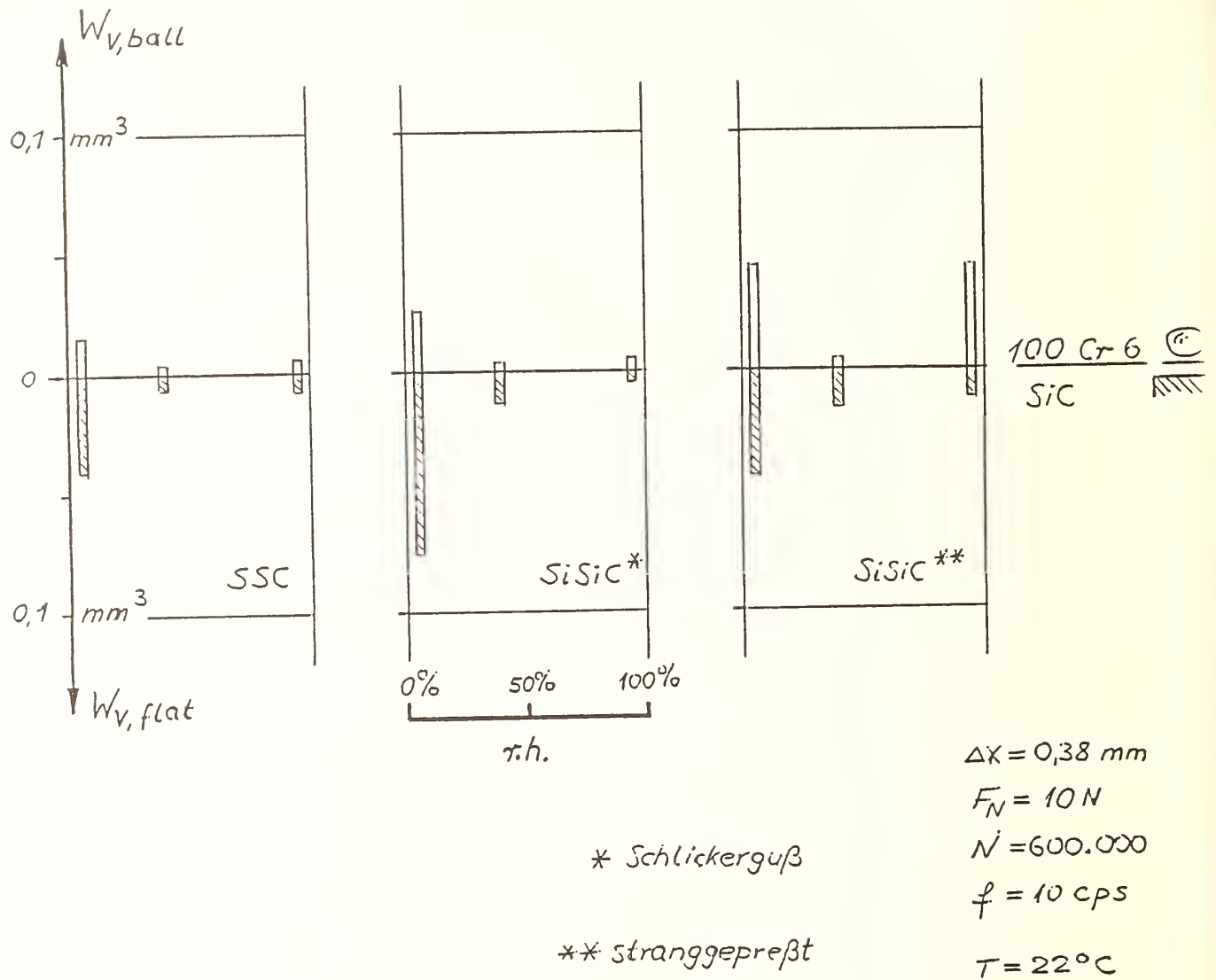


Fig. 23 Wear volumes of steel and ceramic specimens after fretting test at different humidities; three modifications of SiC

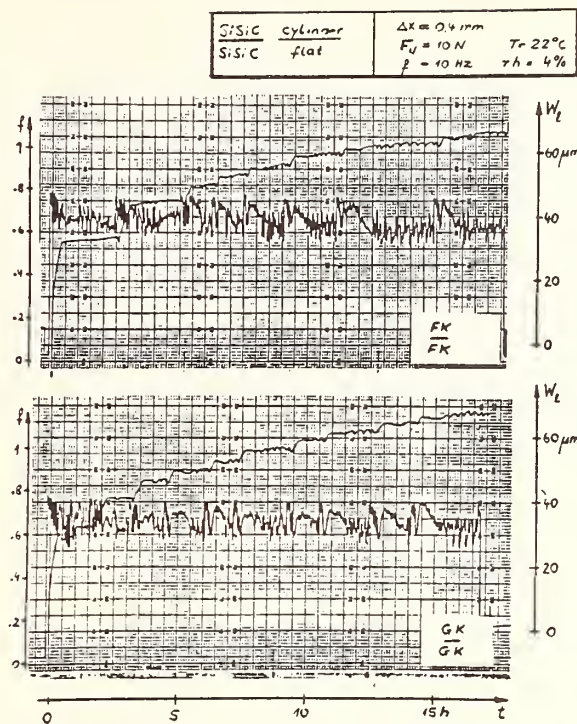


Fig. 24 Coefficient of friction and linear wear for two modifications of SiSiC in dry air

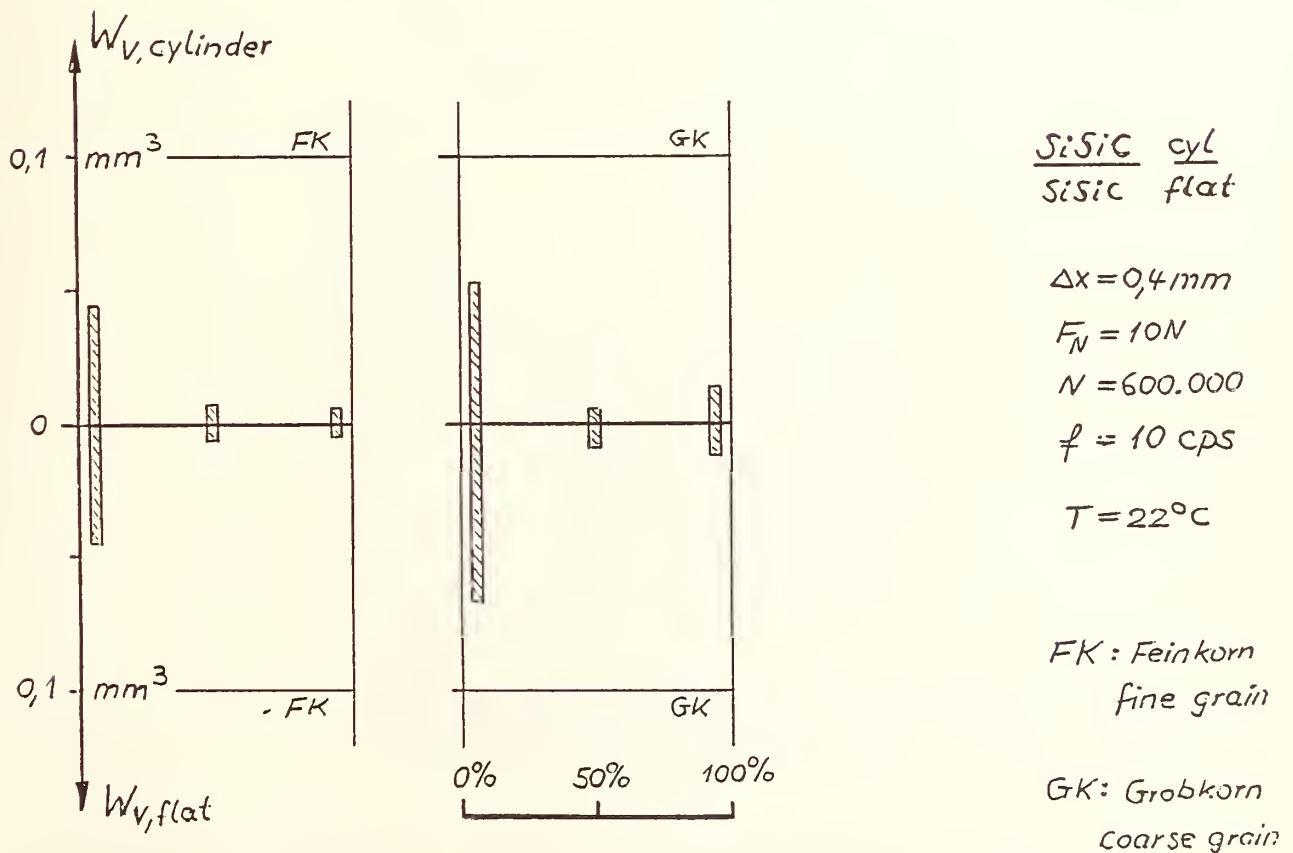


Fig. 25 Wear volumes of ceramic specimens after fretting test at different humidities; fine grained and coarse grains silicized SiC

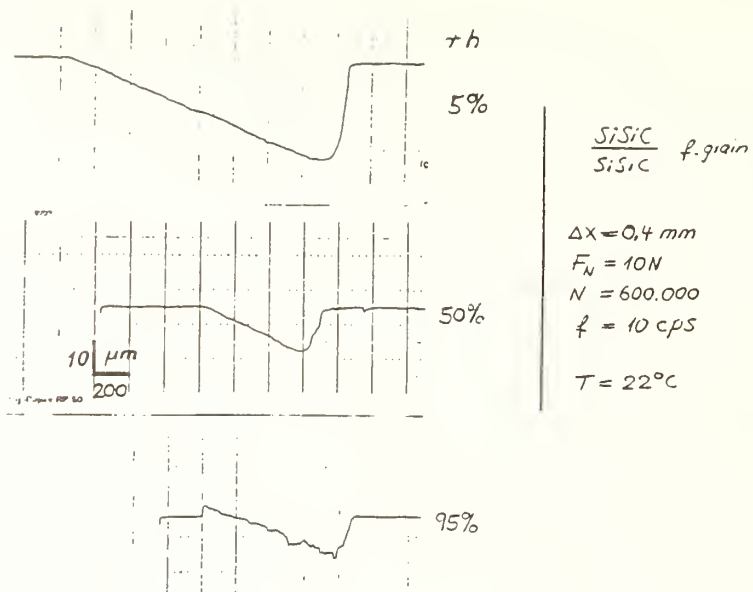


Fig. 26 Wear scar profilograms on fine grained SiSiC specimen after fretting test in air with different humidities

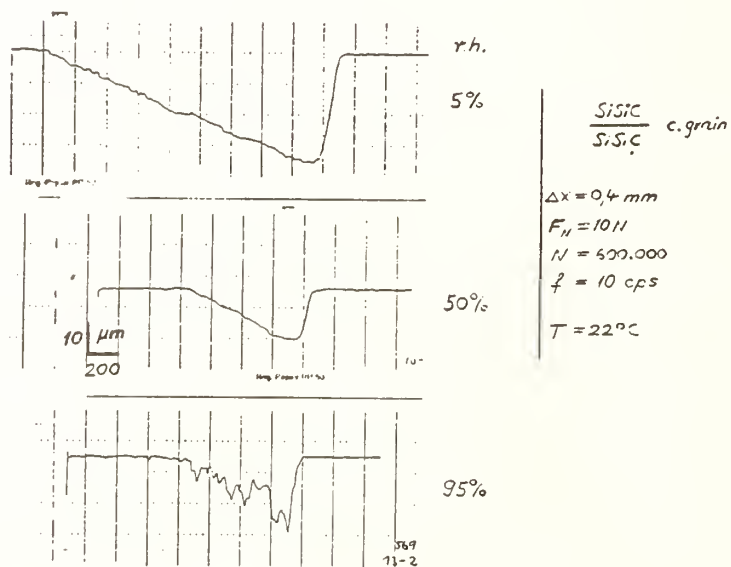
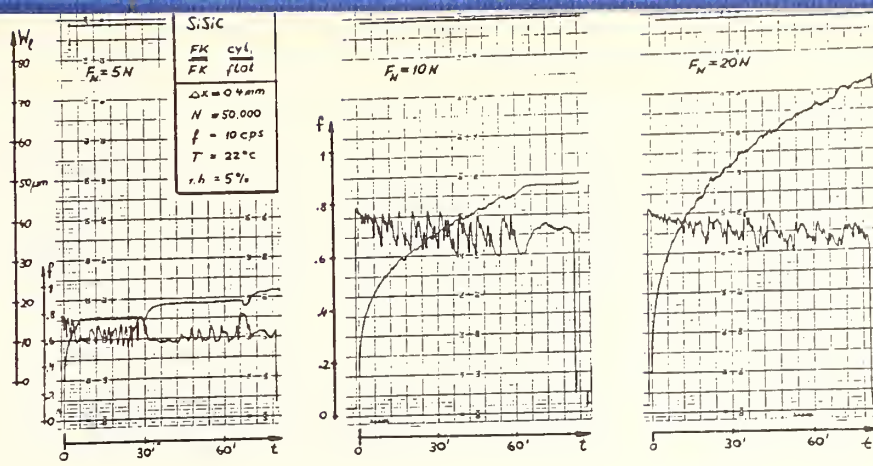
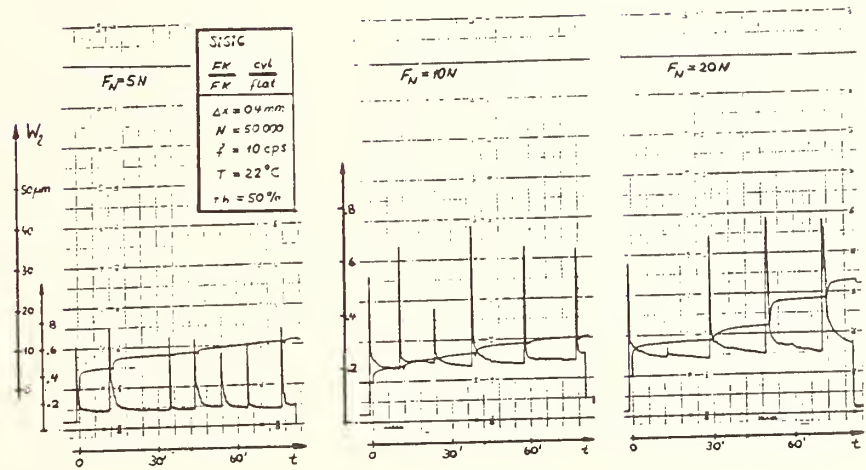


Fig. 27 Same as above for coarse grained SiSiC

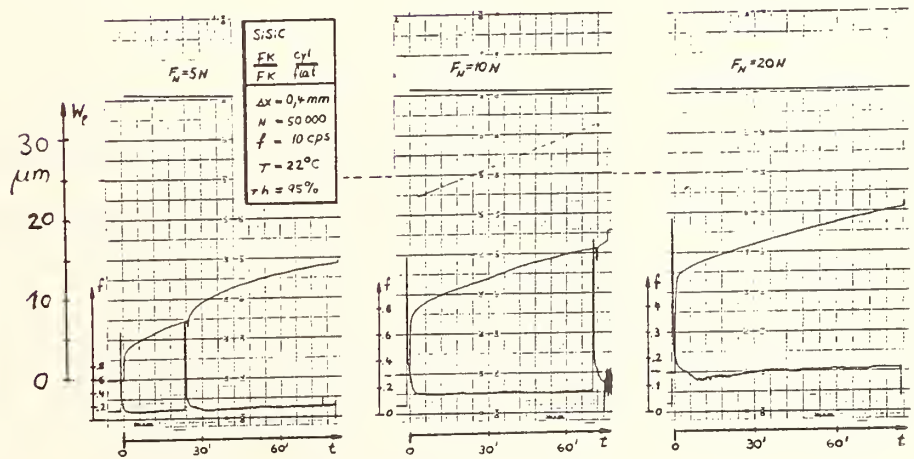
$r.h = 5\%$



$r.h = 50\%$



$r.h = 95\%$



Figs. 28-30 Influence of normal force on fretting wear behavior of fine grains SiSiC against itself at different humidities

## Tribology of Advanced Ceramics

S. M. Hsu  
National Institute of Standards and Technology  
Gaithersburg, MD 20899

### ABSTRACT

Research in materials science of advanced ceramics has been developing rapidly. As materials change and new materials are constantly being developed, the evaluation of these materials for tribological applications becomes a critical issue. This paper examines several important considerations in friction and wear testing of ceramic materials. Detailed test sample characterization is required to define the materials pair. Sample preparation, selection of load and speed, environmental control, and contamination effects are crucial to the understanding of wear mechanisms.

The tribological property of Alumina and water was studied. Water has been found to reduce friction and wear of the alumina system. A tribochemical film was found on the surfaces of water lubricated alumina wear surfaces under boundary lubrication conditions. Results suggest that alumina, under contact stress and high flash temperatures, undergoes phase transformation from alpha to gamma alumina. Gamma alumina subsequently reacts with water to form hydroxides of alumina. Depending on temperatures, boehmite [ $\text{AlO}(\text{OH})$ ] and bayerite [ $\text{Al}(\text{OH})_3$ ] will be formed. Wear debris analysis suggests the presence of bayerite. Independent wear test results found that boehmite reduces friction. Phase diagram and decomposition sequence data suggest that boehmite could transform to

### Considerations in ceramic wear testing

The unique properties of ceramics require that care must be taken when conducting wear tests. The two critical conditions for wear testing are speed and load. Under normal four-ball wear test conditions (52100 steel specimens and hydrocarbon lubricants), the typical speed and load ranges are 0.1 to 1 m/s sliding speed and 40-240 Newtons of machine loading. For ceramics, due to large differences in the hardness of various ceramics, to achieve the same contact stresses, loads have to be adjusted significantly for valid comparison.

The contact pressure is dependent upon the geometry of the contact and the material properties. The geometry of the four-ball contacts provide a distribution of force based on the applied load of  $N = 0.408L$ , where  $L$  is the applied machine load, and  $N$  is the normal load on the surface of single ball. Material parameters, however control the load distribution on the surface. The initial contact area is described by the Hertz equation given in Equation [1].

$$a = \frac{3\pi N(k_1+k_2)R_1R_2}{4(R_1+R_2)}^{1/3}$$

where  $R_1 = R_2 =$  radius of ball (6.35 mm = 0.25 inch)

$N =$  normal load on the surface of a ball

$a =$  radius of Hertz constant

Subscripts refer to materials 1 and 2. For the case where they are the same:

$$k_1 = k_2 = \frac{1 - \nu^2}{\pi E}$$

where  $\nu$  = Poisson's ratio

E = Young's modulus

The basic result of these material parameters on the Hertzian contact diameter is that harder materials deform less under stress and produce higher contact pressures. A graph of calculated maximum contact pressures (assuming hemispherical pressure distribution) for alumina and 52100 steel is given in Figure 2 using values of E and  $\nu$  of 206 GPa and 0.30 for 52100 steel and 403 GPa and 0.236 for polycrystalline alumina, respectively. The curves show that assuming elastic contact, the maximum contact pressures for alumina are 50% higher than steel given the same applied load. The pressure provided by steel at twenty kilogram load is experienced by alumina at a bit less than six kilograms. These calculations serve as a conservative estimate of the contact stresses. One would expect, therefore, that initial machine loads selected for 4-ball wear tests on ceramics should be lower than loads usually utilized for 52100 steel if one wishes to test at the same contact pressure.

The other issue critical in ceramic wear testing is the temperature in the contact junction. Materials with lower thermal conductivity do not allow heat to dissipate as rapidly and give higher local contact temperatures. The difference in thermal conductivity and thermal diffusivity between ceramics and metals therefore causes higher local contact temperatures for ceramics under the same test conditions. A recent study by Munro<sup>2</sup>, who modeled the adiabatic temperature distribution within test specimens of the four-ball wear test predicted high temperatures different for alumina specimens versus steel specimens (Figure 3). Under

conditions of 500 rpm, 40 kg load, and coefficient of friction of 0.075 (lubricated), temperatures of  $\sim 160^{\circ}\text{C}$  were predicted for the contact junction using steel specimens. Temperatures of  $\sim 400^{\circ}\text{C}$  were predicted for alumina, a difference of  $240^{\circ}\text{C}$ . In addition, the thermal gradients in the alumina were much sharper.

These two examples of contact pressure and temperature differences between alumina and steel specimens illustrate the need to analyze the actual contact conditions without assumptions. Therefore, data interpretation should take these factors into account.

### Cleaning Procedures

Interest in the use of ceramics has led to an increasing number of tribological studies being conducted on ceramics. In these studies, there is a vast array of different methods used to prepare specimens for testing ranging from rinsing with ethanol<sup>3</sup> or acetone<sup>4</sup> to baking<sup>4</sup> and ion cleaning<sup>6</sup>. Indeed, in many cases, the cleaning procedure affects the tribological test results.

Unlubricated four-ball tests at low to moderate load exhibited unusual friction traces (Figure 4). These specimens had been cleaned ultrasonically in hexane, then acetone, and rinsed with a stream of nitrogen gas. The friction traces in Figure 4 indicate that a contaminant (residual hydrocarbon or possible water) is present on the surface during these tests which affect the results. At low load (10 kg) the contaminant protects the alumina surface and low friction and wear are observed. At moderate loads (15 kg) low friction and wear are observed. At moderate loads (15 kg) low friction is observed for the initial stage of the test with a transition to high friction during the test (after approximately 2

minutes). The high load (20 kg) test also starts at lower friction but after only a few seconds jumps to the high friction level. The nature of these results suggest as one explanation a surface contaminant is present that reduces friction and wear in these tests.

ESCA was used to analyze the surface to characterize the contaminants. Figure 5 shows an ESCA spectrum on alumina surface. The lower trace represents the ascleaned surface while the upper trace represents the surface after approximately a 30Å layer of material was removed by argon ion sputtering. Quantification was accomplished by comparing the ratio of the carbon peak height to the oxygen peak height. The results of ESCA analyses on several cleaning procedures is given in Table 1. Organic solvents seem to leave a high degree of carbon containing contaminant (a,b) unless followed by a detergent and deionized water rinse (c), or by baking at high temperature (d,e). The difference between the as-prepared results and the sputtered results gives an indication of the tenacity of the contaminant. A strongly bound contaminant shows very little difference in C/O ratio due to sputtering (a) while a weakly adsorbed contaminant shows a large difference (d, e). The organic solvents apparently leave organic residues on the surface (a, b). The Micro/DI water cleaning in addition to the organic solvents (c) effectively removes most of these residues by dissolving them into solution. The bakeout removes the organic contaminants by oxidizing them to CO and CO<sub>2</sub> which are then weakly adsorbed on the surface (d, e). Additional friction experiments confirmed the role of surface contaminant levels on friction using these cleaning procedures (Figure 6). Specimens cleaned with hexane/acetone exhibit a low coefficient of friction which is relatively constant throughout the test.

The more rigorous procedure (including an overnight bakeout at 580°C) produced an immediate high coefficient of friction.

These results show that surface cleaning procedures can have a pronounced effect on the tribological performance of ceramic materials. Based on these results on alumina, a general cleaning procedure is recommended: 1) Ultrasonic cleaning with hexane/toluene (9:1) to remove residual polishing oils; 2) Ultrasonic cleaning with acetone to remove polar surface contaminants and residual hexane and toluene; 3) Ultrasonic cleaning with a laboratory detergent (micro at 2% concentration in deionized water) to remove residual organics; 4) Several ultrasonic rinses with deionized water to remove residual detergent; and 5) High temperature bakeout when feasible.

#### Alumina Wear under Different Fluids

Alumina was tested under dry and liquid lubricated conditions using a four-ball wear tester at 600 rpm (0.23 m/s) and loads ranging from 5 to 60 kg. These loads result in estimated mean Hertzian contact pressures of 1.6 to 3.7 GPa for alumina specimens. The data is plotted in Figure 7 as log of the wear scar diameter versus log of the load. Unlubricated tests were conducted under dry air (<10 ppm water) atmosphere, and produced very rough friction traces with very high levels of friction and wear. Wear tests conducted under identical conditions, with paraffin oil and water as lubricants, produced lower friction and wear. The friction traces for the water lubricated alumina tests were smooth and resulted in steady state coefficient of friction levels of 0.31, representing a friction reduction of 50% below that of the unlubricated case. Wear was reduced by a factor of three as measured by the wear scar diameter.

Examination of the water lubricated worn surfaces using scanning electron microscopy (SEM) (Figure 8) indicated the presence of a "film" in the contact region. The film had the appearance of a coherent compact of material with the ability to flow plastically and be smeared out in various regions of the contact. Further analysis of the film using FTIR indicated the presence of O-H bonds. These observations suggested that tribochemical reactions might be taking place between the water and the alumina. Tomizawa and Fischer previously had found tribochemical reaction between water and "inert" silicon nitride<sup>4</sup>.

To elucidate the nature of the tribochemical reaction products, tests were performed to react water with two alumina samples: alpha and gamma alumina. Low temperature tests were conducted at room pressure and 100°C for 24 hours. Higher temperature tests were conducted in a bomb reactor at approximately 1.54 MPa (223 psia) and 200°C for 60 minutes. At the end of the test, the powders were analyzed for reaction products using thermogravimetric analysis (TGA) and x-ray powder diffraction (XRPD).

Alpha alumina showed no reaction at either temperature. Gamma alumina, however, reacted at both temperatures. The TGA temperature scans of gamma alumina and the two reaction products of gamma alumina and water are presented in Figure 9. The low temperature reaction product thermally decomposed at 272°C and was identified using XRPD as bayerite [Al(OH)<sub>3</sub>]. The higher temperature reaction produced a material that decomposed at higher temperatures (510°C) and was identified using XRPD as boehmite [AlO(OH)].

It has been shown that chemical reactions occur between gamma alumina and water (and at reasonable rates), however, no reaction was observed between alpha alumina and water. A transformation of alpha alumina to

delta alumina was observed by Hines, Bradt, and Biggers<sup>7</sup>. They found that when alpha alumina is subjected to abrasion in unlubricated wear tests, particles of delta alumina were formed. Delta alumina is one of the transition alumina's and in many cases is very difficult to distinguish from gamma alumina.

Analysis of the wear debris was conducted to provide direct evidence of the nature of the tribochemical reaction products. Wear tests were conducted using a specially prepared gold coated test cup to ensure that no water-iron interactions would interfere with the analyses. Small amounts of debris were painstakingly collected and analyzed using XRPD and TGA. The x-ray powder diffraction (XRPD) spectrum indicated that most of the wear debris was composed of alpha alumina, however, a small amount of material was observed that appeared to be bayerite. Thermogravimetric analysis (TGA) showed a large weight loss at 249°C and a smaller weight loss at 325°C. These decomposition temperatures are consistent with those of the trihydroxides and, taken with the other analyses, indicate that bayerite is present in the wear debris.

Given all of the data, the following picture emerges for the tribochemical mechanism of water lubricated alumina. High temperatures and shear stresses in the contact junction produce a phase transformation from alpha to transition alumina. Transition alumina reacts with water at high pressure and temperature to form an aluminum hydroxide. Wear debris analysis, however, indicated that bayerite is present at the end of the test. It appears, therefore, that boehmite transforms to bayerite as it emerges from the high pressure, high temperature environment of the wearing contact to the low pressure low temperature environment outside of the wear

scar. The result is a layer lattice material that lubricates the contact junction.

### Conclusions

Sample cleaning procedures have been demonstrated to alter the results of unlubricated friction tests conducted with dense polycrystalline alumina. A simple cleaning procedure is offered that uses organic solvents to remove residual polishing oils and greases followed by a detergent solution to remove residual organics. A series of rinses with high purity deionized water then removes residual detergent and results in relatively clean surfaces. The samples should be baked out at a moderately high temperature to remove moisture or oxidize any remaining contaminant.

It has also been demonstrated how material properties of elastic modulus and thermal conductivity affect the test severity with regard to surface stress and temperature, respectively.

Wear tests conducted with water on alumina showed significant friction and wear reduction. Detailed analysis of the wear debris and coupled with static reaction experiments have resulted in the following sequence of events:

1. Contact conditions induce a phase transformation from alpha to transition alumina.
2. Chemical reaction occurs between water and transition alumina under high temperatures and pressures to produce aluminum hydroxides.
3. These aluminum hydroxides are layer lattice structures and serve to lubricate the contact junction.

## References

1. Kingery, W. D., Bowen, H. K., and Uhlmann, D. R., Introduction to Ceramics, 2nd Edition, John Wiley & Sons, New York, 1976.
2. Munro, R. G., "Temperature Considerations in the Study of Surfaces Using a Four-Ball Apparatus," J. Appl. Phys., 57, 11, p. 4950-4953., June 1, 1985.
3. Steijn, R. P., "Sliding and Wear in Ionic Crystals," J. Appl. Phys., 34, (2), pp. 419-429 (1963).
4. Aronov, V., and Mesyef, T., Trans. ASME, 108, pp. 16-21 (1986).
5. Scott, H. G., "Friction and Wear of Zirconia at Very Low Sliding Speeds," Wear of Materials, pp. 8-12 (1985).
6. Miyoshi, K., Buckley, D. H., and Srinivasan, M., "Tribological Properties of Sintered Polycrystalline and Single-Crystal Silicon Carbide," American Ceramic Society Bulletin, 62, (4), pp. 494-500 (1983).
7. Hines, J. E., Jr., Bradt, R. C., and Biggers, J. V., "Delta Alumina Formation during the Abrasive Wear of Polycrystalline Alumina," Wear of Materials 1979, pp. 540-550.

Table 1. Residual Contaminant (Carbon Containing) on Alumina after Various Cleaning Procedures as Measured by ESCA

Number	Cleaning Procedure	Contaminant Level as Measured by c/o Peak Ratios	
		As-Prepared	Sputtered
a	Hexane-Toulene/ Acetone/DI	0.94	0.92
b	Hexane/Pyridine	0.58	0.20
c	Hexane-Toulene/ Acetone/Micro/DI	0.19	0.14
d	Micro/DI/Bake at	0.17	0.05
e	Hexane-Toulene/ Acetone/DI + Bake at 693°C for 1 1/2 Hours	0.11	0.06

Each solvent was used by immersing the specimens in them and agitating ultrasonically for approximately 1 minute.  
 DI - 18 mΩ resistance deionized water.  
 Micro = the laboratory detergent utilized (2% in DI water).

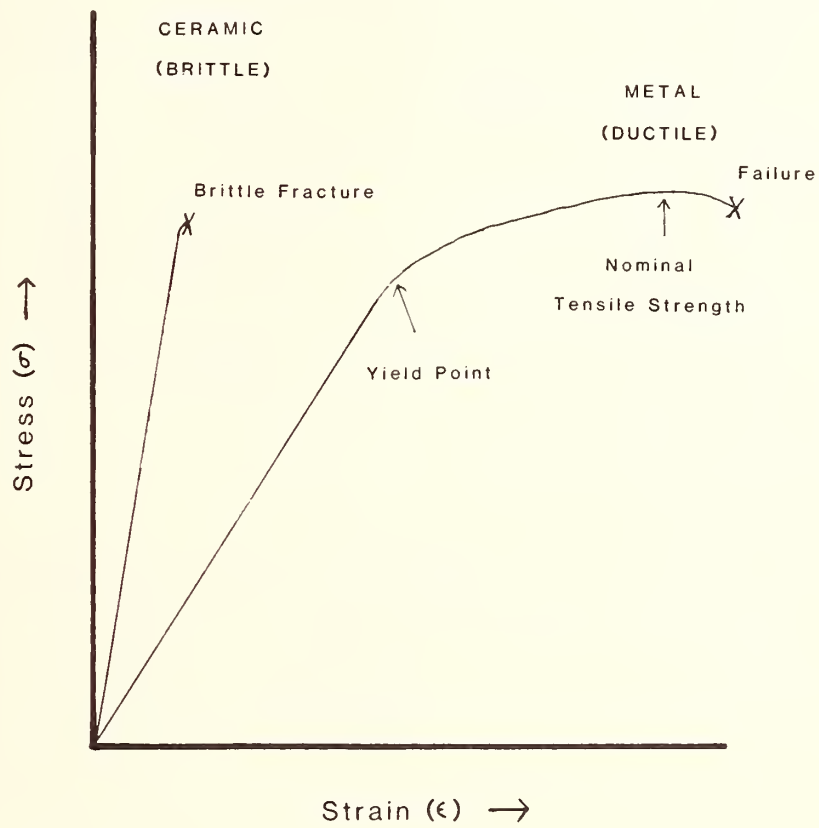


Fig. 1 Typical stress-strain behavior for metals and ceramics at room temperature

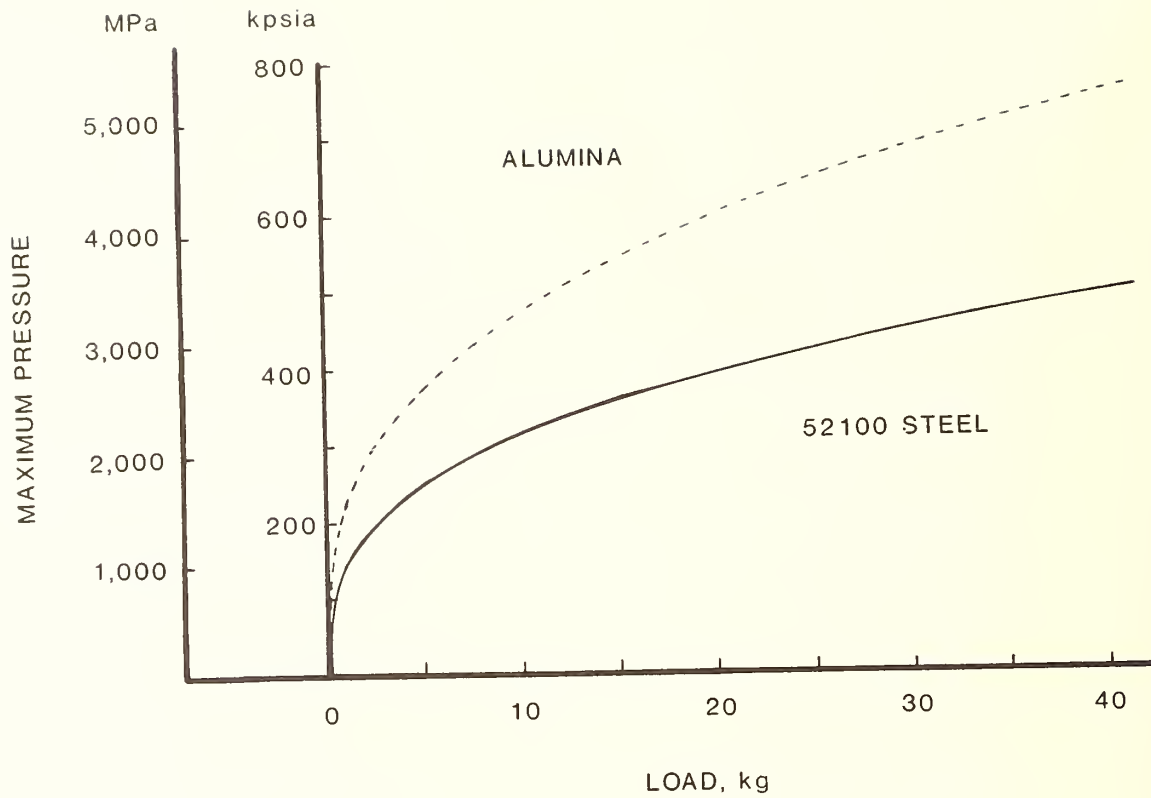
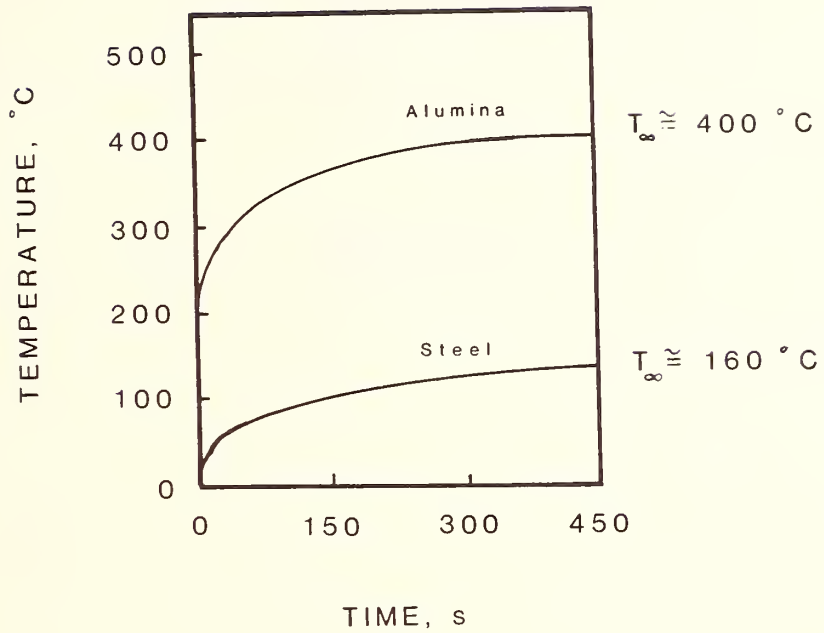
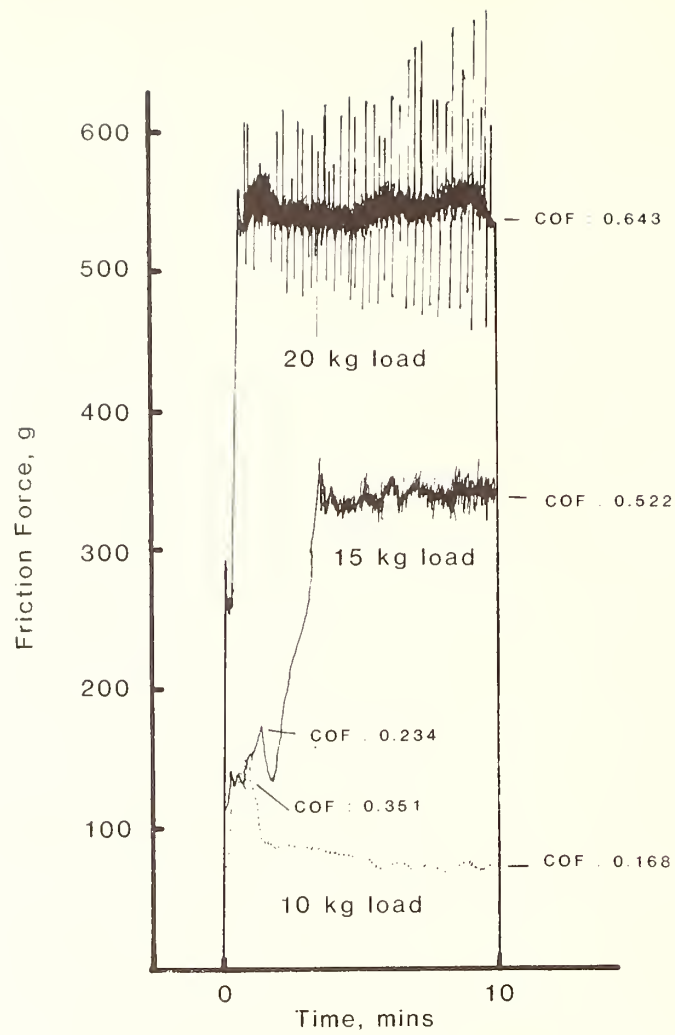


Fig. 2 Comparison of calculated contact pressures for 52100 steel vs. dense polycrystalline alumina



Source : Munro (6)

Fig. 3 Calculated contact junction temperature as a function of time for lubricated alumina and steel four-ball tests



Conditions . 600 rpm, 0.25 l/min dry air, 10 min duration, alumina specimens

Fig. 4 Friction traces for unlubricated alumina four-ball tests at various loads

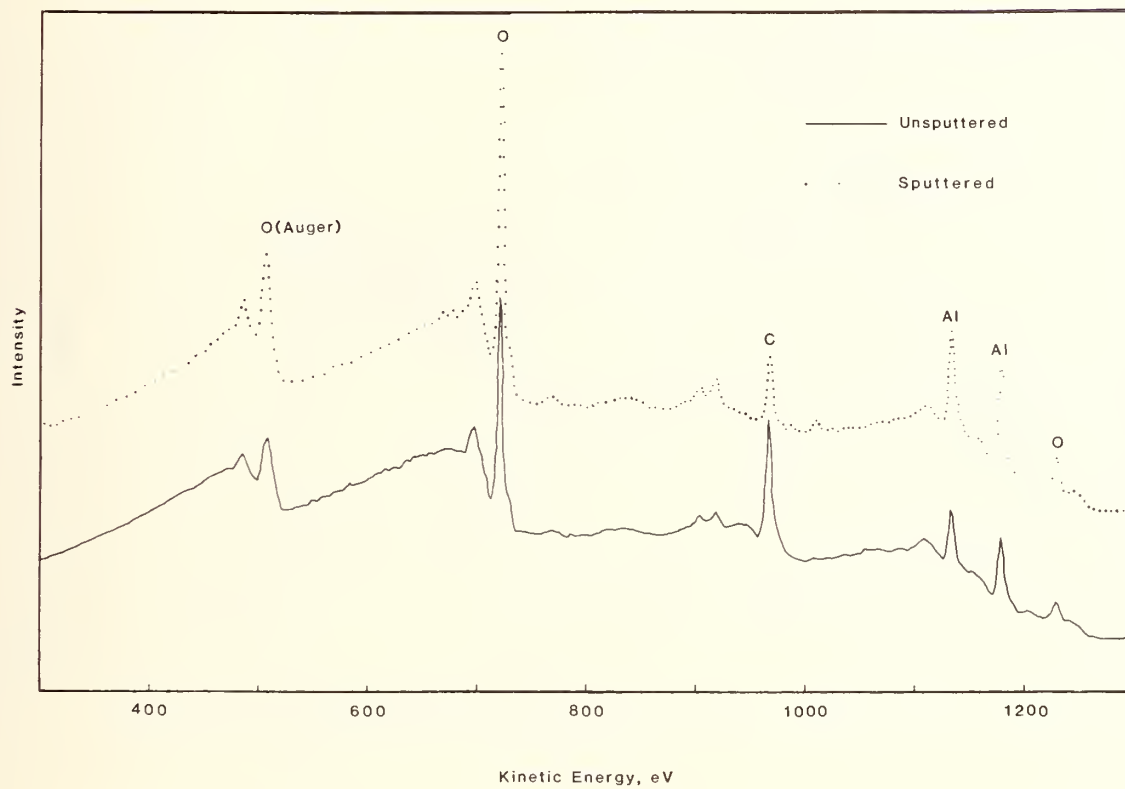


Fig. 5 Typical ESCA analysis of an alumina surface

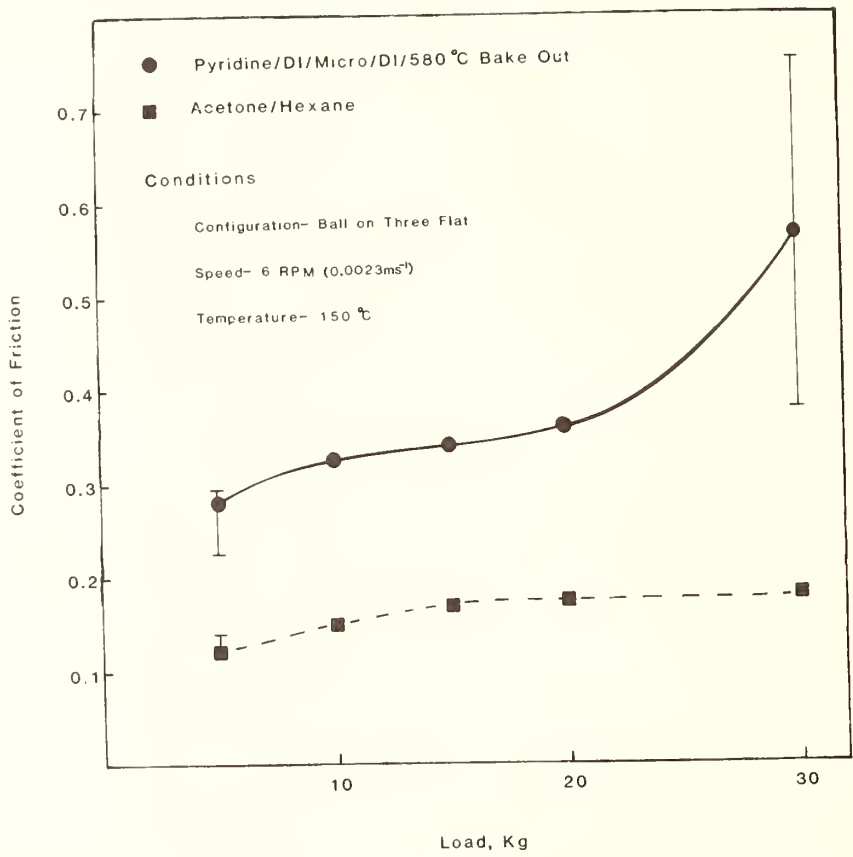


Fig. 6 Effect of cleaning procedure on the coefficient of friction for "unlubricated" alumina on alumina tests

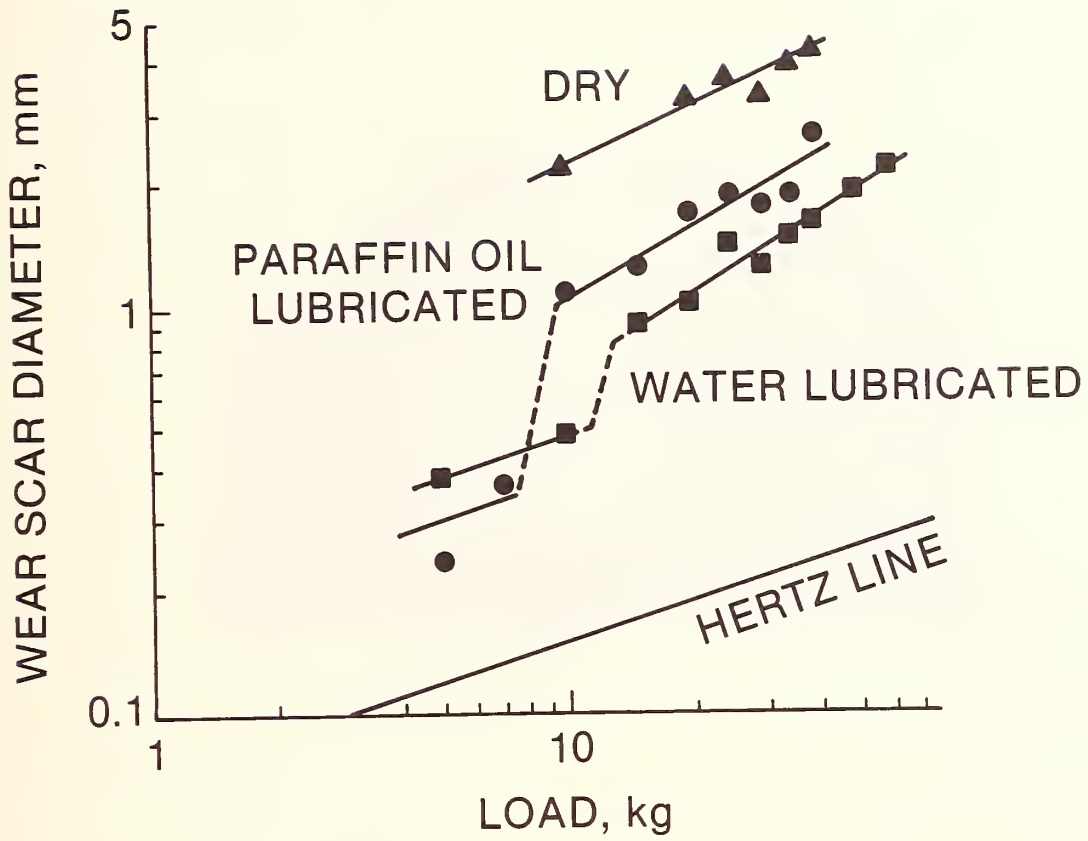


Fig. 7 Comparison of wear as a function of load for unlubricated, paraffin oil lubricated, and water lubricated alumina constant' condition tests

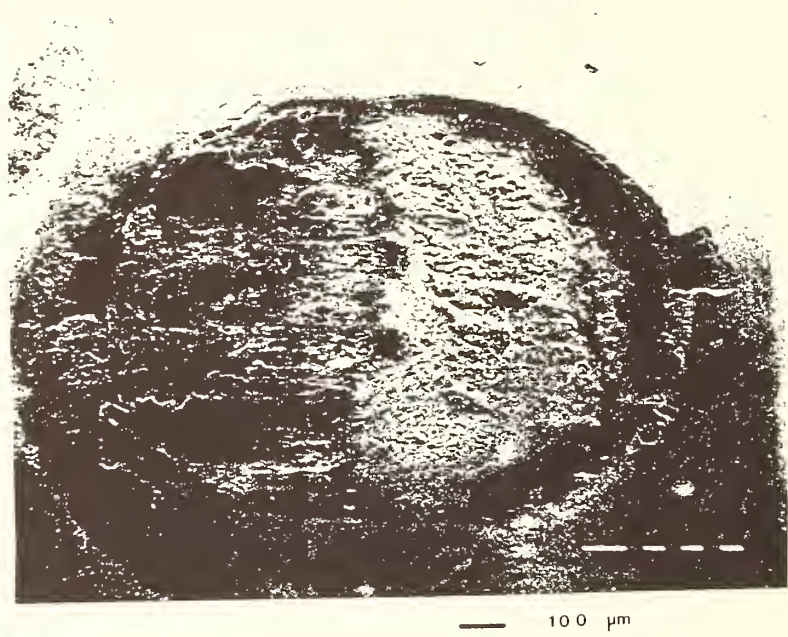


Fig. 8 SEM photomicrograph of lower specimen wear scar water-lubricated four-ball test

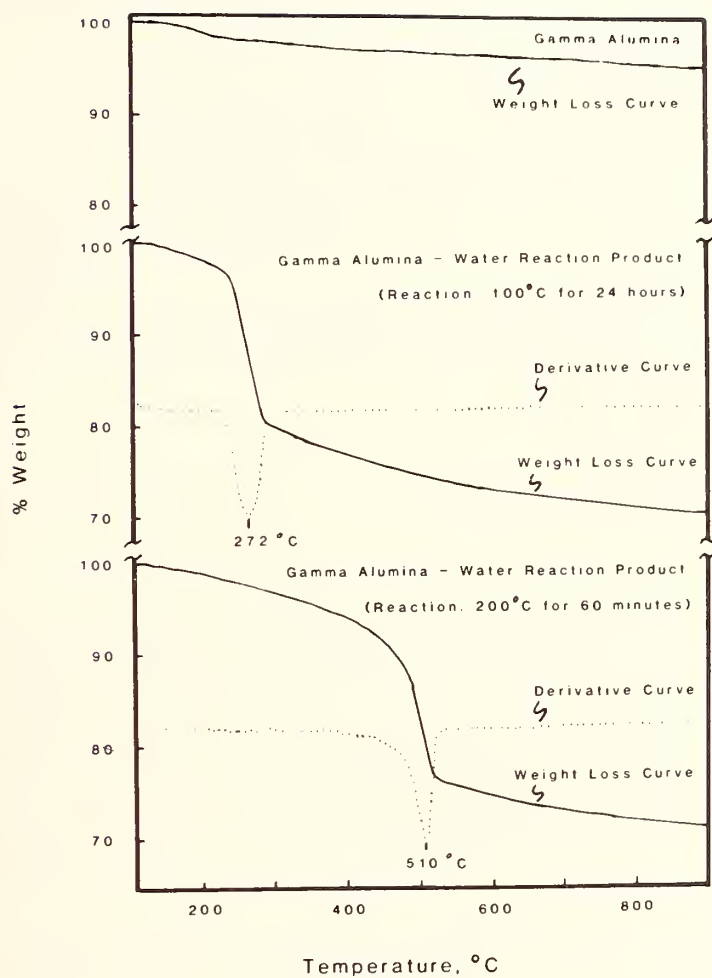


Fig. 9 TGA analysis of gamma alumina and gamma alumina/water reaction products



U.S. DEPT. OF COMM. <b>BIBLIOGRAPHIC DATA SHEET</b> <i>(See instructions)</i>	<b>1. PUBLICATION OR REPORT NO.</b> NIST/SP-766	<b>2. Performing Organ. Report No.</b>	<b>3. Publication Date</b> May 1989
<b>4. TITLE AND SUBTITLE</b>  NBS/BAM 1986 Symposium on Advanced Ceramics			
<b>5. AUTHOR(S)</b> S. M. Hsu and H. Czichos, Editors			
<b>6. PERFORMING ORGANIZATION</b> <i>(If joint or other than NBS, see instructions)</i>  <b>NATIONAL INSTITUTE OF STANDARDS AND TECHNOLOGY</b> <i>(formerly NATIONAL BUREAU OF STANDARDS)</i> <b>U.S. DEPARTMENT OF COMMERCE</b> <b>GAITHERSBURG, MD 20899</b>			<b>7. Contract/Grant No.</b>  <b>8. Type of Report &amp; Period Covered</b> Final
<b>9. SPONSORING ORGANIZATION NAME AND COMPLETE ADDRESS</b> <i>(Street, City, State, ZIP)</i> same as item 6			
<b>10. SUPPLEMENTARY NOTES</b>  Library of Congress Catalog Card Number: 89-600737  <input type="checkbox"/> Document describes a computer program; SF-185, FIPS Software Summary, is attached.			
<b>11. ABSTRACT</b> <i>(A 200-word or less factual summary of most significant information. If document includes a significant bibliography or literature survey, mention it here)</i> <p>Advanced ceramics offer many advantages that other materials do not possess. They have high strength, dimensional stability, are chemically inert, lightweight, wear resistant, and have desirable properties in electrical, optical, and thermal applications. At high temperatures, they are the only class of material with reasonable properties. As such, advanced ceramics is increasingly used in electronic, structural, wear, optical, and electrical applications and devices.</p> <p>Worldwide production of advanced ceramics is growing rapidly. Since ceramics are based on alumina and silica, the most abundant minerals on earth, effective utilization of ceramics carries implications into the next several centuries.</p> <p>One of the major technical barriers to widespread use of ceramics is the inability of industry to manufacture reliable ceramics reproducibly and economically. Advanced ceramics are sensitive to small defects introduced during processing and generated during use. The identification of key parameters and subsequent measurements of these parameters are crucial to control the quality of ceramics. The National Institute of Standards and Technology (NIST) (formerly National Bureau of Standards, NBS), and the Bundesanstalt fur Materialprufung (BAM) to a large extent, share a similar mission to assist their respective industries to achieve reliable manufacturing through standards. This symposium therefore provides timely exchange of technical information on a very significant subject area.</p>			
<b>12. KEY WORDS</b> <i>(Six to twelve entries; alphabetical order; capitalize only proper names; and separate key words by semicolons)</i>  BAM; ceramics; fretting, NIST; powder; sintering; technical exchange; wear			
<b>13. AVAILABILITY</b> <input checked="" type="checkbox"/> Unlimited <input type="checkbox"/> For Official Distribution. Do Not Release to NTIS <input checked="" type="checkbox"/> Order From Superintendent of Documents, U.S. Government Printing Office, Washington, D.C. 20402. <input type="checkbox"/> Order From National Technical Information Service (NTIS), Springfield, VA. 22161			<b>14. NO. OF PRINTED PAGES</b> 159  <b>15. Price</b>













